DISSERTATION

MODELING ANCILLARY EFFECTS: IMPROVEMENTS IN MEMBRANE CHROMATOGRAPHY AND ARRHENIUS-TYPE KINETICS

Submitted by

Shane E. Bower

Chemical and Biological Engineering

In partial fulfillment of the requirements

For the Degree of Doctor of Philosophy

Colorado State University

Fort Collins, Colorado

Spring 2006

COLORADO STATE UNIVERSITY

March 28, 2006

WE HEREBY RECOMMEND THAT THE DISSERTATION PREPARED UNDER OUR SUPERVISION BY SHANE E. BOWER ENTITLED MODELING ANCILLARY EFFECTS: IMPROVEMENTS IN MEMBRANE CHROMATOGRAPHY AND ARRHENIUS-TYPE KINETICS BE ACCEPTED AS FULFILLING IN PART REQUIREMENTS FOR THE DEGREE OF DOCTOR OF PHILOSOPHY.

Committee on Graduate Work

Advisor

Department Head

ABSTRACT OF DISSERTATION

MODELING ANCILLARY EFFECTS: IMPROVEMENTS IN MEMBRANE CHROMATOGRAPHY AND ARRHENIUS-TYPE KINETICS

The time lag created by column peripherals and the column flow distribution headers was modeled for a membrane chromatography system using a Sartorious Q-membrane and bovine serum albumin (BSA). A numerical method was applied that removed the zero order and first order time delays from the breakthrough curve without requiring knowledge of the shape or characteristics of the breakthrough curve in the absence of the time delay. The method was applied to the calculation of Langmuir isotherm parameters under dynamic flow conditions. The Langmuir isotherm calculated under dynamic flow conditions with the time delay removed closely matched the Langmuir isotherm under static (no flow) conditions.

The pore size distribution for a 500 kDa molecular weight cut-off cellulose acetate ultrafiltration membrane was determined from the analysis of field emission scanning electron microscopy (SEM) images. A log-normal distribution was fit to the discrete pore size distribution data by both pore radius and normalized flow. The discrete distribution and both continuous distributions were used to calculate membrane flux and Dextran rejection profiles and compared to experimental results. Improvements in flux predictions were made when modeling the pore size distribution based on normalized flow through the discrete pore size distribution. The flux calculations were in strong

agreement with the experimental results and the rejection calculations were in good agreement with the experimental results.

Agricultural and herbaceous feedstocks may contain appreciable levels of sucrose. The survivability of sucrose and its hydrolysis products, fructose and glucose, was evaluated during dilute sulfuric acid processing over conditions typically used to pretreat lignocellulose biomass. Temperatures from 160-200 °C, acid concentrations from 0.1 to 2.0 %(w/w) sulfuric acid, and reaction times from 3 to 12 minutes were used for the pretreatment conditions. No residual sucrose was detected for any of the conditions, but appreciable concentrations of fructose and glucose were detected under most pretreatment conditions. Different mathematical approaches were used to fit the kinetic parameters for acid-catalyzed thermal degradation of these sugars. Since both sugars may survive dilute acid pretreatment, they could provide an additional carbon source for production of ethanol and other bio-based products.

Shane E. Bower
Department of Chemical and
Biological Engineering
Colorado State University
Fort Collins, CO 80523
Spring, 2006

ACKNOWLEDGEMENTS

I am grateful for the loving support of my family: my parents Sandra and John, my sister and brother-in-law Christa and Chad, and to Amanda. I am also grateful for the many friends I have made during my time at CSU and the many stimulating conversations, both academic and not, that have made my experiences here rich and rewarding.

I would like to thank my fellow group members for their contributions to this work. Dr. Binbing Han provided the ultrafiltration flow and Dextran rejection experimental data for comparisons with my theoretical work and Rachel Specht provided assistance with collecting the scanning electron micrographs.

I would like to thank my advisor Dr. Ranil Wickramasinghe without whose academic and financial support this work would not have been possible. I would like to thank my committee members, Dr. Belfiore, Dr. Linden, and Dr. McMillan, for our conversations over the years. In particular I would like to thank Dr. McMillan for the opportunity to work at the National Renewable Energy Lab (NREL) in Golden over the summer of 2005.

TABLE OF CONTENTS

LIST OF TABLES

LIST OF FIGURES

Chapter 1

INTRODUCTION

1.1 Motivation for research

Previous unpublished work by Bower and Wickramasinghe included an investigation of scaling-up the purification of the ribosome inactivating protein PAP-H from the transformed hairy roots of *Phytolacca americana*. Over the course of the investigation, the bench-top scale of the purification was reduced from ten processing steps, including three chromatographic steps, to eight processing steps including two chromatographic steps. In that work, the prediction was made that the total number of processing steps could be reduced further through creative combined purification processes.

During this work it became apparent that future progress would depend on accurate characterization and modeling of not only the underlying chemical and physical interactions of the solutes of interest (proteins and other cellular materials), but also of the experimental apparatus. The equipment used for purification and kinetic studies frequently contain a host of inefficiencies that directly impact the observed experimental results. Dead volume in tubing, long heat-up times, or poor response times of instrumentation are just a few of the possible apparatus effects that directly impact experimental results. Mathematical modeling and removal of these effects dramatically

improve the analysis of experimental results. Three cases are considered in this work: 1) time lag associated with membrane chromatography tubing, 2) accurate fitting of continuous pore size distributions in ultrafiltration membranes, and 3) determination of kinetic parameters for fructose and glucose degradation under conditions where the heat-up time to reaction conditions is significant. Literature pertinent to the concepts studied in Chapters 2, 3, and 4 are discussed in the introduction to those specific chapters. General background information on membrane chromatography, microfiltration, ultrafiltration, and bio-agricultural products is included in Chapter 1.

1.2 Membrane chromatography

Chromatography is traditionally carried out using a packed bed. The feed containing the solute to be adsorbed flows through the bed. The solute is transported between the resin particles by convective flow. In order to increase the surface area and the number of available binding sites (capacity of the resin), chromatographic particles are usually porous. Thus, the majority of the binding sites are located on the surface of the internal pores. In order to reach these pores, the solute must diffuse from the bulk feed solution, across a liquid film layer at the particle surface and into the pores. Next, the solute diffuses by 'pore diffusion' through the pores and attaches to a binding site on the pore surface.

Conventional chromatography suffers from a number of limitations. The pressure drop across the bed is generally high and tends to increase during operation due to resin deformation. Pore diffusion is often slow, leading to increases in processing time, band

broadening, dilution of the final product, and, in biotechnological separations, possible degradation of the fragile biological product molecules (Roper and Lightfoot, 1995; Thommes and Kula, 1995; Charcosset, 1998, Zeng and Ruckenstein, 1999; Klein, 2000; Ghosh, 2002). Scale up of packed-bed chromatography columns is difficult. If the column is not packed carefully, non-uniform resin distribution will lead to channeling of the feed flow. A separation device with ideal properties is a high-capacity column that allows for high flow rates at low pressure drops. For maximum speed of separation, the separation should only be limited by kinetics, i.e., the diffusion path length, accounting for most of the mass transfer resistance, has to be negligible. Stacks of adsorptive membranes combine these properties of high capacity and small diffusion path lengths.

Membrane chromatography uses microporous membranes that contain functional groups attached to the surface of the internal pores. The feed is pumped through the membrane pores. Thus transport of the solute to the binding sites occurs predominantly by convection, and processing time is greatly reduced. The pressure drop is significantly lower compared to packed beds, as the flow path, even for a stack of multiple membranes, is much shorter. An important practical advantage is that scale up of membrane devices is easier than that of packed beds (Ghosh, 2002).

Membrane chromatography can be used to separate compounds varying from small molecules to large proteins. The mechanism by which membrane chromatography works varies depending on the ligand used to bind the target substrates. The four major types of adsorption membrane chromatography are equivalent in regards to removing the system

time lag as discussed in Chapter 2. These membrane chromatography types are affinity, reversed phase, hydrophobic interaction and ion exchange chromatography. A summary of pertinent membrane chromatography studies from literature is included in Table 1.1. The table summaries the functional groups used to absorb the solute (ligand), the structural membrane matrix, the absorbent (solute) bound to the membrane during the study, the solution complexity (simple is one or two solutes in buffer, complex is many solutes or cell lysates), the membrane configuration, and source of the data.

Chromatography systems as used in affinity, ion exchange, hydrophobic interaction, and reversed phase chromatographies are an adsorption / desorption process. "Chromatography" in these cases is a misnomer. The biotechnology industry as a whole continues to refer to these modes of adsorption as "chromatography" and this will be the convention used in this work for the sake of consistency with the industry.

Both traditional chromatography and membrane chromatography use the same principles and method of operation to separate compounds. The chromatography system consists of two phases, a mobile phase and a stationary phase. The stationary phase consists of a ligand attached to either the resin bead or the membrane. The mechanical matrix provided by the resin or membrane provides the mechanical strength and flow distribution characteristics for the chromatography system. The mobile phase is the solvent that flows continuously through the packed resin bed or the membrane. The composition of the mobile phase depends on the type of chromatography being used and

may change over time during the separation. For most applications, the stationary phase is used for many separation cycles before being replaced.

The chromatography separations used in this work are a batch operation where the substrate is loaded onto the ligands by flowing the sample through the matrix. When using affinity, ion exchange, hydrophobic interaction, or reversed phase chromatographies, the individual molecules bind to the ligands lining the pores. Under typical sample loading conditions, the substrate binds tightly to the ligand. After the sample is loaded, the mobile phase is changed from the sample loading conditions to a condition where the substrate bound to the ligands will release from the ligands and elute from the chromatography system. Typically, gradients in changing polarity, pH, or ionic strength are used to effect protein separations. Alternately, a step change in the mobile phase properties (e.g., polarity, pH, ionic strength) may be used instead of a gradient. The step change will generally elute multiple substrates at the same time and result in lower fraction purity and faster cycle time compared to a gradient elution.

Predictive modeling for solute concentrations during chromatography is critical for the scale-up of protein purification processes. The most common method for solute concentration in the permeate of a membrane chromatography system over time is the frontal analysis method. The frontal analysis method has been used to describe numerous solute / absorption membrane systems (Suen and Etzel, 1992; Suen and Etzel, 1994; Thömmes and Kula, 1995; Hao et al., 2004). The frontal analysis equation is based on a

mass balance over a section of membrane and typically has the following form (Suen and Etzel, 1992):

$$\textit{Unsteady state} + \textit{Convection} = \textit{Axial diffusion} - \textit{Adsorption} \tag{1.1}$$

Or in mathematical terms:

$$\varepsilon \frac{\partial c}{\partial t} + \varepsilon v \frac{\partial c}{\partial z} = \varepsilon D \frac{\partial^2 c}{\partial^2 z} - (1-\varepsilon)\frac{\partial c_s}{\partial t} \tag{1.2}$$

Where ε is the void fraction of the membrane, c is the solute concentration (M or g/ml), v is the velocity of the solution (m/s), z is a positional variable generally defined at the distance from the edge of the feed side of the membrane through the membrane (m), D is the diffusivity of the solute (m^2/s), and cs is the concentration of the solute in/on the membrane (M, g/ml, or g/m^2). The current analytical predictive modeling used to generate breakthrough curves for membrane chromatography either assumes an average pore size or forces the pore size distribution to be a continuous function. Assuming the Hagen-Poiuseuille approximation is valid for the system, the flow through an individual pore is dependent on the radius of the pore to the fourth power. Small changes in the pore radius can lead to very significant changes in the flow distribution through the membrane and the efficiency of the membrane chromatography purification (Suen and Etzel, 1992). The "fit" of the continuous distribution to either the discrete pore size distribution or to the experimental data is vital to an accurate predictive model. Improvements in fitting the continuous distribution to the discrete pore size data may allow for improved agreement between experimental and predictive results.

Functional Group	Membrane Matrix	Absorbent	Solution Complexity	Membrane Configuration	Reference
Affinity Chromatography					
Streptococcal protein G (SPG)	Cellulose	Bovine IgG	Simple	Stack	Kochan et al., 1996
Cu(II), Zn(II), Ni(II), Co(II)	Hydrophilic copolymer carrying terdentate ligand iminodiacetic acid (IDA)	Cytochrome c (tuna heart, t-Cyt c), Cytochrome c (horse heart, e-Cyt c), Dog myoglobin (d-Myo)	Complex	Sheet, Stack	Reif et al., 1994
Cibacron Blue 3GA dye using 1,6-diaminohexane, 1,6-diaminohexane + ethylene glycol diglycidyl ether (EGDGE), 1,10-diaminohexane, and 1,10-diaminohexane + EGDGE spacers	Polyvinylidene difluoride	Lysozyme	Simple	Sheet	Suen and Tsai, 2000
Cibacron Blue 3GA dye	Cellulose	Lysozyme, Bovine serum albumin	Simple	Sheet	Suen and Chang, 1998
Protein A immobilized on S-layer lattice microparticles	Durapore GVLP	Human IgG	Complex	Microparticles and sheet	Weiner etal., 1993
Cibacron Blue 3GA dye using 1,10-diaminohexane spacers	Millipore Immobilon AV	Lysozyme	Simple	Plate and Frame	Tsai and Suen, 2001
Cibacron Blue 3GA dye using 1,10-diaminohexane spacers	Millipore Immobilon AV	Lysozyme, Bovine serum albumin	Complex	Plate and Frame	Tsai and Suen, 2001
Heparin	Sartorius Sartobind synthetic copolymer	Human recombinant antithrombin III (rATIII)	Complex	Sheet	Lutkemeyer et al., 1993
Antibodies	Poly[glycidyl methacrylate-co-ethylene dimethacrylate] (GMA-EDMA)	Recombinant Protein G	Complex	Sheet	Hagedorn et al., 1999
Cibacron Blue immobilized on Agarose microparticles	Millipore Durapore	Human serum albumin, lysozyme	Simple	Microparticles and sheet	Herak and Merrill, 1990
Protein A immobilized on Agarose microparticles	Millipore Durapore	Immunoglobulin G	Simple	Microparticles and sheet	Herak and Merrill, 1990

Table 1.1: Pertinent membrane chromatography studies *(continued next page).*

Functional Group	Membrane Matrix	Absorbent	Solution Complexity	Membrane Configuration	Reference
Concanavalin A immobilized on Agarose microparticles	Millipore Durapore	Horseradish Peroxidase	Simple	Microparticles and sheet	Herak and Merrill, 1990
Cibacron Blue 3GA dye	Poly[ether sulfone] with various polysaccharides	Lysozyme	Simple	Hollow Fiber	Suen et al., 2000
L-amino acid (10 different)	Polyethylene (PE) with grafted glycidyl methacrylate (GMA)	Chiral amino acids	Simple	Hollow Fiber	Kiyohara et al., 1996
Phenylalanine (Phe), Tryptophan (Trp)	Polyethylene (PE) with grafted glycidyl methacrylate (GMA)	Bovine γ-globulin (BGG)	Simple	Hollow Fiber	Kim et al., 1991
Papain	Mercerized and non-mercerized macroporous cellulose	Papain inhibitors	Complex	Stack	Guo and Ruckenstein, 2002
Maltose	Macroporous cellulose	Concanavalin A	Simple	Stack	Guo and Ruckenstein, 2001
Protein A	Chitosan/coarse filter paper	Human IgG	Simple	Sheet	Yang and Chen, 2002
Protein A	Blend of polyethersulfone (PES) and polyethylene (PEO) coated with hydroxyethylcellulose (HEC)	IgG	Simple	Hollow Fiber	Charcosset et al., 1995
Reversed Phase					
No additional activation	Poly[styrene-co-divinylbenzene] (ST-DVB)	Albumin, human serum albumin	Complex	Sheet	Tennikova and Svec, 1993
No additional activation	Polyvinylidene fluoride	Cytochrome c	Simple	Sheet	Li et al., 2002
Hydrophobic Interaction Chromatography					
C4, C8	Poly[glycidyl methacrylate-co-ethylene dimethacrylate] (GMA-EDMA)	Ovalbumin, Ribonuclease, Lysozyme	Complex	Sheet	Tennikova et al., 1991
No additional activation	Dodecyl methacrylate-glycidyl methacrylate-co-ethylene dimethacrylate (DMA-GMA-EDMA)	Myoglobin, ribonuclease A, lysozyme, chymotrypsinogen	Complex	Sheet	Tennikova and Svec, 1993

Table 1.1: Pertinent membrane chromatography studies *(continued next page)*.

Functional Group	Membrane Matrix	Absorbent	Solution Complexity	Membrane Configuration	Reference
Quick Disk C4 from Saulentechnik Knauer	Quick Disk C4 from Saulentechnik Knauer	Human tumor necrosis factor α (TNF-α)	Complex	Sheet	Luksa et al., 1994
Phenyl or butyl group grafted to poly[glycidyl methacrylate] chain	Polyethylene	Bovine serum albumin (BSA)	Simple	Hollow fiber	Kubota et al., 1997a
Phenyl or butyl group grafted to poly[glycidyl methacrylate] chain	Polyethylene	Bovine serum albumin (BSA)	Simple	Hollow fiber	Kubota et al., 1997b
n-Decanol (supported liquid membrane)	Polyvinylidene fluoride (PVDF)	CAMPATH-1G monoclonal antibody, bovine serum albumin (BSA)	Complex	Sheet	Ghosh, 2001
Ion Exchange					
Ionogenic sulphopropyl groups	Poly[glycidyl methacrylate-co-ethylene dimethacrylate] (GMA-EDMA)	Ovalbumin, Ribonuclease, Lysozyme	Complex	Sheet	Tennikova et al., 1991
Diethylamine (DEA)	Poly[glycidyl methacrylate-co-ethylene dimethacrylate] (GMA-EDMA)	Myoglobin, conalbumin, albumin, trypsin inhibitor	Complex	Sheet	Tennikova and Svec, 1993
Sulfonic group	Cellulose (Sartorius S5, S15, S100)	IgM	Complex	Sheet, Stack	Santarelli et al., 1998
Quaternary ammonium group	Cellulose (Sartorius Q5, Q15, Q100)	IgM	Complex	Sheet, Stack	Santarelli et al., 1998
Sulfonic group	Sartorius Sartobind synthetic copolymer (S)	Monoclonal Antibodies (MAbs), Human recombinant antithrombin III (rATIII)	Complex	Sheet	Lutkemeyer et al., 1993
Quaternary ammonium group	Sartorius Sartobind synthetic copolymer (Q)	Monoclonal Antibodies (MAbs), Human recombinant antithrombin III (rATIII)	Complex	Sheet	Lutkemeyer et al., 1993
Amine modified	Sartorius Sartobind synthetic copolymer (A)	Monoclonal Antibodies (MAbs), Human recombinant antithrombin III (rATIII)	Complex	Sheet	Lutkemeyer et al., 1993
Quick Disk Q from Saulentechnik Knauer	Quick Disk Q from Saulentechnik Knauer	Human tumor necrosis factor a (TNF-a)	Complex	Sheet	Luksa et al., 1994

Table 1.1: Pertinent membrane chromatography studies *(continued next page).*

Functional Group	Membrane Matrix	Absorbent	Solution Complexity	Membrane Configuration	Reference
Quaternary ammonium (Q-SE) group	Poly[glycidyl methacrylate-co-ethylene dimethacrylate] (GMA-EDMA)	Plasmid DNA	Simple	Sheet	Giovannini and Freitag, 1998
Diethylaminoethyl (DEAE-AE) groups	Poly[glycidyl methacrylate-co-ethylene dimethacrylate] (GMA-EDMA)	Plasmid DNA	Simple	Sheet	Giovannini and Freitag, 1998
Cellulose phosphate	Whatman P81	Lysozyme	Simple	Plate and Frame	Lin and Suen, 2002
Diethylaminoethyl (DEAE) cellulose	Whatman DE81	Bovine serum albumin (BSA)	Simple	Plate and Frame	Lin and Suen, 2002
Diethylamine (DEA)	Glycidyl methacrylate	Bovine serum albumin (BSA)	Simple	Hollow fiber	Kubota et al., 1997c
Diethylamine (DEA)	Glycidyl methacrylate	Bovine serum albumin (BSA)	Simple	Hollow fiber	Kubota et al., 1997c
Ethanolamine	Glycidyl methacrylate	Bovine serum albumin (BSA)	Simple	Hollow fiber	Kubota et al., 1997c
Ethanolamino (EA) group	Polyethylene (PE) with grafted glycidyl methacrylate (GMA)	Bovine serum albumin (BSA)	Simple	Hollow fiber	Kubota et al., 1996
Sulfonic acid	Polyethersulfone (PES) Mustang-S from Pall	AMP, lysozyme, thyroglobulin	Simple	Stack	Teeters et al., 2002
Sulfonic Group (Sartobind-S)	Nylon, Modified cellulose	Lysozyme, Bovine serum albumin (BSA)	Simple	Stack	Gebauer et al., 1997

Table 1.1: Pertinent membrane chromatography studies. Summary of the functional groups, membrane matrix, absorbent (solute), solution complexity and membrane configuration of a selection of pertinent literature references for membrane chromatography. Numerous membrane configurations, functional group ligands, and membrane matrices have been evaluated experimentally for protein separation and the isolation of antibodies.

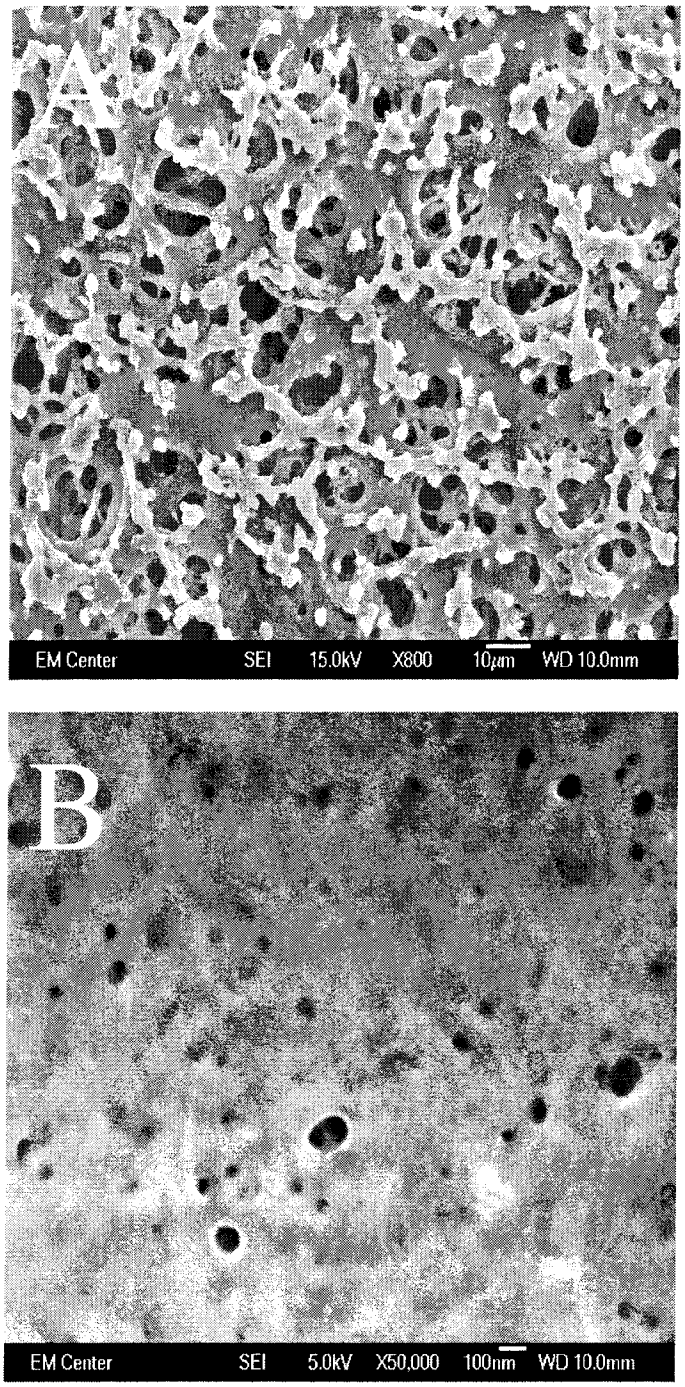

Figure 1.1: SEM images of A) Sartorius Q microfiltration membrane (Goettingen, Germany) and B) Millipore (Bedford, MA) ultrafiltration membrane with a nominal 500 kDa molecular weight cut-off. The pores in the microfiltration membrane are much larger than the ultrafiltration membrane.

1.3 Microfiltration and ultrafiltration

Microfiltration and ultrafiltration are unit operations that separate solutes in solution based on physical size. Solutes small enough to pass through the pores in the membranes travel with the solution to the permeate side of the membrane while larger solutes are physically prevented from passing through the membrane. When the solutes are within an order of magnitude of the pore size, the solutes are "hindered" in permeating the membrane and the flux of solute is reduced.

The primary difference between microfiltration and ultrafiltration is the size of the pores through the membrane. Due to the differences in average pore size, the two types of membranes have different industrial applications. Both types of membranes can be operated in two modes. First, the membranes can be operated in a concentration mode where the solute of interest does not pass through the membrane. As solution permeates the membrane, the solute of interest is concentrated on the retentate side of the membrane. Second, the membrane can be operated in a diafiltration mode where the solute of interest permeates the membrane. Since the concentration of the solute is the same on the retentate and permeate side of the membrane, the recovery of the solute of interest is limited to the fraction of the feed liquid volume recovered as permeate. This limitation can be overcome by adding additional clean buffer to the feed to make up the volume lost as permeate. This mode of operation recovers more of the solute of interest at the cost of diluting the concentration of the solute in the permeate.

Microfiltration membranes contain pores from 0.1 to 10 μm in diameter and are used in biotechnology applications primarily to remove cellular debris from lysed cells as a part of biomolecule purification (diafiltration mode). Ultrafiltration membranes contain smaller pores from 0.1 to 100 nm in diameter and are used in biotechnology applications to separate small from large proteins (diafiltration mode for small proteins, concentration mode for large proteins) or for buffer exchange. Buffer exchange is a combination of concentration mode with diafiltration operation. Clean buffer of a different type is added to the feed solution to make up permeate volume while the solute of interest is completely rejected by the membrane. Over time, the original buffer is displaced by the new buffer and the solutes are transferred to the new buffer.

Figure 1.1 contains a scanning electron micrograph of a microfiltration and ultrafiltration membrane for visual size comparison of the two membrane types. Ultrafiltration was used in this work to study the modeling of pore size distributions. Ultimately, methods learned through ultrafiltration pore distribution modeling can be applied to microfiltration and membrane chromatography.

1.4 Sucrose hydrolysis and degradation

The sucrose hydrolysis and degradation kinetic studies presented in this work not only have scientific merit on their own, but potentially have much greater significance when viewed in context of the continued research into the conversion of cellulosic biomass to ethanol and/or other high value chemicals. Currently, there is an on-going discussion on the future of the world's petroleum supply: how much there is, how fast the earth's

population will consume it, and the geographical and geopolitical environments of the oil production regions. Despite many predictions, no one knows the answers to these questions. Two things are certain: the population of the earth will continue to consume petroleum and its supply is finite. Ethanol from cellulosic biomass is one source of renewable energy being heavily investigated to displace gasoline as a transportation fuel and relieve some of the pressure on the petroleum reserves (Ragauskas et al., 2006; Farrell et al., 2006).

To date, the efficiency of liberating fermentation sugars from cellulosic biomass is based on glucose generated from the de-polymerization of cellulose and/or xylose from the de-polymerization of hemi-cellulose (Schell et al., 2003). Incorporation of sucrose hydrolysis and degradation kinetics into the selection of biomass pre-treatment conditions has the potential to increase the overall yield of ethanol and other biomass chemicals. By optimizing the pre-treatment conditions around maximizing the cellulose-derived glucose, hemi-cellulose derived xylose, and sucrose derived fructose and glucose the net yield of fermentation sugars can be increased and the concentration of fermentation inhibitors decreased to improve the efficiency of the overall biomass conversion process.

1.5 Outline of contributions

The research incorporated in this work is presented as three independent chapters. Each chapter is self-contained with an abstract, introduction, materials and methods, results and discussion, and conclusion section. Each chapter contains one or more novel approaches to improving the modeling of a physical system by incorporation or removal

of apparatus effects or enhancement of the algorithm used to determine the pertinent parameters.

Chapter 2 focuses on the removal of the apparatus system time-lag from membrane chromatography breakthrough curves. Removing the time-lag from the breakthrough curves dramatically improved the agreement of the isotherms measured under static and dynamic conditions and demonstrated a marked improvement in the dimensionless scale-up of a 5 cm^2 membrane holder to a commercially available 100 cm^2 membrane holder.

Chapter 3 details the use of scanning electron microscopy to image the surface of an ultrafiltration membrane. The images are used to construct a discrete pore size distribution. The fitting of a log-normal continuous distribution to the discrete data is improved by determining the continuous distribution parameters from the discrete normalized flow distribution instead of the discrete pore size distribution.

Chapter 4 improves on the determination of Arrhenius kinetic model parameters for fructose and glucose degradation kinetics by incorporating the reaction sample heating and cooling temperature profiles. Chapter 4 also includes two different methods for fitting the parameters: one appropriate when extensive degradation occurs under the reaction kinetics (fructose) and one when less significant degradation occurs (glucose). Additionally, fructose and glucose degradation products are measured and the accuracy of the degradation pathway model is discussed.

Chapter 2

THE MODELING AND ELIMINATION OF TIME-LAG FROM MEMBRANE CHROMATOGRAPHY SYSTEMS.

2.1 Abstract

The time lag created by the column peripherals and the column flow distribution headers was modeled for a membrane chromatography system using a Sartorious Q-membrane and bovine serum albumin (BSA) as the model protein. The time lag was modeled as a combination of a zero order time delay and a first order time delay. A numerical method was applied that removed the zero order and first order time delays from the breakthrough curve without requiring knowledge of the shape or characteristics of the breakthrough curve without the time delay. The method was applied to the calculation of Langmuir isotherm parameters collected under flow conditions. The membrane capacity without accounting for the system time delay was calculated as twice as large as the membrane capacity with the time lag removed. The Langmuir constant was five times as large for the system including the time delay as the system with the time delay removed or determined under non-flow (batch) conditions. Large errors in the fitting of isotherm parameters can significantly impact frontal analysis methods and membrane system scale-up exercises. The Langmuir isotherm calculated under dynamic flow conditions

with the time delay removed closely matched the Langmuir isotherm under static (no flow) conditions.

2.2 Introduction

The term chromatography is frequently used in the biotechnology industry to describe all packed bed separation processes. Membrane chromatography utilizes microporous membranes containing functional groups attached to the surface of the internal pores to bind solutes out of solution. The feed solution is pumped through the membrane pores and thus transport of the solute to the binding sites occurs predominantly by convection, an important advantage over traditional chromatography resins where diffusion of the solute into the resins requires long processing times. Membrane chromatography can be used to separate compounds varying from small molecules to large proteins [Roper and Lightfoot, 1995; Thömmes and Kula, 1995; Charcosset, 1998; Zeng and Ruckenstein, 1999; Klein, 2000; Ghosh, 2002].

The physical construction of chromatography systems can create time delays. Fluid requires time to flow through the tubing connecting the pump to the column distribution head. The distribution head and collection head of the column or membrane holder create void volumes and non-uniform residence times that diffuse sharp solute gradients [Yuan et al., 1999]. These time lag effects impact the time required for the breakthrough to occur and broaden the shape of the chromatography breakthrough curves, respectively. Table 2.1 outlines system lag models and their use in pertinent literature. The sharpness of the breakthrough curve can be used as a measure of the system efficiency.

System Lag Model	Experimental Method	Model use	Reference
Plug flow region plus continuous stirred tank region	Solute flow through system under non-binding conditions	Incorporated into predictive frontal analysis for breakthrough curve.	Suen and Etzel, 1994
Plug flow region plus continuous stirred tank region	Solute flow through system under non-binding conditions	Estimate dispersion in the flow system.	Kochan et al., 1996
Exponentially modified Gaussian distribution	Tracer pulse under non-binding conditions	Subtracted from effluent profile to determine one-dimensional plug flow and two-dimensional potential flow characteristics of the membrane column.	Roper and Lightfoot, 1995
Exponentially modified Gaussian distribution	Tracer pulse under non-binding conditions	Subtracted from effluent profile to eliminate bias generated from peripheral effects, header flow distribution and packing non-uniformity in chromatography scale-up.	Lode et al., 1998
Exponentially modified Gaussian distribution	Tracer pulse under non-binding conditions	Subtracted from effluent profile to eliminate bias generated from peripheral effects, header flow distribution and packing non-uniformity in evaluation of industrial scale resin chromatography columns.	Moscariello et al., 2001
Exponentially modified Gaussian distribution	Tracer pulse under non-binding conditions	Subtracted from effluent profile to eliminate bias generated from peripheral effects, header flow distribution and packing non-uniformity in evaluation of industrial scale membrane chromatography columns.	Teeters et al., 2002

Table 2.1: Previous time lag studies of traditional and membrane chromatography systems.

In an ideal system, the breakthrough curve is a step change from no solute in the permeate to the feed concentration of solute in the permeate. Breakthrough curves typically have an S-shape where solute concentration in the permeate gradually increase as more and more solute is loaded on to the active sites of the membrane. The broader the S-shape of the breakthrough curve the less efficient the utilization of binding capacity was for the chromatography (Suen and Etzel, 1992).

Time delays in the experimental breakthrough curves have been observed and included in frontal analysis models for membrane chromatography (Suen and Etzel, 1994, Kochan et al., 1996). The change in protein concentration over time resulting from a step change in the protein concentration in the feed was measured experimentally under non-binding conditions. The resulting protein concentration breakthrough curve contained two time delay components. These delays were termed delay volume and dead volume mixing effects and modeled as a plug flow region and continuous stirred tank region. The plug flow region is a zero order time delay (change in protein concentration per change in time is not dependent on protein concentration) and the continuous stirred tank region is a first order time delay (the change in protein concentration per change in time is a function of the protein concentration). The system time delays were modeled by empirically fitting experimental measurements under non-binding conditions to determine the characteristic volumes of the plug flow and continuous stirred tank regions. The time delays were incorporated into a frontal analysis model to describe protein breakthrough curves under binding conditions.

Suen and Etzel (1994) evaluated the impact of sorption kinetics on the breakthrough curve of pepsin and chymosin using a pepstatin A affinity membrane. Kochan et al. (1996) also used a combination of plug flow regions and continuous stirred tank regions to model the system lag impact on the breakthrough curves for bovine immumoglobulin G binding to protein G affinity membranes as a means to evaluate dispersion in the flow system. Dead volume mixing effects were observed under non-binding conditions by Hoa et al. (2004) during modeling of a membrane chromatography system but were deemed small enough to be negligible and were not incorporated into the frontal analysis, ideal stirred tank, or modified stirred tank predictive models.

The dispersion of an instantaneous pulse input under non-binding conditions has been used in both membrane chromatography and traditional resin based chromatography to measure the impact of radial and axial diffusion on fluid flow through the system. Pulse trace methods were used by Roper and Lightfoot (1995) to estimate the relative impact of one-dimensional plug flow (micro-scale fluid-phase mixing, Fickian convection) and two-dimensional potential flow on the broadening of effluent profiles in membrane chromatography. The broadening of the peaks was fit to modified Gaussian distributions. Extra-column effects (pre-column tubing, fittings, and injection valves) were measured experimentally, fit to a modified Gaussian distribution, and mathematically manipulated to remove the effects from the effluent profile and isolate peak-broadening effects within the stacked membrane column. This work was continued and applied to chromatography scale-up (resin and membrane) by Lode et al. (1998) and as a means to characterize the performance of industrial-scale columns by Moscariello et al. (2001) and Teeters et al.

(2002). In these cases, no actual binding of the tracer to the stationary phase occurred and the method required the tracer to flow through the system in both the forward and reverse directions at different times. The instantaneous pulse input method is not suitable for conditions where non-reversible binding occurs such as in adsorption chromatography since the pulse tracer would bind to the resin or membrane and not flow through the column. The pulse trace method can be used in systems with highly reversible solute/stationary phase interactions such as size exclusion chromatography (Lode et al., 1998).

To date, the time lag created by the physical membrane chromatography system incorporated into membrane chromatography models has required detailed knowledge of the binding kinetics, diffusion kinetics, and other parameters of the solute-membrane interaction. The time lags were incorporated into membrane chromatography models and used to predict the shape of the breakthrough curves. The predicted breakthrough curves were evaluated against the experimental breakthrough curve to determine the quality of the model. The work reported here shows how the system time lag can be removed from the experimental breakthrough curve data without detailed knowledge of the shape of the breakthrough curve in the absence of the system time lag. The method is applied to experimental data to demonstrate the impact of the system time lag on the calculation of Langmuir isotherm parameters.

2.3 Materials and Methods

Bovine serum albumin (BSA) was purchased from Sigma-Aldrich (St. Louis, MO, USA). Protein solutions were prepared by dissolving BSA in 0.01 M sodium phosphate buffer

and titrating to pH 7.0 using concentrated hydrochloric acid. Equilibration and washing buffer was 0.01 M sodium phosphate (pH 7.0).

Sartorius Q membranes (Goettingen, Germany) were used as the model ionic protein absorber. Single sheets of circular membrane with an area of 5 cm^2 (35 mm diameter) were cut from sheets of membrane and held in a Sartorius 6 mbH D-3400 membrane holder. All experiments using the 5 cm^2 membrane holder were conducted using a single layer of Q membrane. Additional scale-up experiments were conducted using a Sartorius Sartobind Q 100 prepackaged membrane module. The Sartobind Q 100 contained 5 layers of stacked membranes with a total of 100 cm^2 of cross-sectional membrane surface area. Protein was eluted from both membrane systems using 1.0 M sodium chloride in 0.01 M sodium phosphate buffer at pH 7.0.

The breakthrough curves were generated using a Waters 501 HPLC pump (Wilford, MA) and a Waters 474 Scanning Fluorescence Detector. The fluorescence detector was set to excite at 275 nm and to detect emissions at 340 nm to measure the tryptophan amino acids in the BSA. The detection band width was 18 nm with an attenuation of 1.0. The HPLC pump was controlled by and the data logged with Maxima 820 (Dynamic Solutions of Millipore, Billerica, MA) software. The fluorometer reading (in millivolts) was automatically recorded every 5 seconds for the duration of the experiment. Standards of known BSA concentrations were prepared and used to calibrate the fluorometer signal. All breakthrough curves were generated at an ambient temperature of approximately 22 °C.

2.3.1 Normal Membrane Chromatography Operation

Normal operation of the membrane chromatography system in this work involves three steps. In the first step, protein is loaded onto the membrane absorber by pumping a protein and buffer solution through the porous membrane. Protein in solution binds to the membrane while the buffer passes through. As the membrane saturates, protein "breaks through" the membrane and is detected by the fluorometer in increasing concentrations. For these experiments, the membrane chromatography system was operated until the membrane was completely exhausted and the protein concentration in the permeate was the same as the inlet protein concentration, i.e., no additional protein bound to the membrane. Operation of the membrane chromatography system in this manner was different than membrane chromatography used for purification which typically would be stopped once the protein concentration in the permeate reached 10% of its inlet concentration. The second step of the chromatography uses buffer without protein to "wash" the un-absorbed protein out of the membrane pores. The final step is to elute the absorbed protein off of the membrane and into the permeate stream using 1 M sodium chloride in buffer. The three steps have distinct protein concentration patterns as shown in Figure 2.1.

2.3.2 Static Isotherms

Five different BSA concentrations were prepared (40, 100, 205, 360, and 560 μg/ml) in 0.01 M phosphate buffer, pH 7.0. Approximately 1 cm^2 squares of Q-membrane was added to 20 ml of BSA solution in a sealed vial and placed on a shaker table for 24 hours

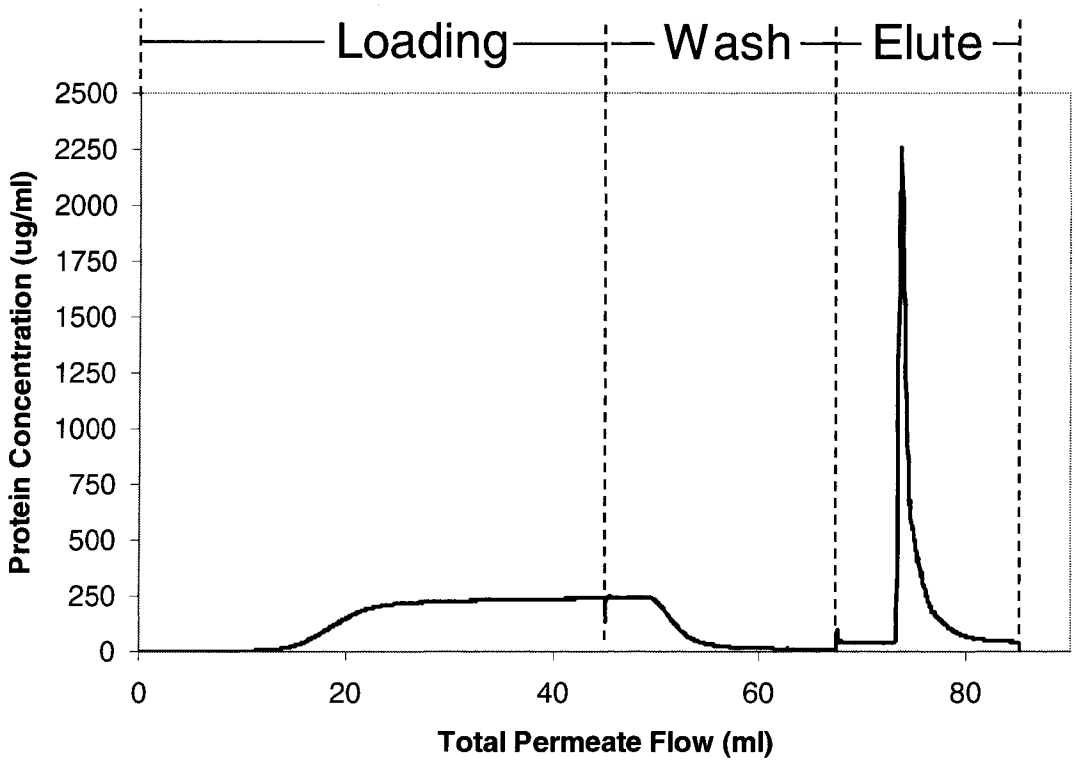

Figure 2.1: The three steps of membrane chromatography illustrated with an experimental chromatogram. The membrane was loaded using 250 μg/ml BSA in 0.01 M phosphate buffer at pH 7.0. The membrane was washed with 0.01 M phosphate buffer at pH 7.0. The protein was eluted from the membrane with 1 M sodium chloride in 0.01 M phosphate buffer at pH 7.0.

at room temperature (approximately 22 °C). Each Q-membrane sample was weighted on an analytical scale to determine the exact volume of the membrane used in each vial. The bulk protein concentration was measured before and after adding the Q-membrane to determine the amount of protein absorbed onto the membrane using the Waters 474 Scanning Fluorescence Detector (275 nm excitation, 340 nm detection). Each BSA concentration was evaluated in triplicate and each bulk concentration for each sample was measured in duplicate and averaged.

2.3.3 Zero and First Order Time Lag Correction

Zero-order time-lag (plug flow region) is removed from the breakthrough curve by deleting the equivalent volume (or time) from the beginning of the experimental data and re-indexing starting at 0. The zero-order time-lag is measured as total permeate flow (equivalent volume = time * flow rate) in this work but it is equally correct to measure the zero order system lag in units of time (i.e. minutes). The time-lag units can be interchanged by multiplying or dividing, as appropriate, by the constant flow rate (ml/min). The units used for the time axis in this work were total permeate flow through the membrane.

The first-order time lag (continuous stirred tank region) correction is accomplished according to the method published by Miloshevich et al. (2004) for removing the first order time delay from measurements using atmospheric humidity detectors. The system time lag for the humidity detectors is caused by the requirement for water molecules to diffuse through a polymer layer. The water molecule diffusion rate is proportional to the

water molecule concentration in the atmosphere and introduces a first order time delay into the measurement system. The change in protein concentration in a continuous stirred tank is also dependent on the inlet protein concentration and creates a first order time lag that is mathematically similar to the first order time lag observed in the atmospheric humidity detector. The method is based on measuring the change in a reading over a fixed period of time and using the known time constant τ to estimate the actual change required to drive the observed measured change. The measured change in the protein concentration (C_m) is a function of the actual protein concentration (C_a) and a constant k according to the exponential growth-law equation:

$$\frac{dC_m}{dt} = k(C_a - C_m) \tag{1}$$

Applying a step change in the protein concentration at time equals t_0, the equation can be rearranged to separate the variables and then integrated.

$$\frac{dC_m}{(C_m - C_a)} = -kdt \tag{2}$$

$$\int_{C_{mo}}^{C_m} \frac{dC_m}{(C_m - C_a)} = \int_{t_O}^{t_f} -kdt \tag{3}$$

$$\ln(C_m - C_a) - \ln(C_{mo} - C_a) = -k(t_f - t_o) \tag{4}$$

Substituting the total time change for the final time minus the initial time, $\Delta t = (t_f - t_o)$, and combining the terms on the left side of the equation yields:

$$\ln\left(\frac{(C_m - C_a)}{(C_{mo} - C_a)}\right) = -k\Delta t \tag{5}$$

$$\frac{(C_m - C_a)}{(C_{mo} - C_a)} = \exp(-k\Delta t) \tag{6}$$

$$(C_m - C_a) = (C_{mo} - C_a)\exp(-k\Delta t) \tag{7}$$

Substituting k = 1/τ and solving for C_m generates an equation for the measured protein concentration as a function of time:

$$C_m(t) = C_a - [C_a - C_{mo}]e^{-\Delta t/\tau} \tag{8}$$

The τ value in Equation 8 is a measured value for the particular system being studied and is used to remove the time lag from the experimental data. It is the time required for the system output to read 63% of the magnitude of a step function change in the input. The value for τ can be calculated directly for a perfectly mixed continuous stirred tank region. The equation describing the solute concentration in the discharge of an ideal continuous stirred tank after a step change from zero to one normalized solute concentration in the inlet is:

$$\frac{C}{C_O} = 1 - \exp\left(-\frac{F}{V}\Delta t\right) \tag{9}$$

Where F is the flow rate in ml/min and V is the volume of the tank in ml. Rearranging and solving for Δt when $C/C_O = 0.63$:

$$\exp\left(-\frac{F}{V}\Delta t\right) = 1 - \frac{C}{C_O} \tag{10}$$

$$\frac{F}{V}\Delta t = -\ln\left(1 - \frac{C}{C_O}\right) = \ln(1 - 0.63) = 1 \tag{11}$$

$$F\Delta t = V \tag{12}$$

In this work, time is measured as total permeate flow, $F\Delta t$. Therefore, τ = V for the continuous stirred tank region of the system time lag.

The first-order system time lag is removed from the experimental data by assuming that the time step Δt is sufficiently small that C_a is effectively constant and solving Equation 2 for C_a using the measured protein concentration and the beginning of the time step ($C_m(t_0)$) to the end of the time step ($C_m(t_f)$). The resulting equation has the form:

$$C_a = \frac{C_m(t_f) - \left[C_m(t_0) e^{-\Delta t/\tau}\right]}{1 - e^{-\Delta t/\tau}} \tag{13}$$

The numerical method utilized for removing the first-order system time lag from the experimental breakthrough curve sequentially applies Equation 13 to the breakthrough curve data at each time point after the zero-order plug flow time delay is removed. The resulting curve of C_a over time frequently contains an oscillation due to the discrete nature of the digital signal and signal noise. The estimated actual protein breakthrough curve with the first-order and zero-order time delays removed is contained in and bounded by the oscillation.

2.3.4 Curve Smoothing

The estimated actual breakthrough curve is recovered from the oscillation through application of a smoothing algorithm. The smoothing algorithm is an iterative based method that allows the value of each data point to adjust up to a specified amount in order to minimize the third derivative and maintain a constant curvature where possible (Miloshevich et al., 2004). The third back-derivative of y calculated at point i+2 is notated as $D_3[i+2]$. The second back-derivative of y calculated at point i+2 is notated as $D_2[i+2]$. The value of $D_3[i+2]$ is calculated from Equation 14 and Equation 15:

$$D_3[i+2] = \frac{(D_2[i+2] - D_2[i+1])}{\Delta t[i+2]} \tag{14}$$

$$\Delta t[i+2] = t[i+2] - t[i+1] \tag{15}$$

The upper limit for the curve smoothing tolerance range for point i is $y_H[i] = y[i] + \Delta y[i]$. The lower limit for the curve smoothing tolerance range for point i is $y_L[i] = y[i] - \Delta y[i]$. The value of $\Delta y[i]$ is user-defined for each data point i in the data set. The tolerance range is not required to be symmetric but was symmetric in this work. The smoothed data point calculated from the method is designated as $y_S[i]$. The data is smoothed by sequentially proceeding through the data set calculating the value of $y_S[i+1]$ in the range of $y_H[i+1]$ to $y_L[i+1]$ that minimizes $D_3[i+2]$. The first iteration of the method uses the original experimental values, $y[i+2]$, for calculating $D_3[i+2]$. The second and subsequent iterations use the value for $y_S[i+2]$ from the previous iteration for calculating $D_3[i+2]$.

The numerical implementation of the smoothing algorithm calculates a critical curvature, $y_C[i+1]$, that yields $D_3[i+2] = 0$. When the critical curvature equals 0, $D_2[i+2] = D_2[i+1]$. Substituting for the second derivatives, rearranging, and calculating the resulting curvature yields:

$$y_C[i+1] = \frac{\left(D[i]\Delta t[i+2]^2\right) + \left(y[i+2]\Delta t[i+1]\right) + \left(y[i]\Delta t_{fac}\right)}{\Delta t[i+1] + \Delta t_{fac}} \tag{16}$$

$$\Delta t_{fac} = \left(\frac{\Delta t[i+2]}{\Delta t[i+1]}\right) \times \left(\Delta t[i+2] + \Delta t[i+1]\right) \tag{17}$$

If the calculated value $y_C[i+1]$ is within the range of $y_L[i+1] < y_C[i+1] < y_H[i+1]$, then $y_S[i+1] = y_C[i+1]$. If $y_C[i+1]$ is outside the tolerance range, then the maximum or minimum value, as appropriate, is accepted as the smoothed value. The smoothing

method is iterative and does not have a unique solution. The method is biased towards the direction y_S is calculated. To overcome the bias, the smoothed data curve is calculated in both directions, from t[0] to t[max] and in the reverse direction from t[max] to t[0]. The two resulting smoothed curves are averaged and the iteration is repeated using the averaged values for y_S for five iterations.

2.4 Results and Discussion

2.4.1 Modeling the System Time-Lag

The membrane chromatography system and model is outlined in Figure 2.2. The HPLC pump and tubing is modeled as a plug flow system, the membrane holder is modeled as a continuous stirred tank, and the fluorometer and associated tubing is modeled as an additional plug flow reactor as in Suen and Etzel (1994) and Kochan et al. (1996). For the mathematical modeling, the upstream and downstream plug flow reactors were combined as a single zero-order time delay.

The system lag was measured using a step input change in protein concentration through the membrane chromatography system without an adsorption membrane under non-binding conditions (Figure 2.3A). The system was brought to equilibrium using buffer without BSA. In order to evaluate the possible dependence of the system time-lag on inlet protein concentration, two different protein concentrations of 500 μg/ml and 10 μg/ml BSA in buffer solution were evaluated in separate trials. The resulting time-lag curves were normalized and are equivalent (Figure 2.3B). The system lag is not a function of protein concentration at a flow rate of 0.5 ml/min.

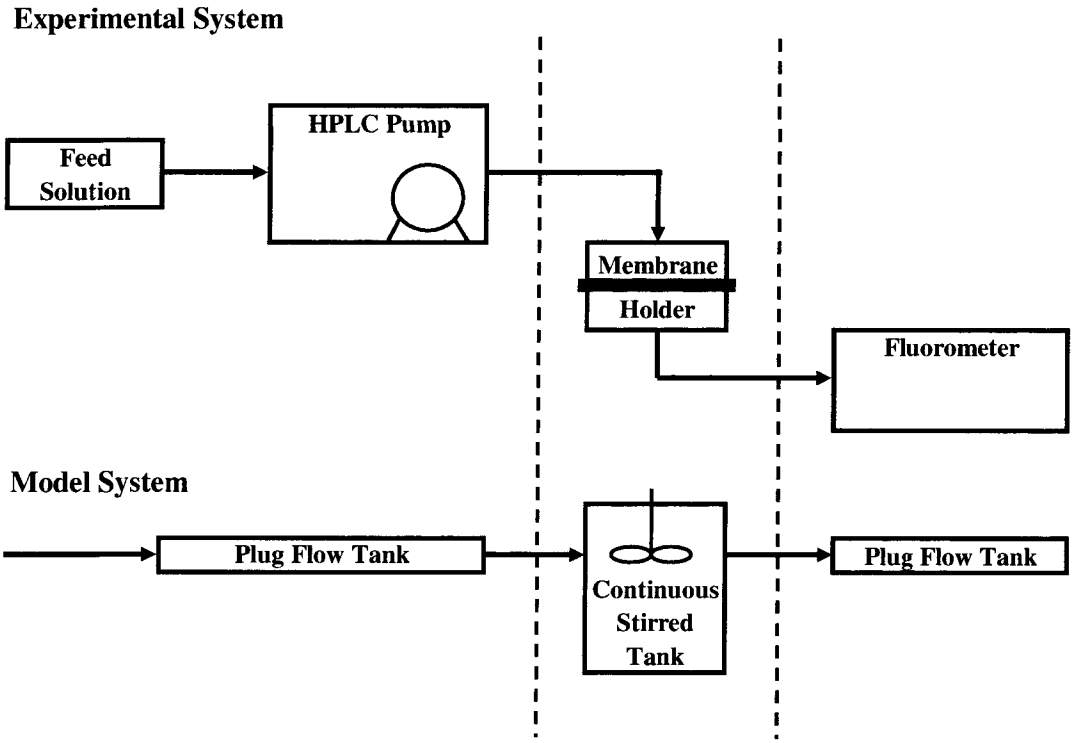

Figure 2.2: The experimental system and mathematical model for the membrane chromatography system.

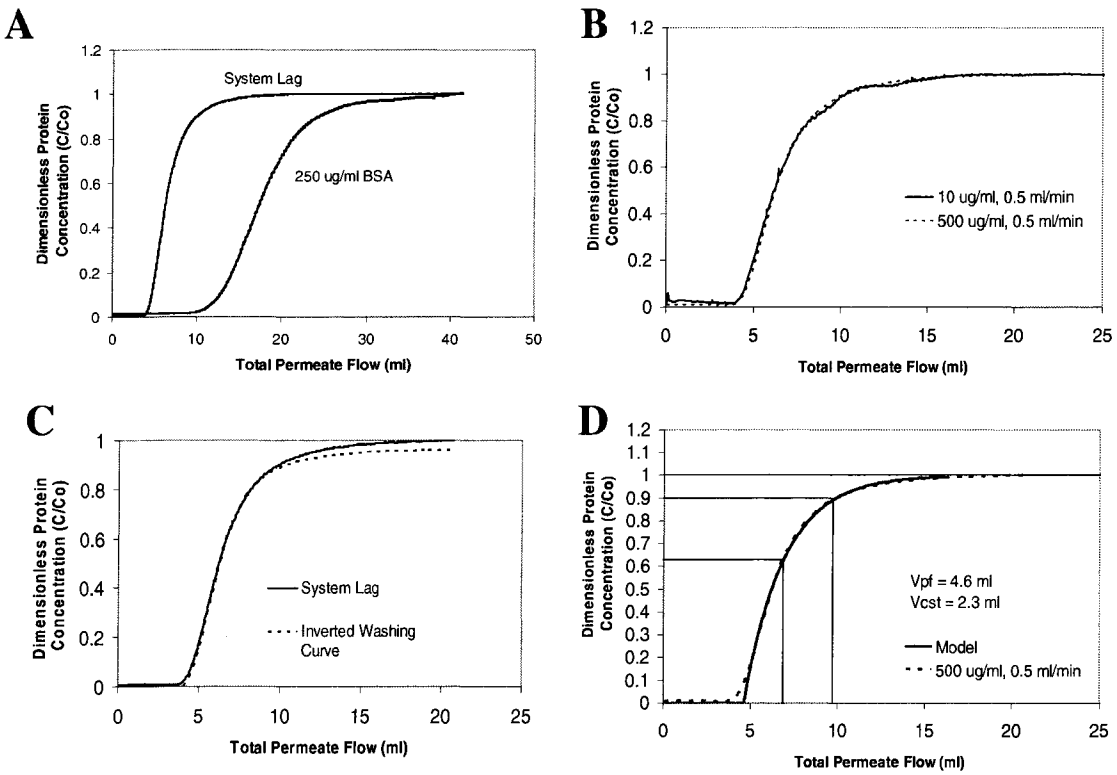

Figure 2.3: Evaluation of the time lag associated with the membrane chromatography system. (A) The measured protein concentration response to a step change from 0 to 1 (C/C_0) at a flow rate of 0.5 ml/min. The "system lag" curve was measured from a system without a membrane absorber (empty holder) and the "250 μg/ml BSA" curve was measured from a system with a single layer of Q membrane in the holder and an inlet protein concentration of 250 μg/ml BSA. The difference between the two curves was caused by BSA absorbing to the membrane. (B) The system lag measured without a Q membrane at 10 μg/ml and 500 μg/ml. Protein concentration in this range did not affect the measured system lag. (C) The system lag measured without a Q membrane was plotted vs. $1-(C/C_0)$ measured for the washing of a Q-membrane loaded with 250 μg/ml BSA solution. The two curves overlap indicating that a single layer of Q membrane does not appreciably add to the system lag. (D) The system lag was empirically modeled using a plug flow and continuous stirred tank system. The plug flow element has a volume of 4.6 ml and the continuous stirred tank has a volume of 2.3 ml. The two points highlighted on the curve indicate the 63% and 90% response times used for removing the system lag from the breakthrough curve.

The impact of the absence of the membrane during the time-lag measurements was evaluated by examining the washing step of the breakthrough curve. Upon saturation of the membrane, full inlet protein concentration is observed in the permeate. To wash the membrane of unbound protein, a step change to pure phosphate buffer is applied to the system. The resulting curve of decreasing protein concentration measured at the detector was used to evaluate the time-lag of the system. The washing curve was "inverted" by plotting the function of $1\text{-}C/C_O$ vs. time. The resulting plot was overlaid with the system-lag measured without the membrane (Figure 2.3C). The results overlap. The presence or absence of a single layer of Q-membrane does not significantly effect the overall time-lag of the system.

The PF-CST-PF model was empirically fit to the experimentally measured time-lag for the system to determine the total plug flow volume and effective volume of the continuous stirred tank (Figure 2.3D). The volume of the plug flow component of the model was 4.6 ml. The volume of the continuous stirred tank was 2.3 ml.

2.4.2 Time Lag Corrected Breakthrough Curve

The zero-order time-lag (plug flow volume) was removed from the breakthrough curve by deleting the first 4.6 ml of experimental permeate data from the original breakthrough curve data. All time points were re-indexing starting at 0. The resulting data was used as C_m. The first-order time delay was removed by sequentially applying Equation 13 to the re-indexed experimental data. The value for τ was determined for this system from the graph of the system lag model (Figure 2.3D). The 63% response (0.63

normalized protein concentration) occurred at a total flow of 6.9 ml. Subtracting the zero order time-lag of 4.6 ml yields $\tau = 2.3$ ml. A continuous stirred tank model has an ideal exponential response. As expected, the 90% response time of the model for a step input (0.9 normalized protein concentration) is 2.3 times the 63% response time when the zero order time delay is subtracted from the system. An oscillation was clearly visible in the resulting calculated C_a curve (Figure 2.4). The smoothing algorithm was applied to the calculated C_a curve as outlined in the *Materials and Methods*. The resulting smoothed C_a curve represents the BSA breakthrough curve through a Q-membrane at pH 7.0 and 0.5 ml/min flow rate with the time-lag caused by the chromatography system removed (Figure 2.4). The smoothed C_a breakthrough curve more accurately represents the protein flow through and adsorption to the Q-membrane than the experimental data.

The original breakthrough curve with the system lag included was recovered from the smoothed C_a curve by applying a first-order time delay ($\tau = 2.3$) and a zero order time delay of 4.6 ml using SIMULINK (MathWorks, Natick, Massachusetts, USA). The original breakthrough curve and reconstructed breakthrough curves are equivalent (Figure 2.5).

2.4.3 Membrane Capacity

The membrane capacity was determined by integrating the area between the breakthrough curve and inlet protein concentration. Two areas were determined from the breakthrough curves for each inlet protein concentration; the breakthrough curve not considering system lag and the breakthrough curve after removing the system lag. The

total protein was divided by the membrane surface area (5 cm^2) and membrane thickness (275μm) to determine Q, the protein concentration per volume membrane. The bulk protein concentration, C, was the concentration of the protein in the feed solution pumped through the membrane. The resulting areas are included in Table 2.2.

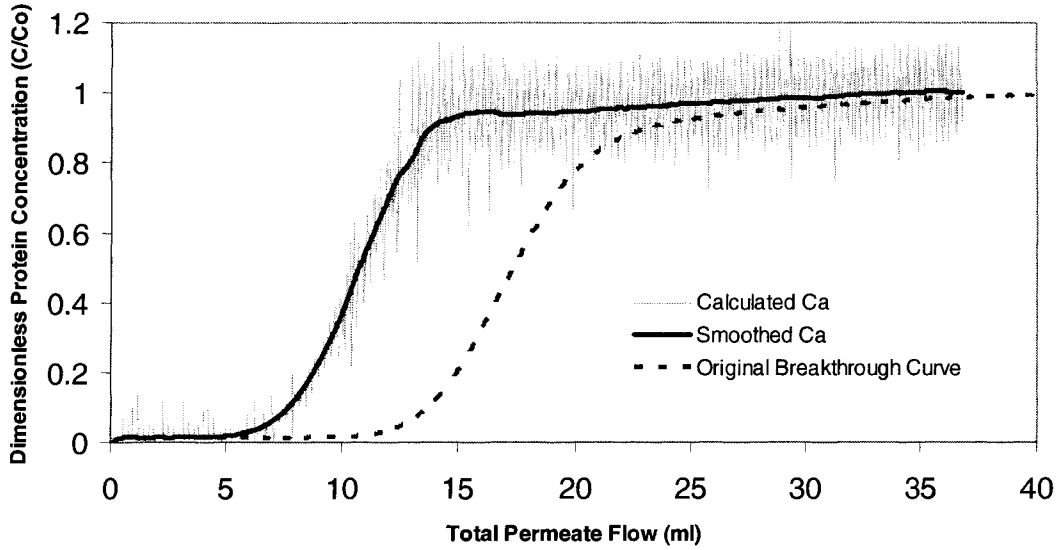

Figure 2.4: Removing the first order time delay. The zero order time delay of 4.6 ml was removed from the original breakthrough curve (not shown). The numerical method (Equation 13) was use to generate the calculated BSA concentration (C_a) as a function of time. The oscillation generated by the calculation is smoothed using an iterative numerical method based on minimizing the local third derivative.

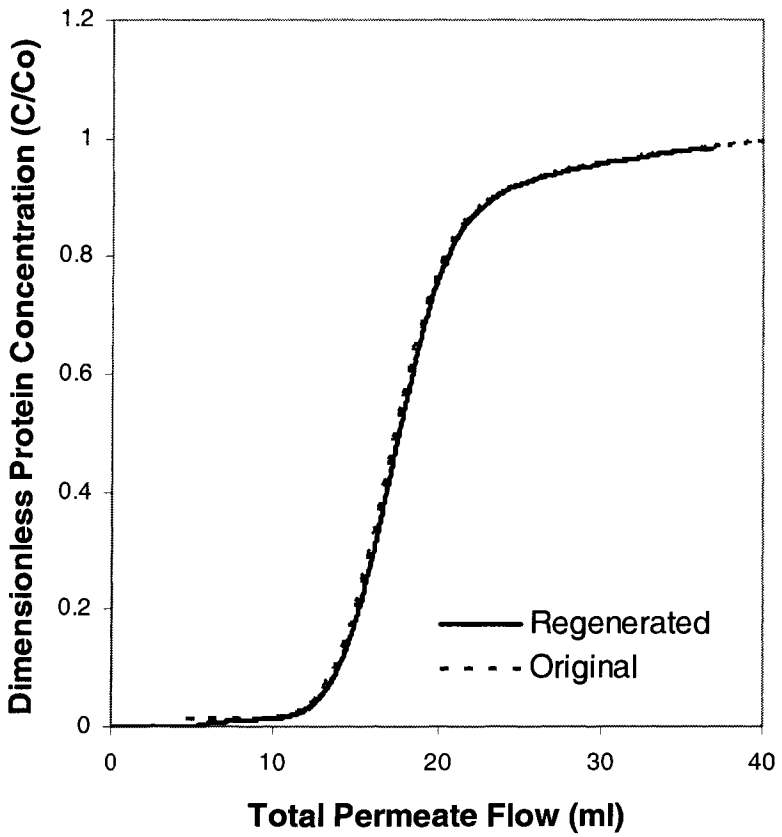

Figure 2.5: The zero order time delay (4.6 ml) and the first order time delay (τ = 2.3) were applied to the smoothed C_a curve using SIMULINK. The original experimental data was regenerated after applying the time delays.

Bulk Protein Concentration, C (μg/ml)	Uncorrected Membrane Concentration, Q (mg/ml)	System Lag Removed Membrane Concentration, Q (mg/ml)
50	20.8	18.3
150	28.9	21.5
250	35.6	23.2
350	38.8	21.3
500	48.7	23.6

Table 2.2: Membrane capacity determined by integration of the breakthrough curves generated for different inlet protein concentrations. The uncorrected values are generated from breakthrough curves still containing system lag. The system lag removed values are from the breakthrough curves with the system lag removed.

2.4.4 Langmuir Isotherms

Languir-type isotherms have been used extensively to model the absorption of protein or other solutes to ionic membranes. The Langmuir-type isotherm relates the solute concentration in the mobile bulk phase (C, mg/ml solution) to the solute concentration absorbed to the stationary solid phase (Q, mg/ml membrane) of the system under equilibrium conditions. Two constants are required, the maximum capacity of the membrane, Q_∞, and the Langmuir constant, K_d.

$$Q = \frac{Q_\infty C}{K_d + C} \tag{18}$$

The Langmuir-type isotherm under dynamic (flow) conditions was measured by comparing the total protein absorbed by the membrane to the protein concentration in the bulk phase for several different bulk phase protein concentrations (Shiosaki et al., 1994) by integrating the area over the breakthrough curve. Total membrane capacity was measured for 5 different inlet protein concentrations varying in range 10 to 500 μg/ml of BSA at 0.5 ml/min flow rate. The membrane capacity was determined both accounting for the system lag and not accounting for system lag (Table 2.2). Parameters for the Langmuir-type isotherm in each case were determined by linear transformation of the Langmuir-type isotherm (Equation 19) and plotting C/Q vs. C (Figure 2.6). This transformation has been shown to minimize the error in the parameters (Kinniburgh, 1986, Longhinotti et al., 1998). The slope of the linear regression is equal to $1/Q_\infty$ and the intercept is equal to K_d/Q_∞. The resulting Langmuir-type isotherm parameters obtained are listed in Table 2.3 and used to generate Figure 2.7.

$$\frac{C}{Q} = \frac{K_d}{Q_\infty} + \frac{C}{Q_\infty} \tag{19}$$

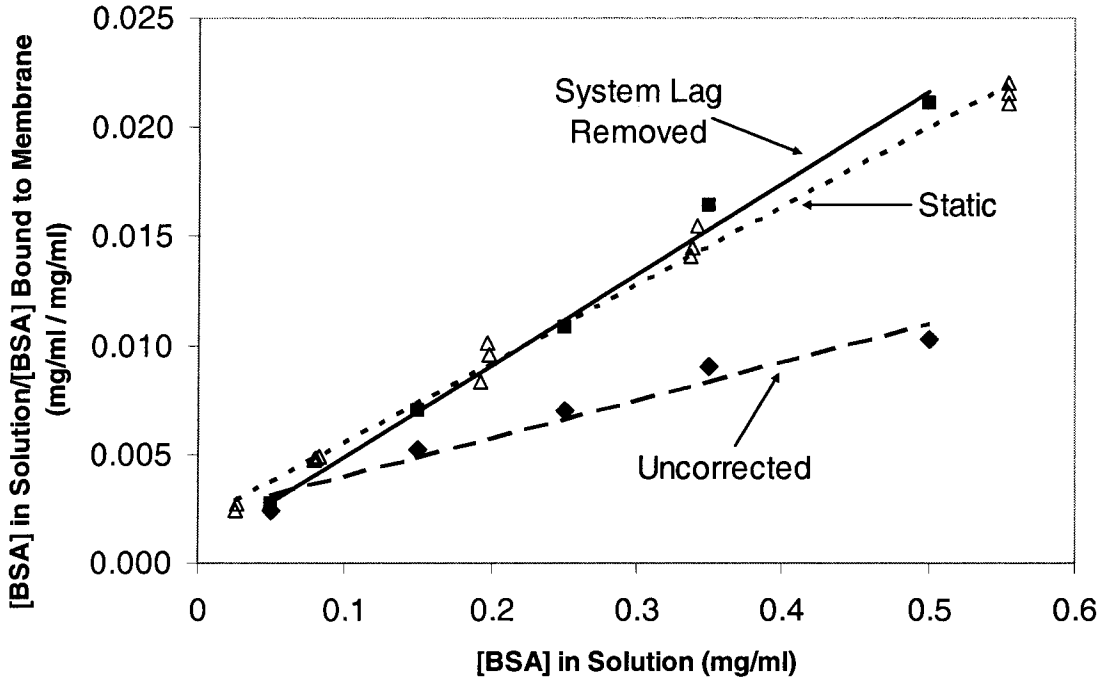

Figure 2.6: Plot of C versus C/Q for BSA/Q-membrane Langmuir-type isotherm linearization. The slope of each line is equal to $1/Q_\infty$ and the intercept is equal to K_d/Q_∞. The slope of the "System Lag Removed" regression was 0.0418 with an intercept of 0.00074 and a R^2 of 0.993. The slope of the "Uncorrected" regression was 0.0175 with an intercept of 0.00224 and a R^2 of 0.956. The slope of the "Static" regression was 0.0361 with an intercept of 0.00195 and a R^2 of 0.994.

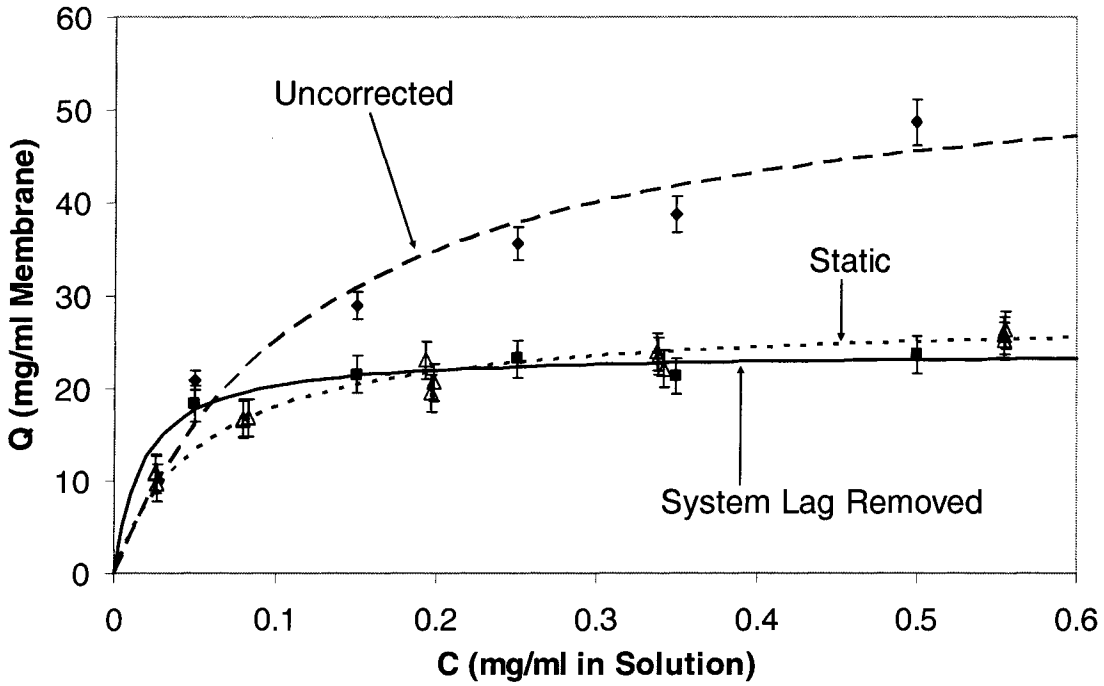

Figure 2.7: Langmuir-type isotherms for the uncorrected data, data with the system lag removed, and the static equilibrium data. The static isotherm closely agrees with the isotherm generated by removing the system lag.

Langmuir Isotherm Parameter	Uncorrected Membrane	System Lag Removed	Static Measurements
K_d (ml/mg)	6.49	33.3	18.5
Q_∞ (mg/ml)	67.8	28.8	27.2

Table 2.3: Langmuir-type isotherm parameters determined from regression of linearization.

Removal of the system time lag from the experimental breakthrough curves significantly impacted the calculated Langmuir-type isotherm parameters. The maximum membrane capacity, Q_∞, was twice as large for the "uncorrected" data (Table 2.3). The Langmuir constant, K_d, was five times as large for the "system lag removed" as the "uncorrected" data. The "system lag removed" data also fit a Langmuir isotherm better than the "uncorrected" data with a R^2 value of 0.993 compared to a R^2 value of 0.956. Most importantly, the "system lag removed" isotherm closely follows the static isotherm.

The large differences in the fit parameters between calculations including the system time lag and calculations with the time lag removed significantly impact subsequent calculations based on utilizing the isotherm data. The significant differences in the isotherm parameters may result in large errors in calculations such as frontal analysis methods and scale-up exercises.

2.4.5 Membrane Chromatography System Scale-Up

The effect of the system time lag on membrane chromatography scale-up was evaluated by generating breakthrough curves using a 100 cm^2 membrane module and comparing the results to the 5 cm^2 membrane holder on a dimensionless basis. All 4 breakthrough curves were generated with a BSA concentration of 250 μg/ml buffer in the feed solution. The breakthrough curves were compared by plotting the protein concentration profile in the permeate against the total permeate flow expressed as the dimensionless relative mass throughput (RMT) [Hiester and Vermeulen, 1952; Suen and Etzel, 1992; Charcosset et al., 1995; Han et al., 2005]. The RMT was calculated as:

$$RMT = \frac{(C_0 + K_d)Ft}{Q_\infty V_m} \tag{20}$$

Where C_0 is the protein concentration in the feed, K_d and Q_∞ were from the static Langmuir isotherm calculation, F is the flow rate of the permeate in ml/min, *t* is the time in min, and V_m is the volume of the membrane. The flow rates evaluated for the 100 cm^2 module were selected based on scaling up the flow rates for the 5 cm^2 membrane holder using the performance parameter. The performance parameter for each case was calculated using the first Damkholer number neglecting the ε and k_l terms in the numerator [Charcosset et al., 1995]:

$$\text{Performance Parameter} \cong \frac{Q_\infty V_m}{F} \tag{21}$$

The calculated performance parameters are included in Table 2.4 for each flow rate / membrane area combination. The system time lag was removed from the 4.0 and 10 ml/min 100 cm^2 membrane module breakthrough curves using the same method as the 0.2 and 0.5 ml/min 5 cm^2 membrane holder. The plug flow region and continuous stirred tank region were determined from the inverted washing curve for each flow rate and removed from the breakthrough curve. The plug flow region for the 4 and 10 ml/min flow rates was 13 ml. The continuous stirred tank region for the 4 ml/min flow rate was 26 ml. The continuous stirred tank region for the 10 ml/min flow rate was 24 ml. The fitted values for K_d and Q_∞ from the static isotherm were used for all RMT calculations.

The break though curves for all four flow rates are plotted in Figure 2.8. All four cases were similar when plotted on a dimensionless basis with the time lag removed (8A). The

	5 cm^2 module		100 cm^2 module	
	0.2 ml/min	**0.5 ml/min**	**4 ml/min**	**10 ml/min**
Performance Parameter	19.1 mg·min/ml	7.6 mg·min/ml	19.1 mg·min/ml	7.6 mg·min/ml
Q, Uncorrected	32.7 mg/ml	35.6 mg/ml	24.3 mg/ml	24.6 mg/ml
Q, Corrected	23.9 mg/ml	23.2 mg/ml	20.8 mg/ml	21.3 mg/ml

Table 2.4: Performance parameters used for flow rate scale-up and calculated membrane capacity. All runs used a feed BSA concentration of 250 μg/ml.

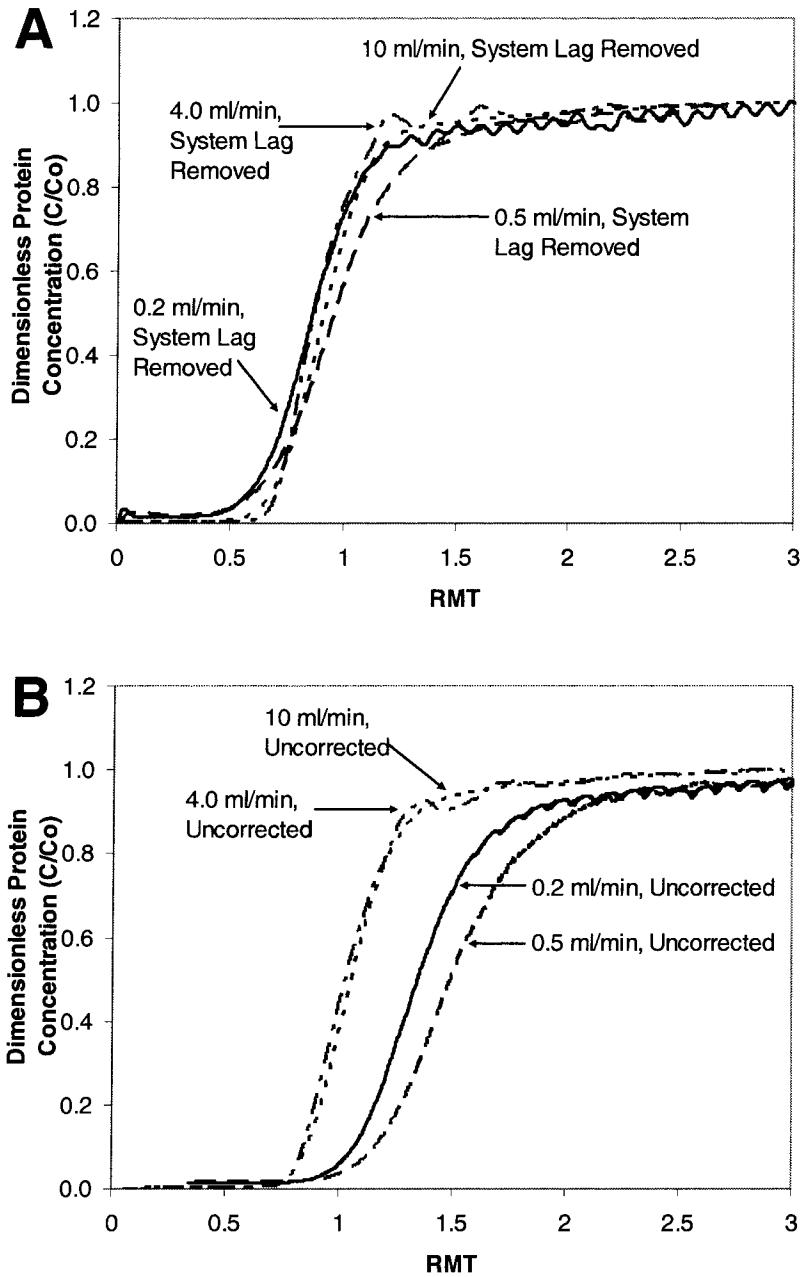

Figure 2.8: Dimensionless protein concentration plotted against the Relative Mass Throughput (RMT) with the system lag removed (A) and uncorrected (B). The 0.2 and 0.5 ml/min data was collected using the 5 cm^2 membrane holder and the 4.0 and 10 ml/min data was collected with the 100 cm^2 membrane module. Removing the system time lag resulted in accurate scale-up of the membrane chromatography system.

curves were not similar in the uncorrected curves (8B). The system time lag had a larger impact on the smaller 5 cm^2 membrane holder than on the larger prefabricated 100 cm^2 membrane module. Likewise, the membrane capacity was calculated for each flow rate with and without the system lag removed (Table 2.4). The membrane capacity was more similar with the time lag removed than without the time lag removed.

2.5 Conclusions

Membrane chromatography systems frequently contain significant time lags that are attributable to the tubing, membrane holder, and peripheral equipment. In many cases, these time lags can be removed from the breakthrough curves using a combination of simple model elements and numerical methods. As shown by the Langmuir-type isotherm calculations, the system time lag can have a large impact on the final results of the data analysis. Removing the system time lag also allowed for accurate scale-up from a 5 cm^2 membrane holder to a 100 cm^2 membrane module.

The primary advantage of the method outlined in this work is that the nature of the shape of the breakthrough curve does not need to be known, only the shape of the curve generated by the system lag. Application of this method to existing and new chromatography systems can yield improved insight to the binding mechanism and flow characteristics of the protein/membrane interaction through better understanding of the actual shape of the breakthrough curve without the influence of the system time delays.

Chapter 3

PORE SIZE DISTRIBUTION OF ULTRAFILTRATION MEMBRANES: MEASUREMENT, MODELING, AND APPLICATION

3.1 Abstract

The pore size distribution for a 500 kDa molecular weight cut-off cellulose acetate ultrafiltration membrane was determined by field emission scanning electron microscopy (SEM). Two log-normal distributions were fit to the discrete pore size distribution data. One was fit to the pore radius data and the second was fit to the normalized flow. All three distributions were used to calculate membrane flux and Dextran rejection profiles and compared to experimental results. Improvements in flux predictions for the log-normal distributions were made when modeling the pore size distribution based on normalized flow instead of the pore radii. The flux and rejection calculations were is strong agreement with the experimental results.

3.2 Introduction

Ultrafiltration is a basic unit operation used in many industries as a method to separate solutes in a solution based on molecular size. Ultrafiltration uses a porous membrane as a barrier for solutes larger than the pores. Solutes small enough to pass through the pores are transported through the membrane in the permeate stream. Solutes near the size of the pores are partially transported through the membrane. The rejection of a given size of

solute is defined as one minus the fraction of the solute that permeates the membrane. The cut-off for an ultrafiltration membrane is the size of the smallest solute that is fully rejected. The largest ultrafiltration membranes typically have a cut-off of approximately 30 nm radius solutes (corresponding to 500 kDa MW proteins). The two performance characteristics critical for commercial applications of ultrafiltration membranes are the flux and the solute rejection profile.

Ultrafiltration membranes have two distinct forms of construction: symmetric and asymmetric. Symmetric membranes have one uniform material of construction through the full thickness of the membrane. Both structural (mechanical strength) and functional (solute separation) properties are provided by this material. Asymmetric membranes consist of a thin functional membrane graphed to a thicker structural membrane. The thin functional component of the membrane contains the small radius ultrafiltration pores and typically has low mechanical strength. The thicker structural component of the membrane typically has pores an order of magnitude or larger than the functional component of the membrane (Calvo et al., 1997). The pore size distribution and membrane thickness of the functional component of asymmetric membranes has little effect of the overall membrane rejection or flux and is neglected for the calculations in this work. The flux and rejection performance of the two types of membranes are determined by pore size distributions at different points in the membrane. The surface pore size distribution determines the flux and rejection for asymmetric membranes (Calvo et al., 1997; Gumi et al., 2003). The bulk pore size distribution (the distribution

within the thickness of the membrane) determines the flux and rejection performance characteristics of symmetric membranes (Prádanos et al., 1996; Hernandez et al, 1998).

The transport of a solute molecule through a pore in an otherwise non-permeable membrane occurs by a combination of two means, diffusion and convection. Diffusion is the property of solutes in a solvent to move randomly within the solvent. The random nature of the solute movement tends to equilibrate the solute concentration throughout the solvent over time. In general, the permeate side of an ultrafiltration membrane has a lower solute concentration than the retentate side. This concentration gradient across the membrane provides a driving force for diffusion of the solute through the membrane. Through random motion, the solutes enter the membrane pores and eventually some of the solutes migrate to the permeate side of the membrane. Given enough time under static conditions with a membrane with large enough pores to physically allow the solute to pass through, the concentration of the solute will be equal on the permeate and retentate sides of the membrane. Convection occurs when the there is bulk solvent flow from the retentate to the permeate side of the membrane. The moving solvent will tend to carry solutes through the pores. When the hydraulic radius of the solutes is the same order of magnitude as the radius of the pores, the movement of the solute through the pores becomes hindered. Models describing the movement of solutes through pores under hindered conditions are discussed in detail in reviews by Deen (1987) and Nakao (1994). Briefly, the rate of transport by diffusion and convection can be calculated. The relative magnitude of the diffusion rate to the convection rate is described by the Peclet number (Pe). For small Peclet numbers ($<<1$), diffusion dominates. For large Peclet

numbers (>>1), convection dominates the transport of the solute from the retentate to the permeate side of the membrane. Under hindered conditions, the size of the solute relative to the size of the pore affects diffusion and convection to different extents. Correction coefficients for the diffusion and convection rates can be calculated by assuming the solute is spherical, the pore is cylindrical, and the solvent is significantly smaller than both. Asymptotic expansions are performed on a dimensionless basis and the resulting approximations are used to relate the rate of transport under hindered conditions to un-hindered conditions (Bungay and Brenner, 1973). In this work, the Peclet numbers are large and the transport of solutes across the membrane by diffusion is negligible.

As the ratio of the solute radius to the pore radius approaches 1 the diffusion and convection transport rates dramatically decrease. This reduction in transport rate is a method to physically separate larger molecules from smaller molecules and is termed "sieving" or "rejection".

In most types of membranes, the membrane does not contain just one size of pore. A pore size distribution describes the relative frequency of each size of pore per unit cross-sectional area of the membrane. Small pores in the distribution will block most of the solutes in the solution but the presence of even a few large pores completely through the membrane will allow an appreciable amount of larger-sized solutes to permeate the membrane and defeat the filtration.

Many methods have been developed to measure pore size distributions (Nakao, 1994; Baltus, 1997a; Baltus, 1997b; Gadam et al., 1997; Germic et al., 1997; Khulbe and Matsuura, 2000; Zhao et al., 2000; Ramaswamy et al., 2004). Direct methods measure the characteristics of the surface pores. Scanning electron microscopy (SEM) and atomic force microscopy (ATM) are the two most widely used direct methods for measuring the pore size distribution of ultrafiltration membranes (Dietz et al., 1992; Pradanos et al., 1996; Calvo et al., 1997; Germic et al., 1997; Hernandez et al., 1998; Khulbe and Masuura, 2000; Khayet and Matsuura, 2003; Gumi et al., 2003; Khayet et al., 2004; Ramaswamy, 2004). Indirect methods measure a secondary effect of the membrane such as solute rejection profiles, bubble sizes, liquid displacement, Raman spectrum, electronic spin resonance, ultrasonic frequency domain reflectometry, or gas adsorption/desorption and then calculate the pore size distribution based on theory and/or assumptions about the nature of the pore size distribution (Pradanos et al., 1996; Baltus, 1997a; Baltus, 1997b; Calvo et al., 1997; Gadam et al., 1997; Germic et al., 1997; Hernandez et al., 1998; Khulbe and Masuura, 2000; Lee et al., 2002; Khayet and Matsuura, 2003; Gumi et al., 2003; Khayet et al., 2004; Ramaswamy, 2004; Baltus, 2006). The indirect method used to calculate the nominal pore size distribution influences the distribution parameters with different indirect methods resulting in different parameters. Frequently, both direct and indirect methods are used to determine pore size distributions and other pertinent membrane characteristics such as membrane surface area, roughness, and void fraction.

Direct pore size measurements result in a discrete pore size distribution populated by the observed surface pores which then must be assumed to remain similar throughout the

bulk of the membrane. Indirect pore size measurements require a nominal pore size distribution model to be selected and used in the subsequent calculations to fit the experimental data. The selection of the pore size distribution model can have a significant impact of the quality of the fit results (Mochizuki and Zydney, 1993; Berjani-Bayeh and Rodgers, 2002). The log-normal distribution is widely used for pore size distributions of ultrafiltration membranes.

In this work, twenty SEM images were collected for an asymetric cellulose acetate ultrafiltration membrane. The pores in the images were measured and a discrete pore size distribution was generated. The discrete distribution was fit to a log-normal distribution based on either the pore radius or the normalized flow through the pore using the Hagen-Poiseuille equation. Water flux and Dextran rejection profiles were calculated for the discrete, log-normal fit using the pore radii, and log-normal fit using the normalized flow rates. The calculations for the three distributions were compared to experimental results.

3.3 Materials and Methods

3.3.1 Materials

Regenerated cellulose ultra filtration membranes with a nominal 500 kDa molecular weight cut-off were obtained from Millipore (Bedford, MA). The membranes were imaged using a JEOL JSM-6500F Field emission scanning electron microscope (Peabody, MA) at 15,000 kEv. The membranes were sputtered with a 5 nm gold layer using a Hummer VII sputtering system (Anatech Ltd., Alexandria, VA). Cross-sections

were obtained by freezing the membrane in liquid nitrogen for a minimum of one minute, removing the membrane from the liquid nitrogen, and sharply cracking the membrane.

Mono-dispersed Dextran standards were purchased to prepare both the calibration and feed Dextran solutions. Dextran T1 (MW 1 kDa) was purchased from Pharmacosmos (Holbæk, Denmark). Dextran T4 (MW 4 kDa) was purchased from Serva (Frankfurt, Germany). Dextran T10 (MW 10 kDa), 40 (MW 40 kDa), T70 (MW 70 kDa), T500 (MW 500 kDa), and T2000 (MW 2000 kDa) were purchased from GE-Healthcare Bio-Sciences Corp. (Piscataway, NJ). The calibration and feed solutions were prepared at the same Dextran concentrations for each component in the single and multi-component solutions. The Dextran concentrations were 0.74 g/l (T1), 1.22 g/l (T4), 0.54 g/l (T10), 0.74 g/l (T40), 0.34 g/l (T70), 0.27 g/l (T500), and 3.65 g/l (T2000).

3.3.2 Experimental Procedures

Membrane flux was measured using double DI water and a Millipore (Billerica, MA) model 8050 stirred ultrafiltration cell with a membrane diameter of 44.5 mm. Nitrogen was used to pressurize the head on the feed side of the ultrafiltration cell. Flux measurements were obtained at 10, 20, 30, 40 and 50 psi pressure drop across the membrane by collecting permeate in tared flasks for five minutes. The experimental rejection data was measured using the same ultrafiltration cell. A peristaltic pump was used to pull permeate through the membrane at a total flow rate of 0.1 ml/min. Forty five ml of feed solution was loaded into the feed chamber and the system was operated under full permeate recycle for one hour to equilibrate the membrane. After equilibration, 1 ml

of permeate was collected and analyzed to determine the concentration of each Dextran component.

Dextran concentrations were determined by high performance liquid chromatography (HPLC). An Agilent Technologies Model 1050 (Palo Alto, CA) HPLC was used with a SB-806M HQ gel permeation column and a Showa Denko SB-G guard column (Tokyo, Japan) to separate Dextran components in the feed and permeate samples. An Agilent Technologies 1047A refractive index (RI) detector (Palo Alto, CA) was used to detect the Dextran concentrations on the discharge of the gel permeation column. The HPLC mobile phase was 0.05 mol/L KH_2PO_4/NaOH buffer at pH 7 at a flow rate of 0.4 ml/min. Temperature was controlled at 40°C. HPLC grade NaOH and reagent grade KH_2PO_4 were purchased from Sigma-Aldrich (St. Louis, MO).

3.3.3 Calculations

3.3.3.1 Hagen-Poiseuille Approximation

The Hagen-Poiseuille equation relates the radially-averaged solution velocity through a cylindrical pore to the pressure drop across the length of the pore. The equation was originally derived to model the flow of blood in the circulatory system. The Hagen-Poiseuille approximation models a porous membrane as a collection of cylindrical tubes of various radii in parallel. The approximation is one of the simplest flow-through-pore models and does not account for the effect of solute interactions or membrane fouling on the solute velocity. The equation has the following form [Mochizuki and Zydney, 1993; Nakao, 1994]:

$$v = \frac{r^2 \Delta P}{8\eta L} \tag{3.1}$$

Where v is the radially averaged solution velocity (m/s), r is the pore radius (m), ΔP is the pressure drop across the cylindrical pore (pa), η is the solvent viscosity (pa·s), and L is the membrane thickness (m).

3.3.3.2 Log Normal Distribution

The log normal distribution is frequently used to describe the pore size distribution for ultra filtration and micro filtration membranes (Zydney et al., 1994). The log normal distribution has several different, but equivalent, forms (Zydney et al., 1994). The log normal distribution form used to fit the discrete data is:

$$n(r) = n_0 \exp\left(-\frac{[\ln(r) - \ln(R_m)]^2}{(\ln \sigma_1)^2} \right) \tag{3.2}$$

Where n(r) is defined as the product of the probability distribution function (PDF) and the total number of pores per unit membrane, N_0. The most probable pore radius is R_m and σ_1 is related to the geometric standard deviation (see Equation 3.5). The parameter n_0 is used to normalize the probability density function. The normally-distributed mean, most probable, and variance of the distribution can be calculated as (Zydney et al., 1994):

$$Mean(\mu) = R_m \exp\left[\frac{3}{4} (\ln \sigma_1)^2 \right] \tag{3.3}$$

$$Most\ Probable = R_m \tag{3.4}$$

$$Variance(\sigma'^2) = (R_m)^2 \left(\exp[2(\ln \sigma_1)^2] - \exp\left[\frac{3}{2} (\ln \sigma_1)^2 \right] \right) \tag{3.5}$$

3.3.3.3 Flux

The total flow per unit area through the discrete pore size radius distribution is calculated as a sum of the flow rates through the individual pore radius categories assuming an equivalent pressure drop through each pore regardless of its position on the surface of the membrane:

$$j = \frac{3{,}600{,}000\pi\Delta P}{8\eta L}\sum_{i=1}^{n} n(r_i)r_i^4\Delta r \qquad (3.6)$$

Where j is the flux ($l/m^2/hr$), ΔP is the pressure drop across the membrane (pa), η is the solvent viscosity (pa·s), L is the membrane thickness (m), $n(r_i)$ is the number of pores of a given radius per unit area, r_i is the pore radius (m), and Δr is the bin width (m).

The flux through the continuous pore size radius distribution is calculated as the integral of the flow rate through the individual pores assuming the same pressure drop through each pore regardless of its position on the surface of the membrane as in Equation 3.6:

$$j = \frac{3{,}600{,}000\pi\Delta P}{8\eta L}\int_0^{\infty} n(r)r^4 dr \qquad (3.7)$$

3.3.3.4 Rejection Coefficients

The rejection (reflection) coefficient relates the concentration of solute transported through a pore relative to the bulk concentration and is calculated by estimating the hindered transport of the solute through a closely fitting fluid filled pore (Deen, 1987).

The rejection coefficient is defined as equal to 1.0 when no solute is transported through the pores and equal to 0.0 when the concentration of the solute in the permeate is equal to the solute concentration in the bulk solution. The Dextran molecules are approximated as spheres and the pores are approximated as cylinders of a fixed given radius. For high Peclet number flows (Pe >>1), the rejection coefficient simplifies to 1 minus the convective hindrance constant, W, since diffusion terms are neglected (Deen, 1987). The rejection coefficient (R_k) for each species k is defined as:

$$R_k = 1 - W_k \tag{3.8}$$

The Peclet number is the ratio of the diffusional rate of the solute to the convection rate of the solute. Equation 3.9 was used to estimate the Peclet number for the close-fitting dextran molecule moving through a cylindrical pore (Bungay and Brenner, 1973). Concentration polarization can affect the separation factor and the Peclet number (Bhattacharya and Hwang, 1997). The ultrafiltration cell is assumed to be well mixed and the concentration polarization is assumed negligible in these calculations.

$$Pe = \frac{WvL}{HD_{\infty}} \tag{3.9}$$

Where W is the convective hindrance coefficient and H is the diffusion hindrance coefficient. L is the membrane thickness (m) and v is the radially averaged velocity (m/s). The bulk diffusion rate, D_{∞}, is approximated. The convective and diffusion hindrance coefficients are calculated based on the theoretical models presented in Bungay and Brenner, 1973:

$$W = \frac{\Phi(2-\Phi)K_S}{2K_T} \tag{3.10}$$

$$H = \frac{6\pi\Phi}{K_T} \tag{3.11}$$

$$\Phi = (1-\lambda)^2 \tag{3.12}$$

$$\lambda = \frac{r_h}{r_p} \tag{3.13}$$

$$\begin{pmatrix} K_S \\ K_T \end{pmatrix} = \frac{9}{4}\pi^2\sqrt{2}(1-\lambda)^{-5/2}\left[1+\sum_{n=1}^{2}\begin{pmatrix} a_n \\ b_n \end{pmatrix}(1-\lambda)^n\right]+\sum_{n=0}^{4}\begin{pmatrix} a_{n+3} \\ b_{n+3} \end{pmatrix}\lambda^n \tag{3.14}$$

The coefficients used in Equation 3.14 are defined as: a_1 = -73/60; a_2 = 77,293/50,400; a_3 = -22.5083; a_4 = -5.6117; a_5 = -0.3363; a_6 = -1.216; a_7 = 1.647; b_1 = 7/60; b_2 = -2,227/50,400; b_3 = -4.0180; b_4 = -3.9788; b_5 = -1.9215; b_6 = 4.392; b_7 = 5.006. The hydraulic radius, r_h, for each Dextran size was obtained from literature (Armstrong et al., 2004). The range of pore radii, r_p, considered was determined from the SEM image analysis.

3.4 Results and Discussion

Scanning electron micrograph (SEM) images were collected of both the closed and open sides of the cellulose membrane (Figure 3.1). As expected, the pore morphology is significantly different between the functional (closed) and structural (open) sides. Surface pores on the open side of the membrane are approximately 50 times the size of the surface pores on the closed side of the membrane. Image analysis of the cross-section

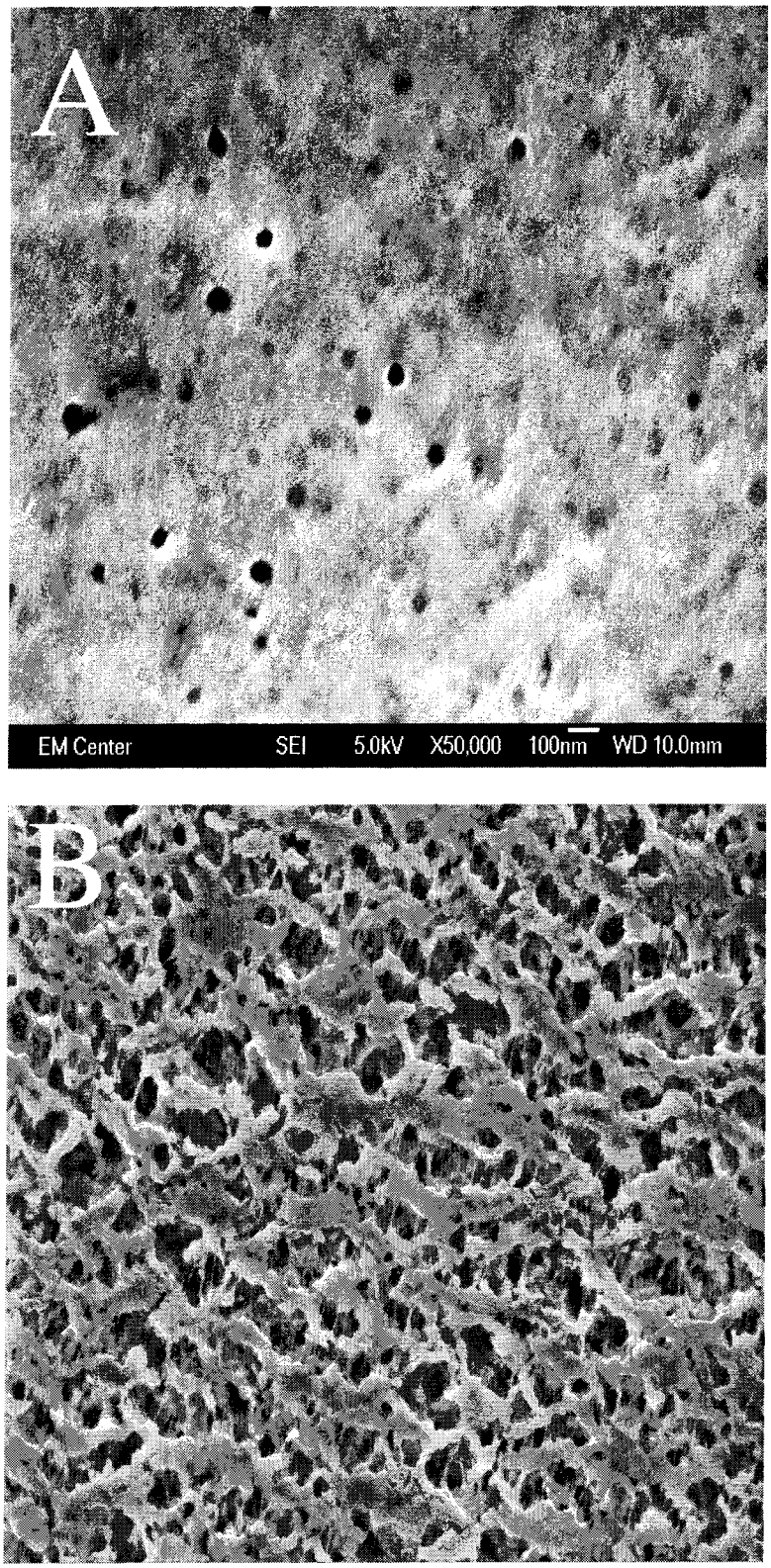

Figure 3.1: SEM image of the (A) closed and (B) open sides of the membrane. The closed side is shown at x50,000 magnification. The open side is shown at x1000 magnification.

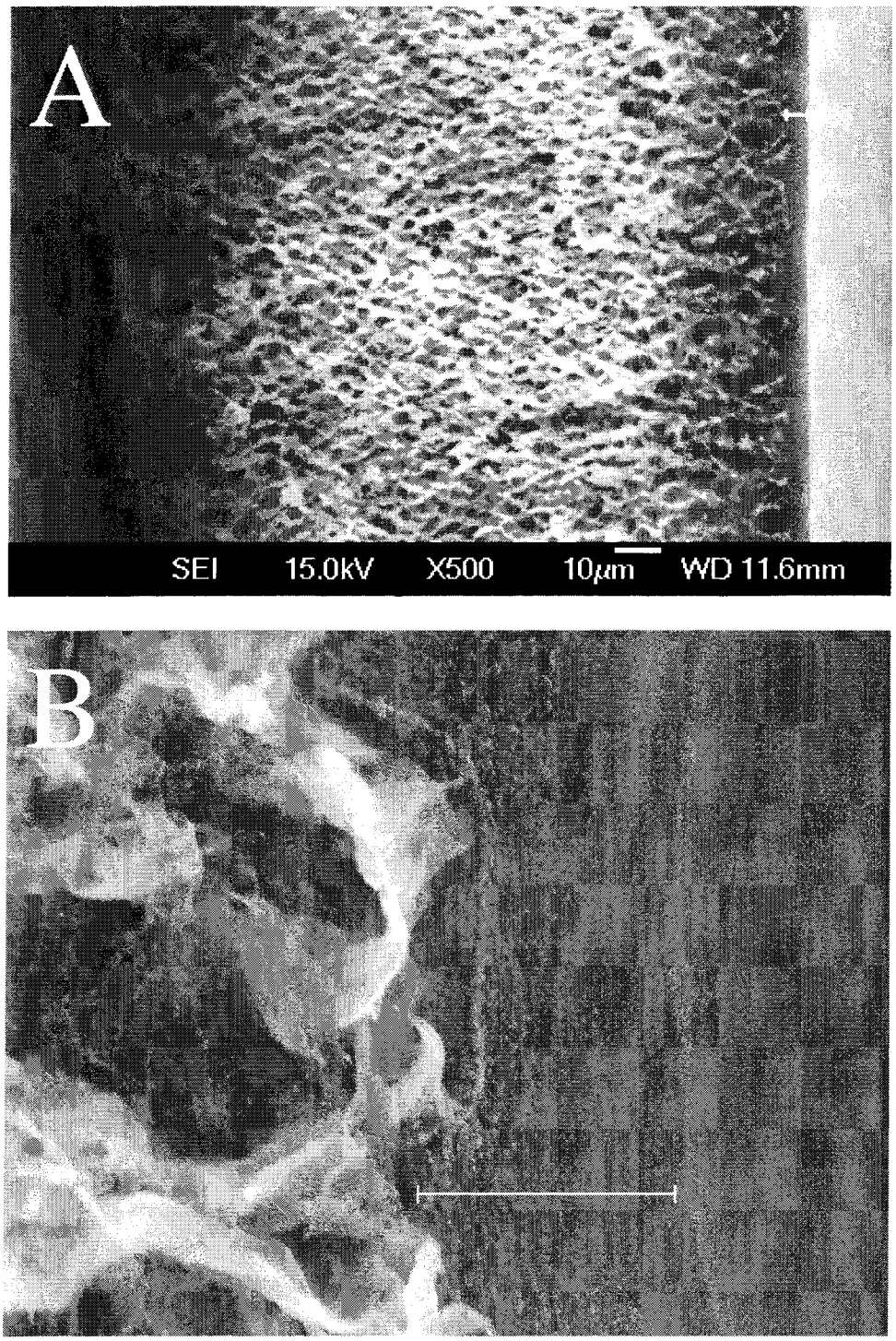

Figure 3.2: SEM of edge of unmodified cellulose acetate membrane at (A) x500 and (B) x10,000 magnification. The white bar indicates the ultra filtration layer on the regenerated cellulose structural matrix and is 3.5 μm in depth. The ultra filtration layer is used to calculate the flux through the membrane.

of the membrane was used to determine the thickness of the functional ultra-filtration layer on the closed side of the membrane (Figure 3.2). The ultra-filtration layer thickness is consistently 3.5 μm. Flux calculations were made assuming that the surface morphology and pore size distributions were indicative of constant radius cylinders of a length equivalent to the membrane thickness.

Twenty images of the closed side of the membrane were analyzed to generate the discrete pore size distribution. The circumferences of the pores in the image were defined through image analysis functions in MATLAB and a black and white image was constructed defining the pores in each image (Figure 3.3). The equivalent diameter of a circle with an equal cross-sectional area was calculated for each pore in the image. A data set containing the equivalent diameters for all of the pores in the images was used to construct four different histograms with bin sizes of 1, 2, 5, and 10 nm respectively. The histograms and the total number of pores were used to determine the discrete probability distribution function (PDF) shown in Figure 3.4. The 5 nm bins size was selected for the fitting of continuous distribution functions and as the discrete distribution function for further calculations. The bin selection was determined from membrane flux calculations for the different distributions (data not shown). The membrane flux calculated for the 1, 2 and 5 nm bin distributions were within 1% of each other. The membrane flux calculated for the 10 nm bin distribution was significantly different than the other flux calculations. The largest bin size that did not introduce significant error was selected for further modeling and curve fitting. The 5 nm bin distribution had the additional advantage of minimizing much of the noise apparent in the 1 and 2 nm bin distributions.

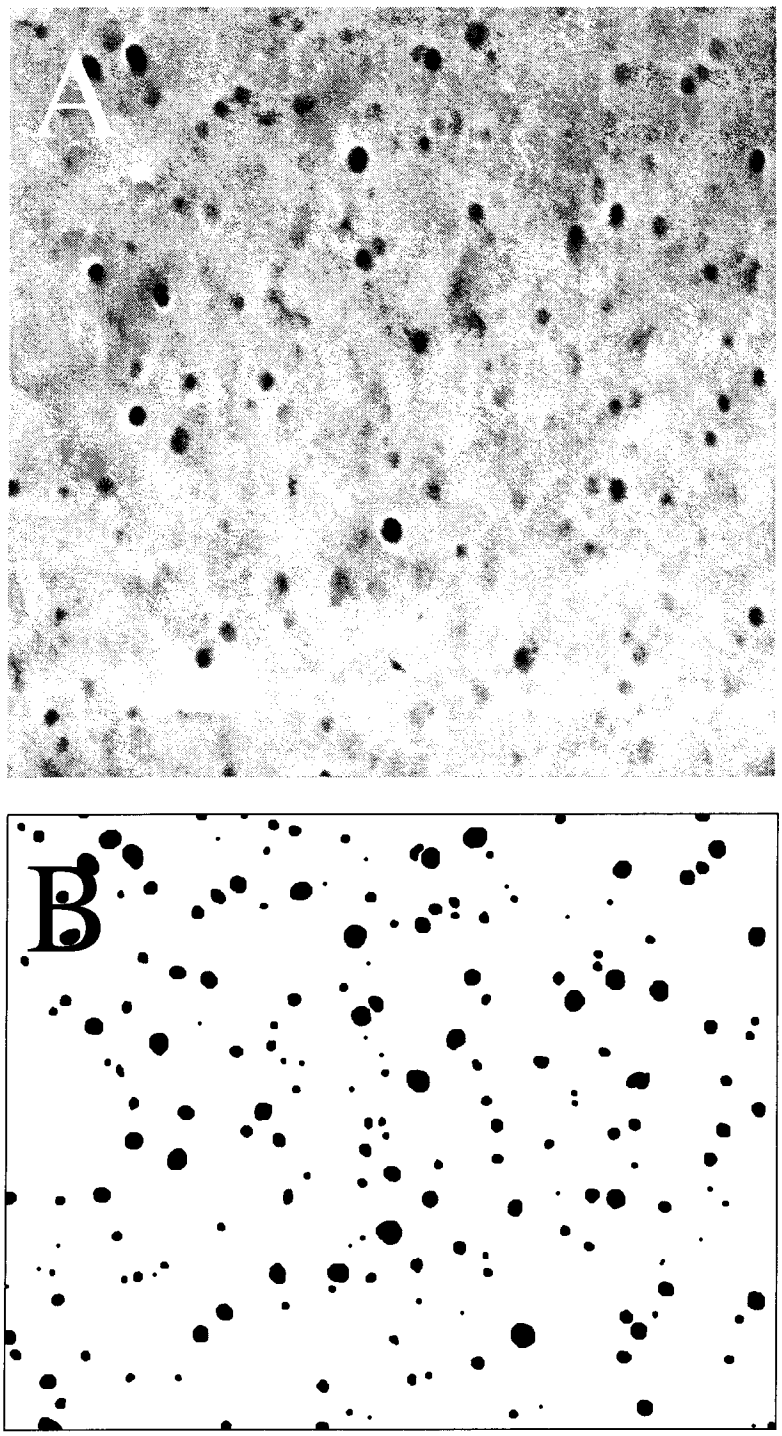

Figure 3.3: Example of image analysis of a typical SEM. A) The image taken during the SEM at x50,000 magnification. B) The digital image was analyzed using a custom MATLAB program and converted to a black and white image to generate the pore size distribution. At total of 20 images were analyzed to construct the pore size distribution.

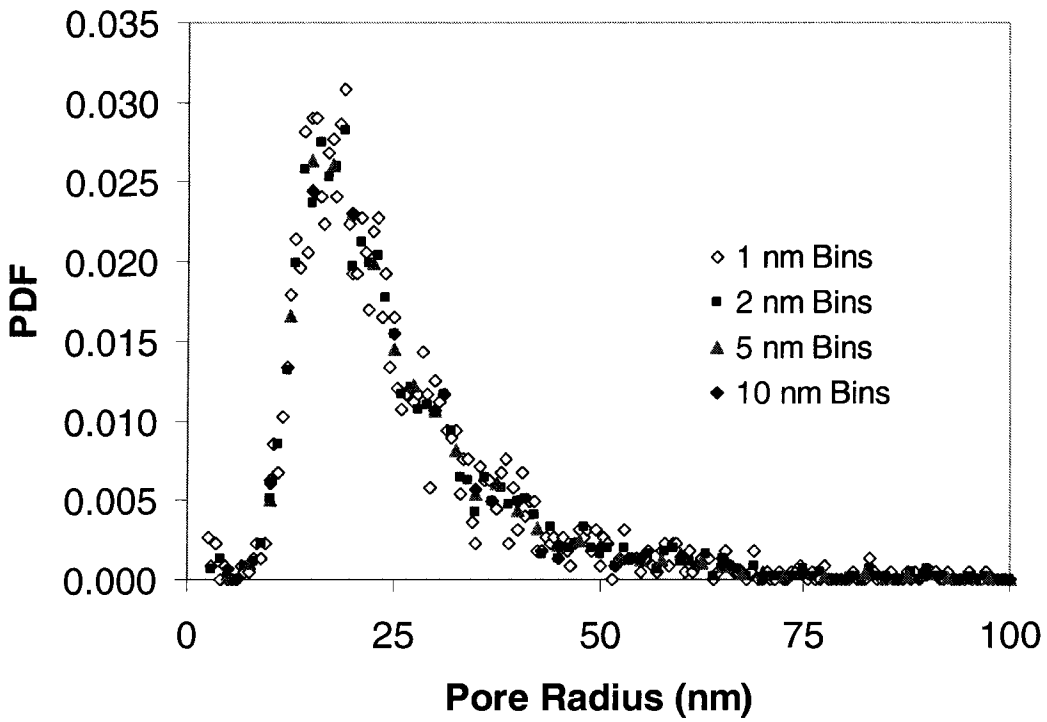

Figure 3.4: Discrete pore size distribution generated from SEM images. The distribution was generated from a histogram of the calculated equivalent radii of the pores. Four different histogram bin sizes were evaluated.

The number average pore radius was determined for the 5 nm distribution as 25.6 nm with a Gaussian (normal) standard deviation (σ') of 12.9 nm and a variance (σ'^2) of 166.4 nm^2. The discrete pore size distribution was truncated at $\pm 3\sigma$. Three standard deviations include 99% of the pores in the distribution, and includes the pores that dominate the flow and sieving properties of the membrane. The 5 nm bin discrete distribution is shown in Figure 3.5. Two log normal distributions were fit to the discrete data. The first method was to fit the PDF to the pore radius discrete distribution. The second method involved calculating the normalized flow through the PDF using the Hagen-Poiseuille approximation and fitting r^4*PDF to the resulting flow data. The two methods enhance the curve fitting to different regions of the distribution. Fitting the PDF to the pore radius data enhances the curve fit to the most probable region of the distribution. Fitting r^4*PDF to the normalized flow calculation enhances the curve fit to the tail end of the distribution (pores with a radius greater than ~30 nm). All fits were determined by minimizing the sum of squares difference between the calculated and experimental data. The curve fitting methods are shown graphically in Figure 3.6 and the resulting parameters are tabulated in Table 3.1.

Flux calculations were performed for the discrete distribution (Equation 3.6) and the two log normal distributions (Equation 3.7) and compared to the experimental results in Figure 3.7. The discrete distribution and the log normal distribution fit from the normalized flow match the experimental results. The flux calculated from the log normal distribution fit from the pore radius data under estimates the membrane flux. The log normal distribution fit from the pore data under estimates the number of pores at larger

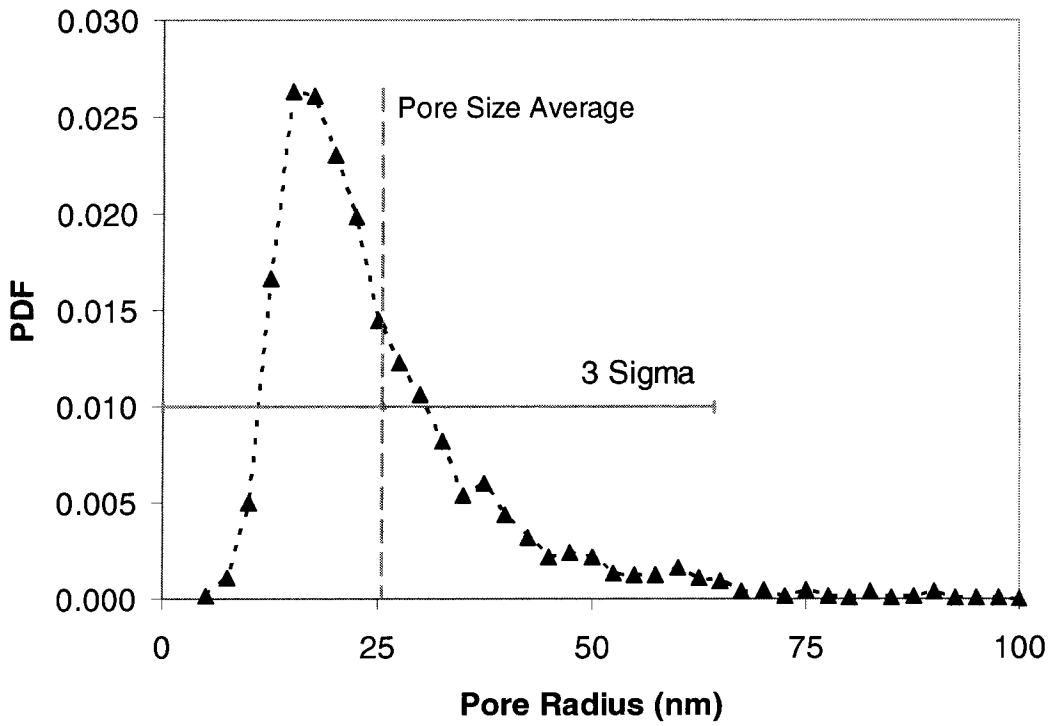

Figure 3.5: The average pore radius of the distribution is 25.6 nm. The standard deviation is 12.9 nm. The truncated distribution is 0 to 65 nm.

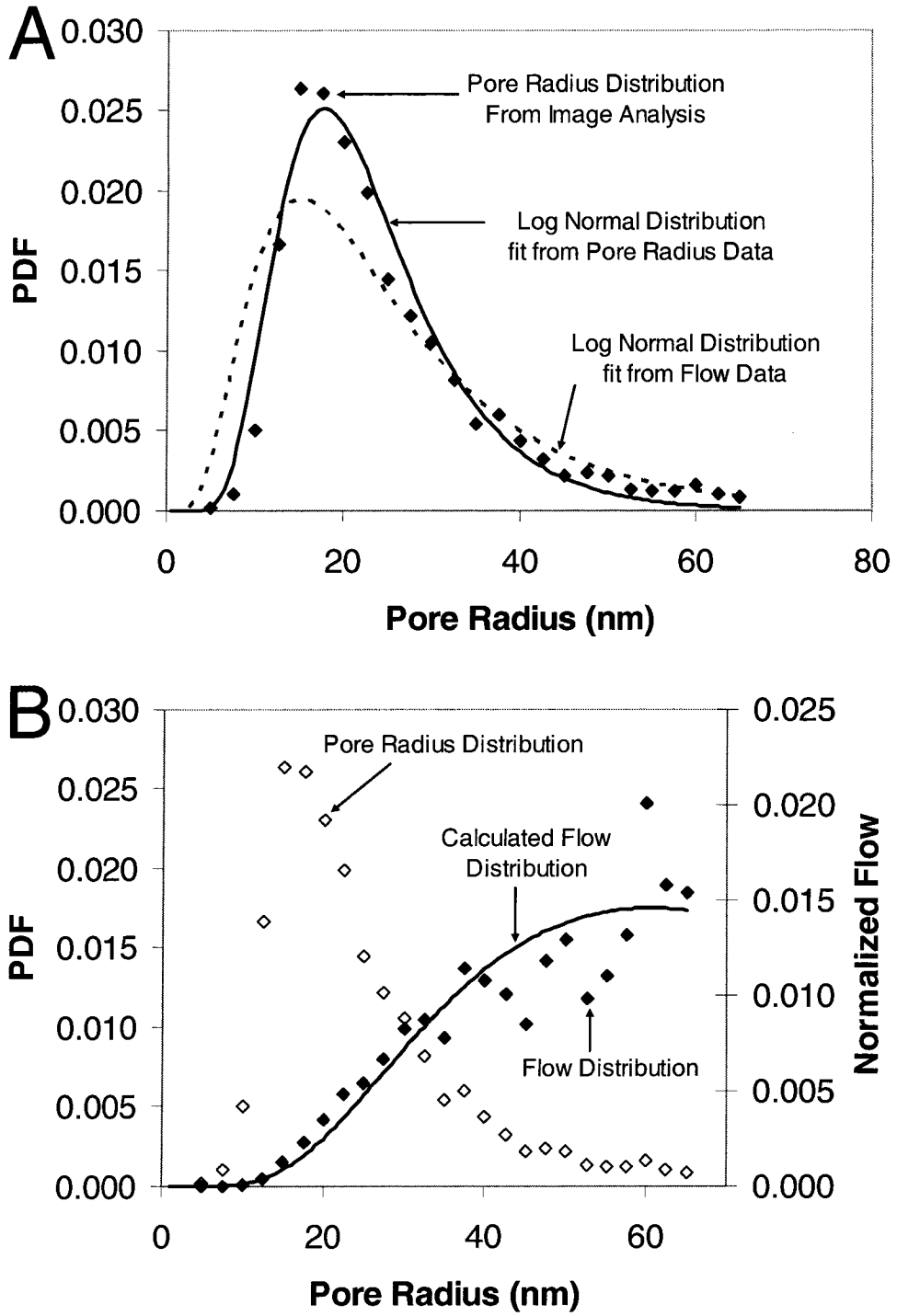

Figure 3.6: Log normal distribution fit to (A) pore radius distribution and (B) normalized flow distribution. The log normal fit to the normalized flow distribution is plotted in (A) for visual comparison of the differences between the log normal distributions fit by different methods.

Method to Fit	σ_1	R_m	Mean (μ)	Most Probable	Variance (σ'^2)
Discrete (5 nm bins)	n/a	n/a	25.6	16.1	166.4
Pore Size Distribution	1.8	17.7	22.9	17.7	99.2
Normalized Flow	2.3	15.1	25.4	15.1	267.6

Table 3.1: Parameters fit for the various probability density functions. The mean and variance are normally distributed and either calculated directly (Discrete PDF) or calculated per Zydney et al., 1994 (Pore size distribution and normalized flow).

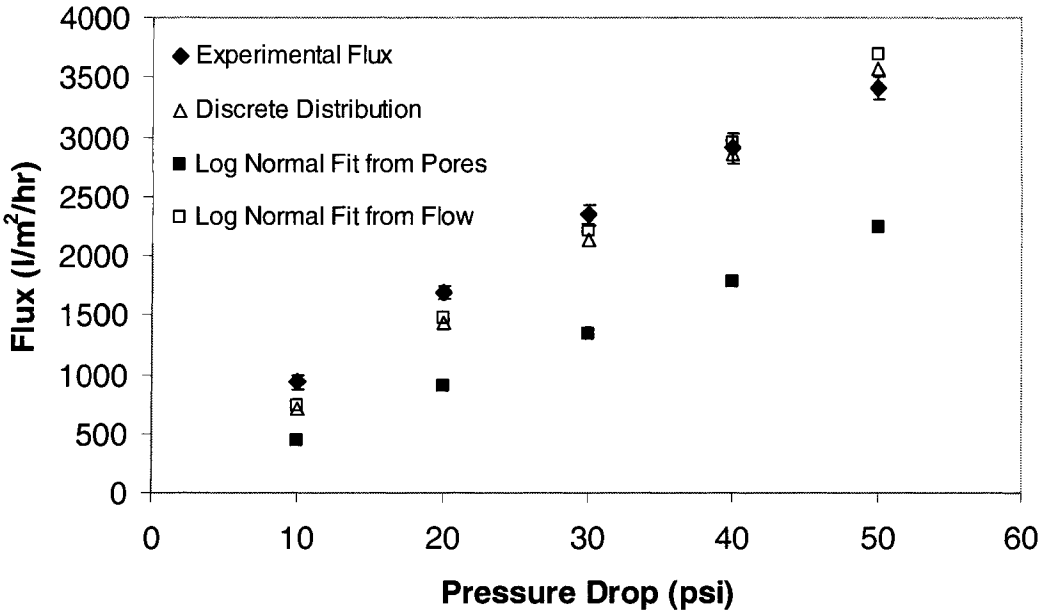

Figure 3.7: Calculated membrane flux for different pore size distributions and different pressure drops.

pore radii (Figure 3.6A). Volumetric flow through a cylindrical pore is proportional to the radius to the fourth power. The majority of the membrane flux is through a small number of pores at the upper end of the pore size distribution. This is clearly indicated in Figure 3.6B with the normalized calculated flow distribution data. Under estimation of the number of larger pore radii results in under predicting the flux, j.

The Peclet number can be calculated for each pore radius in the discrete distribution. The calculated Peclet numbers for the discrete distribution are shown in Figure 3.8. All of the Peclet numbers are much greater than 1. Convection dominates the transport of the Dextran molecules through the pores. Peclet numbers calculated for the two log-normal distributions are very similar to the discrete distribution (data not shown).

The rejection coefficient was calculated for the 5 largest solutes (T10, T40, T70, T500 and T2000) using Equations 3.8 through 3.14. As discussed previously, the rejection coefficient was estimated assuming the Dextran behaved as a spherical solute with a constant hydraulic radius and were transported through close fitting cylindrical pores under flow conditions where convection dominates. The rejection curves are plotted as a function of pore radius in Figure 3.9.

Experimental rejection data was collected from a seven component dextran solution. The individual dextran components were mono-dispersed. HPLC chromatograms of the individual dextran components collected singularly were used to calibrate the HPLC

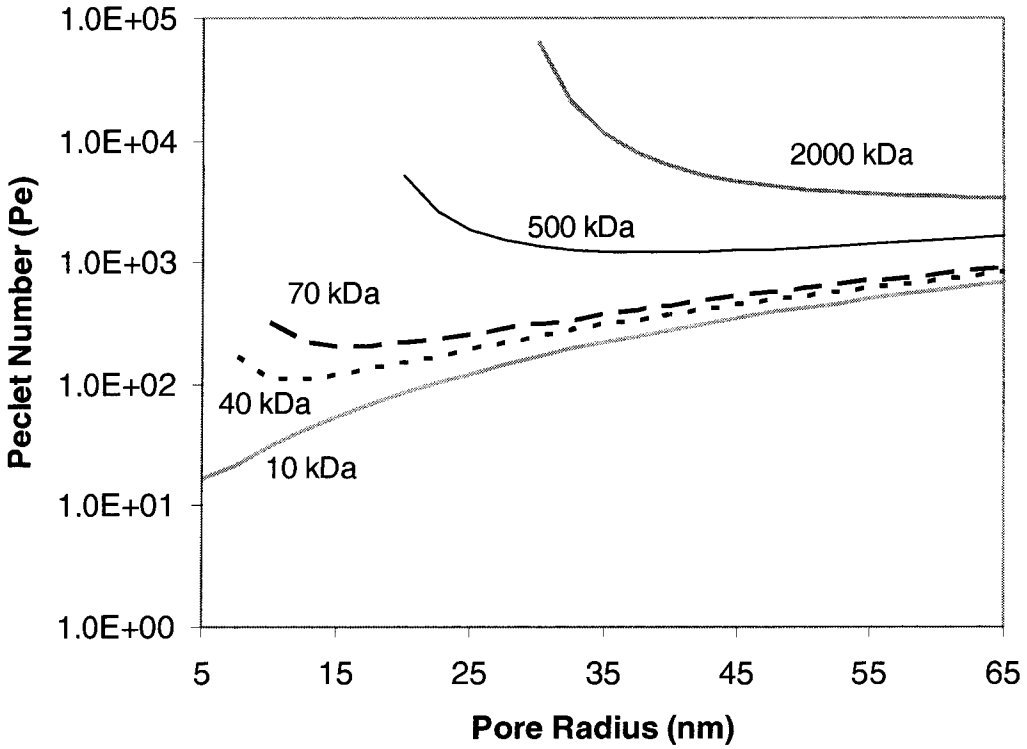

Figure 3.8: Peclet numbers calculated for the discrete pore size distribution at 10 psi pressure drop across the membrane. The Peclet numbers calculated for both log-normal distributions are similar.

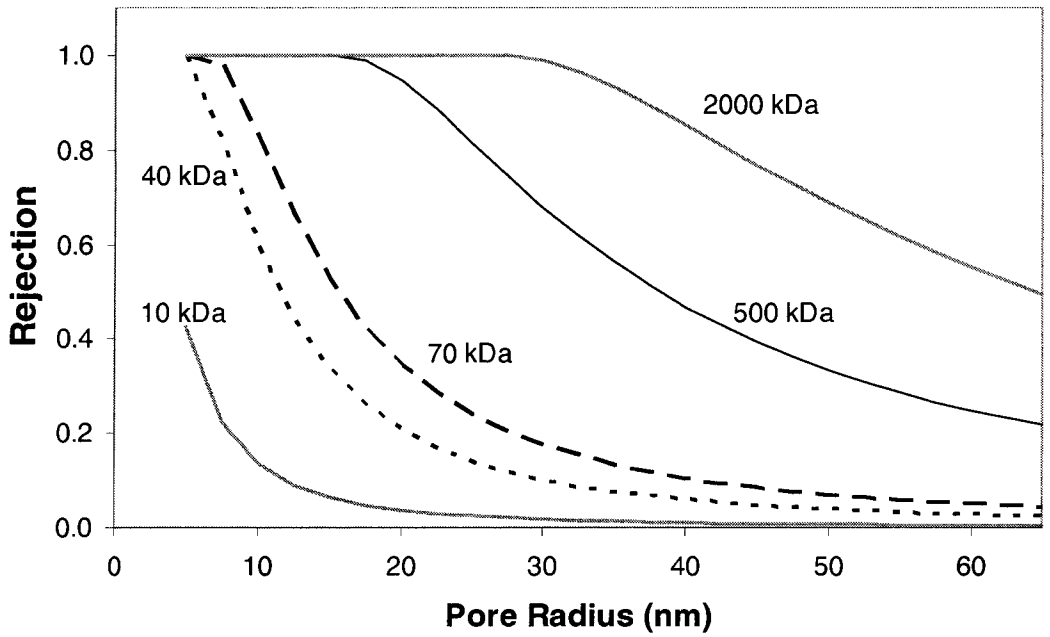

Figure 3.9: Rejection coefficients calculated for the different Dextran components.

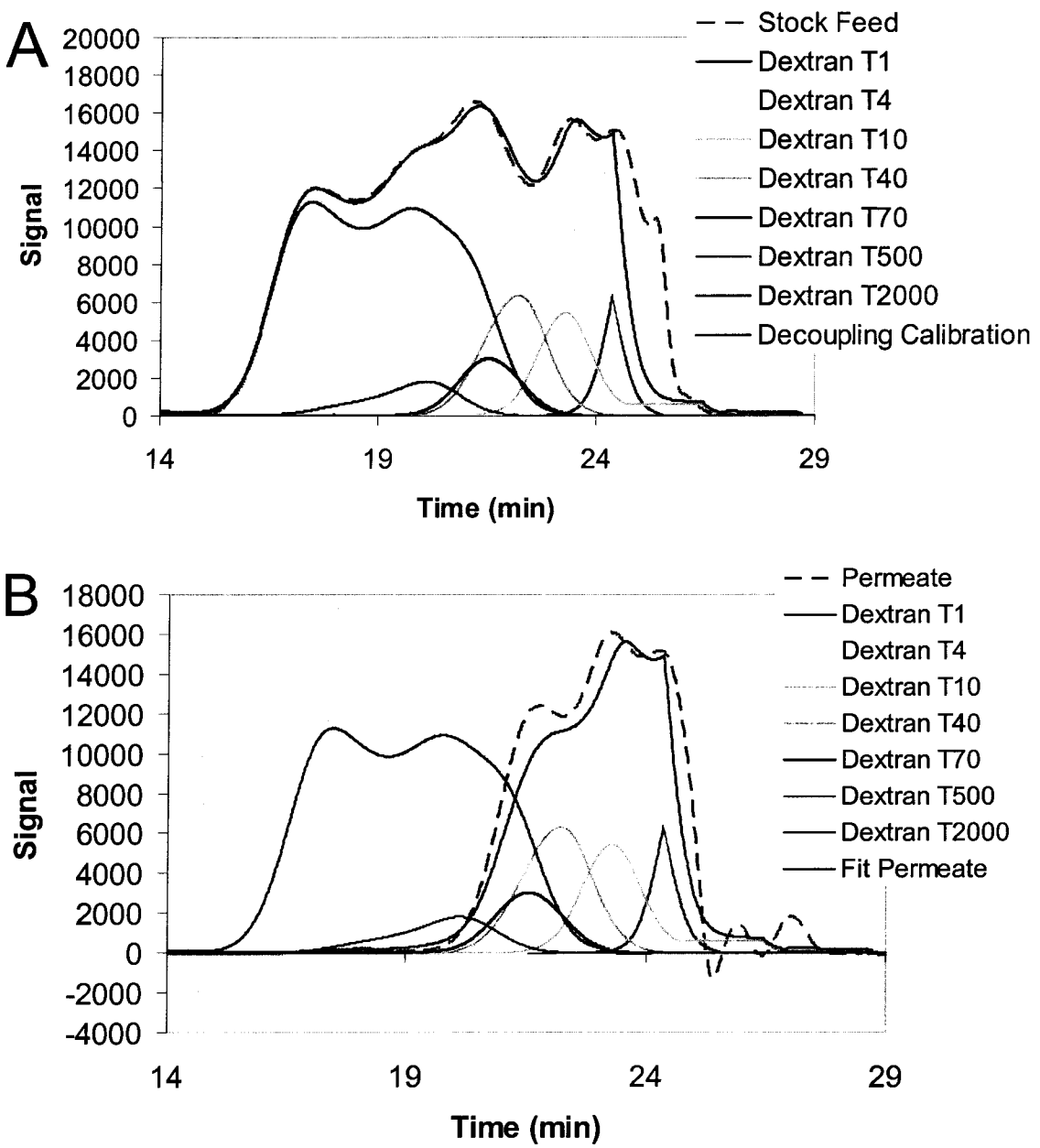

Figure 3.10: Calibration and permeate data used to calculate Dextran concentrations in the permeate. (A) Individual component HPLC curves were multiplied by calibration constants and summed as the decoupling calibration curve to fit the stock feed HPLC curve. (B) The permeate HPLC curve was fit by multiplying the individual component curves by the calibration constants, w_i, and the individual component concentration constants, c_i.

Component	MW (kDa)	Hydrodynamic Radius (nm)	Calibration Multiplier, w_i	Permeate Multiplier, c_i	C/C_0 in Permeate
T1	1	n/a	*1.20*	*1.00*	1.0
T4	4	n/a	*0.88*	*1.00*	1.0
T10	10	1.86	*1.10*	*1.00*	1.0
T40	40	4.78	*1.00*	*1.00*	1.0
T70	70	6.49	*1.60*	*1.00*	1.0
T500	500	15.9	*1.50*	*0.10*	0.1
T2000	2000	26.89	*1.02*	*0.01*	0.01

Table 3.2: Scaling multipliers for individual feed HPLC curve and the permeate HPLC curves. The permeate multiplier is the ratio of the concentration in the permeate to the concentration in the stock feed (i.e. a multiplier of 0.1 is equal to a permeate concentration of 10% of the concentration in the stock feed). There appears to be little rejection of the Dextran T70 or less. The T500 and T2000 are mostly rejected. Dextran radius data from Armstrong et al., 2004.

curve generated from the seven component mixed feed (Figure 3.10A) by fitting the component weighting parameters, w_i, using Equation 3.15. The membrane permeate was analyzed by fitting Equation 16 to the HPLC curve in Figure 3.10B. The rejection data and parameters are summarized in Table 3.2.

$$f_{feed}(t) = \sum_{i=1}^{7} w_i f_i(t) \tag{15}$$

$$f_{permeate}(t) = \sum_{i=1}^{7} c_i w_i f_i(t) \tag{16}$$

The overall rejection of solute through the membrane ($R_{k,Overall}$) was estimated by calculating the rejection for each component (subscript k) through each pore size of the distribution (subscript i) and weighing the sum by the normalized flow through the pore size (Equation 3.17).

$$R_{k,Overall} = \sum_{i=1}^{n} R_{k,i} \frac{\frac{3{,}600{,}000\pi\Delta P}{8\eta L} n(r_i) r_i^4 \Delta r}{j} \tag{17}$$

The results for each distribution are shown in Figure 3.11. All three distributions underestimate the experimental rejection. The log-normal distribution fit to the pore radius measurements does the best job of approximating the experimental data. The log-normal distribution fit from the pore radius measurements has the lowest average pore radius and smallest standard deviation and hence has the best calculated rejection of the larger sized Dextran molecules.

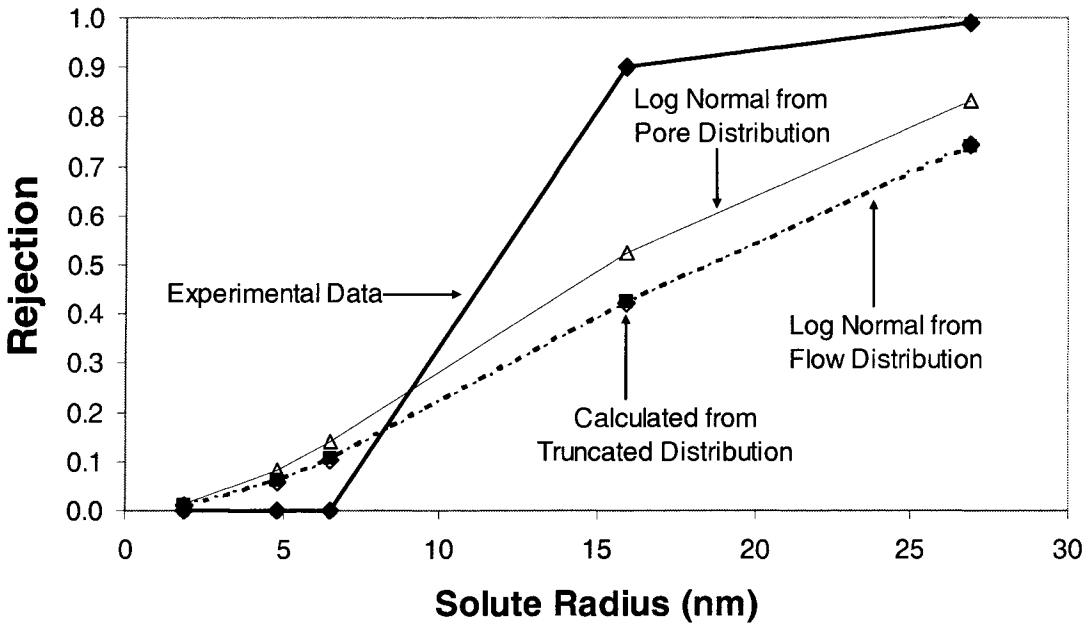

Figure 3.11: Calculated rejection as a function of solute (Dextran) radius.

The rejection model assumes cylindrical pores. Any slight constrictions in the pore wall will restrict the passage of Dextran molecules and result in larger-than-calculated Dextran rejection. Slight constrictions do not have the same impact on flux calculations.

3.5 Conclusions

The SEM images of the cellulose acetate ultrafiltration membrane clearly showed the difference in the pore size distribution between the functional closed side of the membrane and the structural open side of the membrane. The images were analyzed to determine the discrete surface pore size distribution for the closed side of the membrane. The discrete distribution was well described by a log-normal distribution.

The three distributions were used in predictive flux and solute rejection calculations. The discrete distribution and the log-normal distribution fit from the normalized flow calculations are in strong agreement with the experimental flux measurements. The log-normal distribution fit to the pore radius distribution better predicts the Dextran rejection profile than either the discrete data or log-normal distribution fit from the normalized flow calculations. Calculations based on the pore size distribution of the surface images of the ultrafiltration membrane well characterize the physical system.

Chapter 4

SUCROSE HYDROLYSIS AND DEGRADATION PRODUCTS UNDER CORN STOVER PRETREATMENT CONDITIONS

4.1 Abstract

Agricultural and herbaceous feedstocks may contain appreciable levels of sucrose. The goal of this study was to evaluate the survivability of sucrose and its hydrolysis products, fructose and glucose, during dilute sulfuric acid processing at conditions typically used to pretreat lignocellulose biomass. Solutions containing 25 g/l sucrose with 0.1% to 2.0% (w/w) sulfuric acid concentrations were treated at temperatures of 160°C to 200°C for 3 to 12 min. Sucrose was observed to completely hydrolyze at all treatment conditions. However, appreciable concentrations of fructose and glucose were detected and glucose was found to be significantly more stable than fructose. Different mathematical approaches were used to fit the kinetic parameters for acid-catalyzed thermal degradation of these sugars.

The primary degradation products of fructose and glucose were measured. The concentration of 5-hydroxymethalfurfural (5-HMF) was maximized under conditions of a combined severity factor (CS) of approximately 2. Conditions with a higher severity factor degraded 5-HMF into formic and levulinic acid. Conditions with a lower severity factor degraded less fructose and glucose and produced less 5-HMF. A total carbon

balance based on initial sucrose concentrations and measured degradation products indicates additional reaction pathways under combined severity factors greater than 2.0. The presence of additional reaction pathways is supported by the observation of solid precipitates forming during the experimental work.

This work demonstrated that both sucrose-derived glucose and fructose can survive dilute acid pretreatment to various extents depending upon the severity of the pretreatment conditions employed. This implies that the possibility exists to improve the total amount of sugars available from agricultural and herbaceous materials available for conversion to ethanol and other products.

4.2 Introduction

Cellulose and hemicellulose in lignocellulosic feedstocks are a source of renewable sugars that could be converted to a variety of products. However, a number of thermochemical and biochemical processing steps are necessary to convert these polymers to monomeric sugars. Once in monomeric form, the sugars may be converted by fermentative microorganisms into ethanol or other products. Typically, the ability of cellulase to hydrolyze cellulose to glucose is improved by a thermochemical pretreatment step. Although, many pretreatment technologies have been investigated (Wyman et al. 2005), dilute sulfuric acid pretreatment is commonly used. It has been shown to effectively hydrolyze hemicellulose and make the cellulose amenable to enzymatic conversion (Lloyd and Wyman, 2005; Schell et al. 2003).

Recent work at the National Renewable Energy Laboratory (NREL) has focused on conversion of corn stover to ethanol. Corn stover contains appreciable levels of sucrose (2-10% w/w) that vary depending on when the stover is harvested as well as the environmental conditions the stover is exposed to after harvesting. New technologies such as single pass harvesting are expected to preserve even more of the sucrose present in stover. Recovering this sugar provides an additional fermentable carbon source that could improve process economics. Sucrose could be recovered prior to pretreatment, but the economic viability of adding an extraction step is doubtful because the additional water requirement will increase cost. The other possibility is that sucrose or its immediate hydrolysis products, glucose and fructose, survive pretreatment and are available to microorganisms. Recent work has suggested that sucrose-derived glucose and fructose may survive dilute acid pretreatment (Agblevor et al. 2004).

Sucrose is a dimer composed of two sugar monomers, β-D-fructose and α-D-glucose. Under acidic conditions, the glycosidic bond hydrolyses and sucrose breaks down into its two monomer components. Fructose and glucose are known to degrade under the temperature and pH conditions encountered during dilute acid pretreatment. The primary degradation pathway is a dehydration of the sugar to 5-hydroxymethylfurfural (5-HMF), which hydrolyzes and further degrades to levulinic and formic acid (Clarke et al., 1997; Kuster and Temmink, 1977; Mosier et al., 2002; Qian et al., 2005a, 2005b; Xiang et al., 2004).

Model	Kinetic Expression in terms of $[H^+]$	Kinetic expression in terms of pH	Reference
Power law dependence on $[H^+]$, if A = 1, linear dependence on $[H]^+$	$k_S = k[H^+]^A \exp\left(\frac{-Ea}{RT}\right)$	$k_S = k\exp\left(-\frac{ApH}{\log e} - \frac{Ea}{RT}\right)$	Torres et al., 1994; Mosier, 2002
Exponential rate dependence on $[H^+]$	$k_S = k\exp(b[H^+])\exp\left(\frac{-Ea}{RT}\right)$	$k_S = k\exp\left(b\exp(\frac{-pH}{\log e}\right)\exp\left(\frac{-Ea}{RT}\right)$	Torres et al., 1999
Sum of kinetic constants for rate dependence on pH	$k_S = (k^O + k^H[H^+])\exp\left(\frac{-Ea}{RT}\right)$	$k_S = \left(k^O + k^H \exp\left(\frac{-pH}{\log e}\right)\right)\exp\left(-\frac{Ea}{RT}\right)$	Kuster and Temmink, 1977; Schell et al., 2003; Xiang et al., 2004

Table 4.1: Summary of models reported in the literature to describe the rate dependence for acid-catalyzed hydrolysis reactions on pH.

The rate of acid-catalyzed sucrose hydrolysis has been extensively studied due to its importance to both the commercial sugar industry and as a means to study thermal degradation in the food processing industry (Clarke et al., 1997). Kinetic models of sucrose hydrolysis that are most applicable to dilute acid pretreatment conditions must account for both high temperatures (>150°C) and low pHs (<2.5).

Some of the kinetic expressions that have been proposed for the acid catalyzed hydrolysis of sucrose are summarized in Table 4.1. Kinetic expressions in terms of the hydrogen (hydronium) ion concentration [H^+] or pH are given. Early work modeling sucrose hydrolysis assumed a first order reaction with respect to sucrose concentration. The temperature dependence of the reaction rate was found to be well described by the Arrhenius equation over a large range of temperatures (Vukov, 1965). Additionally, the activation energy for hydrolysis was shown to be independent of the pH of the solution (Torres et al., 1994; Vukov, 1965), while the kinetic rate constant was observed to increase exponentially with decreasing pH (Vukov, 1965). The rate limiting step in sucrose hydrolysis and glucose degradation is the protonation of the hydrolxyl group on the sugar ring (Clark et al, 1997; Qian et al., 2005a, 2005b). Lowering the pH of the solution increases the concentration of protons in solution and therefore increases the rate of the hydrolysis and degradation reactions.

Additional work at temperatures near 100°C has also used the Arrhenius equation for temperature dependence of the rate constant and has added an additional term to the rate constant to account for effects of solution pH. An exponential dependence of the rate

constant on pH (linear with respect to H+ concentration) and has been studied over a pH range from 0.8 to 2.5 using nitric acid as a catalyst (Torres et al., 1994). Later work used a different experimental apparatus and a linear dependence of the rate constant with respect to H^+ concentration was observed over a pH range of 0.8 to 1.5. In both cases, the pH of the sucrose hydrolysis solution was experimentally verified to remain constant and did not change as the sucrose was hydrolyzed into fructose and glucose. A third relationship between the rate constant and pH has also been used to model experimental data. Since water is known to be both a proton donor and a proton acceptor, the effect of the water (solvent factor) was included as a constant in the calculation of the rate constant with a linear dependence on H^+ concentration (Kuster and Temmink, 1977; Schell et al., 2003; Xiang et al., 2004).

Errors in estimating kinetic parameters can occur when heat up time from room temperature to the steady state temperature is significant compared to time at the constant reaction temperature (Sadeghi and Swartzel, 1990). Two approaches are generally used to determine the reaction time for parameter estimation. The first method is to subtract a fixed amount of time from the reaction time to compensate for the heat up time, or alternately, define time zero when sample temperatures reaches near or at the desired steady state temperature. The second approach is to integrate the reaction rate over the reaction time with respect to the temperature profile (Swartzel, 1982). Integration of the reaction rate over time is the basis of using non-isothermal methods for the analysis of chemical time-temperature indicators to measure degradation of products during pasteurization (Torres et al., 1994, 1999). Non-isothermal methods are also used to

increase the efficiency of data collection for kinetic parameters of Arrhenius type systems since fewer experimental runs are required to cover a range of temperatures (Torres et al., 1994).

In this work, two different approaches were used to determine the degradation parameters for fructose and glucose. As the rate of degradation of fructose was high, the residual concentration in solution was often very low. Thus, calculating the fructose degradation kinetic parameters required numerical integration of the reaction rate based on the temperature profile. Since the rate of degradation of glucose was much slower, glucose was always detected after hydrolysis. Consequently, calculating the glucose degradation kinetic parameters required correcting the reaction time based on the temperature profile.

The objective of this work was to investigate the kinetics of sucrose hydrolysis under biomass pretreatment conditions with the goal to improve understanding of the fate of sucrose during dilute acid pretreatment. These experiments used pure sugars with the knowledge that these solutions may not accurately represent conditions in true biomass hydrolysates; nevertheless, investigating degradation behavior using pure sugars is a reasonable starting point. Experiments were conducted at temperatures from 160°C to 200°C for reaction times of 3 to 12 min at sulfuric acid concentrations of 0.1% to 2.0% (w/w). These ranges span typical dilute sulfuric acid biomass pretreatment conditions (Schell et al., 2003).

4.3 Materials and Methods

4.3.1 Experimental and Analytical Proceedures

High-purity sucrose was purchased from Sigma-Aldrich (St. Louis, Missouri). High purity sulfuric acid was purchased from Mallinckrodt Baker (Paris, Kentucky). All aqueous solutions were made up using deionized water. Stock sample solutions were prepared containing 25 g/l sucrose at five different sulfuric acid concentrations [0.1%, 0.4%, 1.0%, 1.5%, 2.0% (w/w)]. Sample solutions were placed in Hastelloy C reaction bombs made of 1.3 cm internal diameter (0.5 in) Swagelok (Cleveland, OH) tube unions sealed at each end with caps. Experimental runs consisted of loading five bombs with acidic sucrose solutions, while a sixth bomb contained water and was fitted with a thermocouple to monitor the temperature profile. Temperature data was logged every 5 seconds using a Digi-Sense scanning thermocouple thermometer (Cole-Palmer, Vernon Hills, Illinois). The six bombs were secured in an open mesh wire basket and inserted into a preheated SBL-2D fluidized sand bath (Techne, Staffordshire, UK). Three steady state reaction temperatures were tested, 160°C, 180°C, and 200°C. Samples evaluated at the 160°C and 180°C conditions were initially heated in a separate fluidized bath at 210°C until they were within 10°C of the required temperature, at which point they were transferred to the fluidized bath controlled at the steady state temperature. Samples treated at 200°C were not preheated and instead inserted into a 200°C fluidized bath. Samples were treated for nominal reaction times of 3, 5, 8, and 12 min with 0.1, 0.4 and 1.0% (w/w) sulfuric acid and for 3, 5, and 8 min with 1.5 and 2.0% (w/w) sulfuric acid at all three temperatures. The nominal reaction time was defined as the time between

insertion of the bombs into the first fluidized sand bath and quenching in ice water at the end of the desired reaction time.

4.3.2 Analytical methods

Sucrose, fructose, and glucose concentrations were measured using an Agilent 1100 (Palo Alto, California) HPLC with a refractive index detector (RID) and an Alltech (Deerfield, Illinois) Carbohydrate ES column. The isocratic mobile phase was 25% (v/v) water and 75% (v/v) acetonitrile at a flow rate of 1 ml/min. Both the column and RID were maintained at 30°C. High-purity fructose and glucose were purchased from Sigma-Aldrich (St. Louis, Missouri). Five mixed sucrose, fructose, and glucose calibration standards were used containing each of these sugars at concentrations of 0.32, 1.28, 5.12, 10.0, and 25.0 g/l. A linear calibration ($R^2 > 0.9996$) was obtained for all sugars. A validation standard containing 15.0 g/l of each sugar was prepared and run with the treated samples as a quality control check to verify the accuracy of the calibration. Method accuracy was calculated as the absolute value of the difference between the known sugar concentration and the average of the measured sugar concentration, divided by the known sugar concentration. The accuracy of the sucrose measurement was 2.0% while the accuracy of the fructose and glucose measurements was 0.25% on a relative basis. All samples were neutralized with lime, refrigerated overnight at approximately 4 °C, and cold filtered with a 10 μm nylon filter prior to analysis.

Formic acid, levulinic acid, and 5-HMF concentrations were measured using an Agilent 1100 (Palo Alto, California) HPLC with a refractive index detector (RID) and a Bio-Rad

(Hercules, California) HPX-87H column using a 0.01 N sulfuric acid mobile phase per a previously published analytical method (Schell et al., 2004). The mobile phase flow rate was 0.6 ml/min with a 6 µl sample injection volume. The column and the RID were maintained at 65°C. High-purity formic acid, levulinic acid, and 5-HMF was purchased from Sigma-Aldrich (St. Louis, Missouri).

After treated samples cooled to room temperature, the pH was measured using an Orion 520 A+ pH meter (Thermo Electron Corporation, Boston, Massachusetts).

4.3.3 Kinetic model selection

The first-order kinetic expression used to model fructose and glucose concentration is:

$$\frac{C}{C_O} = \exp(-k_S t) \tag{4.1}$$

where C is the instantaneous sugar concentration (mol/l or g/l), C_O is the initial sugar concentration (mol/l or g/l), k_S is the kinetic rate constant for hydrolysis or degradation (min^{-1}), and t is reaction time (min). The temperature dependence of the hydrolysis or degradation rate is modeled using the Arrhenius relationship (Equation 4.2) where k is a dimensionless pre-exponential constant, Ea is the activation energy (J/mol), R is the universal gas constant (8.3144 J mol^{-1} K^{-1}), and T is temperature (°K).

$$k_S = k \exp\left(\frac{-Ea}{RT}\right) \tag{4.2}$$

Three different expressions for the specific reaction rate k_S reported in the literature were used to model sugar hydrolysis and degradation kinetics under varying pH conditions. All three expressions are based on a first order exponential decay system and incorporate pH dependence. Table 4.1 summarizes the three different models.

4.3.4 Kinetic parameter estimation for fructose degradation – The ODE method

The kinetic parameters for fructose degradation were determined by constructing an ordinary differential equation from a linearized form of Equation 4.1 (see Equation 4.3) where both fructose concentration and temperature change with time.

$$d\ln\left(\frac{C(t)}{C_o}\right) = -k_S(t)dt \tag{4.3}$$

Assuming pH remains constant at a fixed acid concentration, Equation 2 can be substituted into Equation 4.3 (see Equation 4.4) in which the pre-exponential factor, k, is a function of pH. With these assumptions, the reaction rate at a fixed pH is a function of the fitted parameters k and Ea and the temperature profile.

$$d\ln\left(\frac{C(t)}{C_o}\right) = -k\exp\left(\frac{-Ea}{RT(t)}\right)dt \tag{4.4}$$

The temperature measured at each 5 sec interval was used to calculate an instantaneous reaction rate. This was then used to determine the new fructose concentration present in solution. A typical temperature profile, calculated reaction rate, and calculated fructose

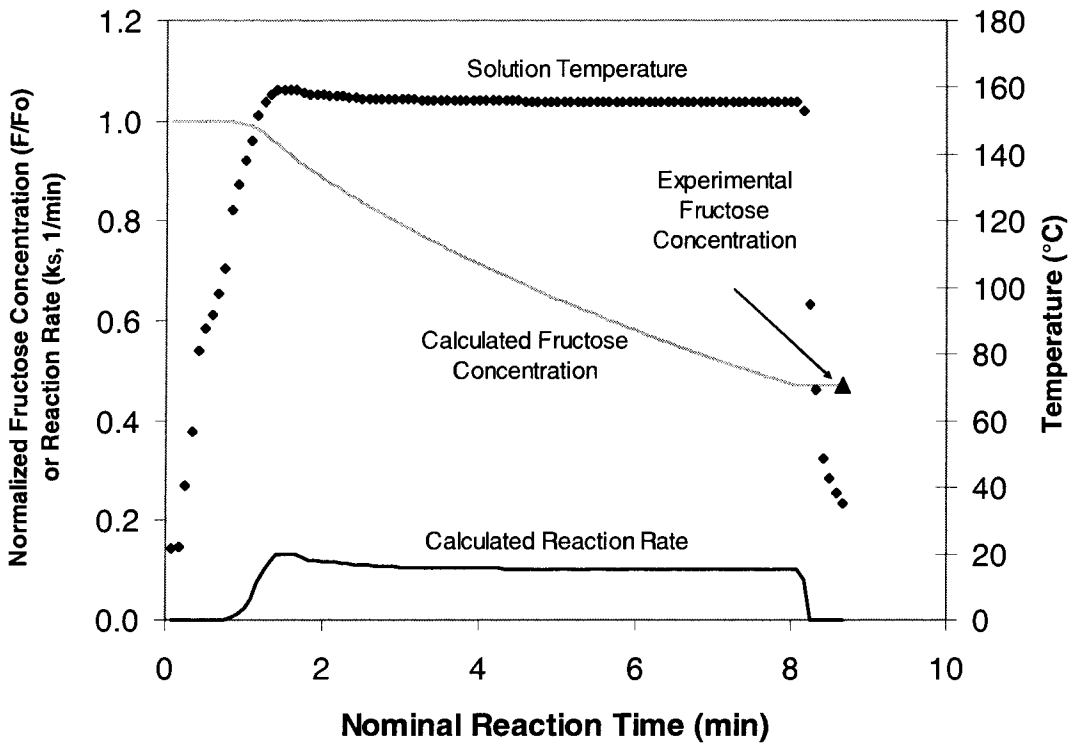

Figure 4.1: Temperature profile and calculated reaction rate for a 0.4% (w/w) sulfuric acid, 160 °C and an 8-min nominal reaction time sample. The calculated fructose concentration was compared to the experimental fructose concentration to determine the kinetic parameters k and Ea.

concentration are shown in Figure 4.1. This method was applied at each treatment condition (nominal reaction time, temperature, and acid concentration) using a 4^{th} order Runge-Kutta method in conjunction with Equation 4.4 to estimate the kinetic parameters (k and Ea). The calculated fructose concentration was compared to the measured value and used to estimate kinetic parameters. One activation energy (Ea) and 5 pre-exponential values ($k_{0.1\%}$, $k_{0.4\%}$, $k_{1.0\%}$, $k_{1.5\%}$, $k_{2.0\%}$ corresponding to the various sulfuric acid concentrations) were simultaneously fit to all of experimental data using the non-linear least-square regression package from MATLAB (MathWorks, Natick, MA). The procedure will subsequently be referred to as the ODE (ordinary differential equation) method in this work.

4.3.5 Kinetic parameters estimation for glucose degradation – linearization and regression

The glucose degradation kinetic parameters were determined by performing linear regressions on kinetic rate constants calculated from the initial and final glucose concentrations and the reaction time according to Equation 4.5. The calculations assumed a constant pH within each acid concentration group (0.1%, 0.4%, 1.0%, 1.5%, 2.0% w/w H_2SO_4) for all reaction temperatures and nominal reaction times based on experimental pH measurements. Equation (4.1) was linearized and rewritten to calculate the degradation rate constant for each sample (Haralampu et al., 1985).

$$k_S = \frac{-\ln\left(\frac{C}{C_o}\right)}{t} \tag{4.5}$$

The kinetic parameters k and Ea were calculated from a least-square fit of resulting k_s values versus temperature using the linearized form of Equation 4.2 given in Equation 4.6 without needing to know the specific dependence of k on pH.

$$\ln(k_s) = \left(\frac{-Ea}{R}\right)\left(\frac{1}{T}\right) + \ln(k) \tag{4.6}$$

A different value for k was calculated at each sulfuric acid concentration. The value of Ea was assumed to be independent of sulfuric acid concentration and one value for Ea was determined for all the data sets.

As with the fructose degradation calculation, sample temperature was not constant during each run. Since Equations 4.5 and 4.6 require a constant temperature and reaction time, the changing temperature for each sample was accounted for by calculating an equivalent reaction time (t_{EQ}, min) at the steady state nominal temperature (T_{SS}, °K) that achieves the same degree of glucose degradation as the time (t_M, min) and temperature (T_M, °K) measured for each increment in the temperature profile. Calculation of t_{EQ} was done by holding the exponential term in Equation 4.1 constant (Equation 4.7), substituting for the steady state ($k_{S,SS}$, min^{-1}) and measured ($k_{S,M}$, min^{-1}) rate constants based on the Arrhenius relationship expressed by Equation 4.2 (Equation 4.8), and solving for t_{EQ} (Equation 4.9).

$$k_{S,SS}\, t_{EQ} = k_{S,M} t_M \tag{4.7}$$

$$k \exp\left(\frac{-Ea}{RT_{SS}}\right) t_{EQ} = k \exp\left(\frac{-Ea}{RT_M}\right) t_M \tag{4.8}$$

$$t_{EQ} = \frac{t_M}{\exp\left(\frac{Ea}{R}\left(\frac{1}{T_M} - \frac{1}{T_{SS}}\right)\right)} \tag{4.9}$$

The equivalent reaction time was calculated for each temperature time increment (every 5 seconds) in the temperature profile and the equivalent reaction times for each increment were summed to determine the overall equivalent reaction time for calculation of $k_{S,SS}$ using Equation 4.5. A typical temperature profile and equivalent reaction time are shown in Figure 4.2.

The experimental values for $1/T_{SS}$ were plotted versus $\ln(k_{S,SS})$ and linear regressions performed for each acid concentration data set to calculate one activation energy (Ea) and 5 pre-exponential values ($k_{0.1\%}$, $k_{0.4\%}$, $k_{1.0\%}$, $k_{1.5\%}$, $k_{2.0\%}$) simultaneously using a least-squares minimization in MATLAB (MathWorks, Natick, MA). In Equation 4.9, t_{EQ} is a function of t_M, Ea, T_M, and T_{SS} where T_{SS} is the nominal temperature for each experiment and t_M is the time increment of the temperature data recorder. T_M was measured at each time increment. The determination of the activation energy for glucose degradation required iteration until the activation energy used to calculate the equivalent reaction time was the same as the activation energy calculated from the linear regression.

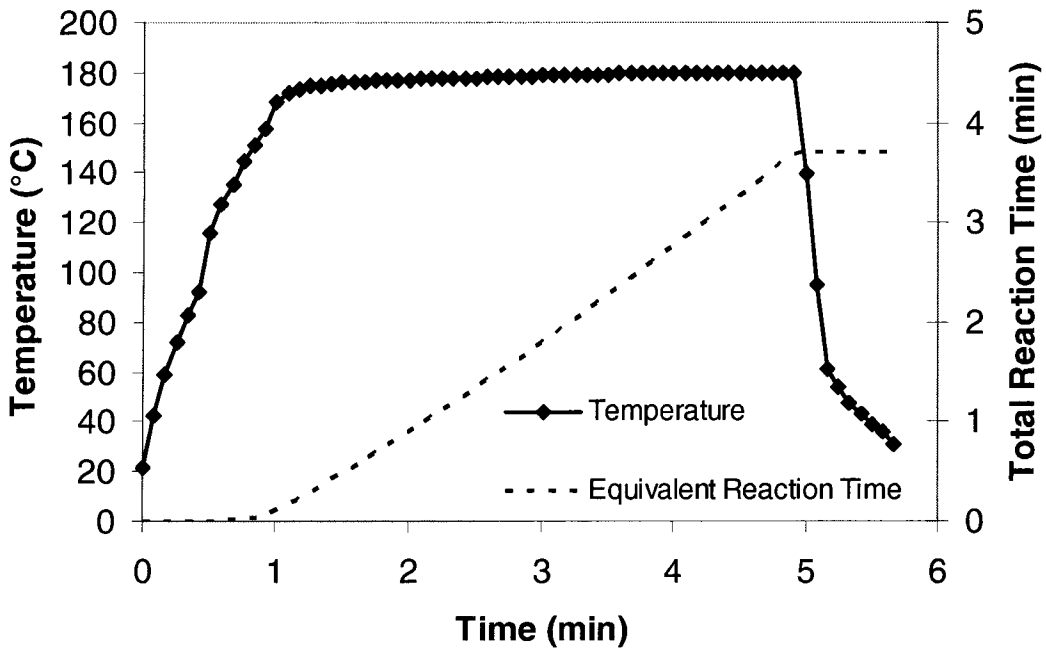

Figure 4.2: A typical temperature profile for the solution inside the thermal bomb. The specific example used was from the nominal 5-minute reaction time at 180 °C. The total reaction (rxn) time plotted on the second ordinate axis is calculated from the temperature profile for glucose with experimentally determined activation energy of 113 KJ/mol. The 5-minute nominal reaction time sample has an equivalent reaction time of 3.6 minutes for glucose.

4.3.6 *Temperature Distribution inside Hastelloy Bomb*

The temperature distribution inside the hastelloy bomb was estimated using a lumped parameter model. The lumped parameter model estimates the temperature of a solid object inserted in a fluid medium as a function of time, the temperature of the fluid medium, the initial temperature of the solid object, and the physical properties (heat conductivity, specific heat, etc.). The shrinking temperature differential between the solid object and fluid medium reduces the rate of heat transfer between the object and the medium which in turn slows down the temperature change of the object. The rate of temperature change in the hastelloy bomb (solid object) is important to the experimental conditions because the rate of sucrose hydrolysis and degradation are highly dependent on the temperature of the solution. Temperature gradients within the bomb would create unequal reaction rates and greatly complicate kinetic rate studies. Properly estimating the reaction kinetic parameters for the hydrolysis and degradation reactions is not possible without understanding the temperature gradients within the bomb. The simplest way to approximate the temperature gradient within the bomb is to calculate the Biot number (*Bi*). The Biot number is a dimensionless number relating the convection coefficient (*h*, $w/m^2 \cdot K$), the characteristic length of the object (L_c, m), and the conductivity of the solid (*k*, w/m·K). The characteristic length of the solid is the volume to area ratio and changes depending on the shape of the object. For a wall of thickness $2L$, $L_c=L$. For a cylinder of radius *r*, $L_c=r/2$. For a sphere of radius *r*, $L_c=r/3$. The equation for calculating the Biot number is:

$$Bi = \frac{hL_c}{k} \tag{4.10}$$

When the Biot number is ≤ 0.1, there are negligible temperature gradients within the solid and the total solid can be treated as one temperature for the lumped body temperature calculation.

The lumped body model requires two conditions. First, the temperature of the object must be approximately equal throughout (negligible temperature gradients). Second, the volume of the fluid must be sufficiently large such that its temperature does not change as the solid changes temperature. The second condition can also be met through temperature regulation of the fluid. When both conditions are met, the temperature inside the bomb can be estimated using the relationship:

$$\frac{T(t)-T_{\infty}}{T_i-T_{\infty}} = \exp\left(-\frac{hA}{mc_p}t\right) \tag{4.11}$$

Where $T(t)$ is the temperature of the solid (°C), T_{∞} is the temperature of the fluid (°C), T_i is the initial temperature of the solid, A is the surface are of the object (m^2), c_p is the specific heat of the solid (J/g·K), t is the time after submersion of the solid in the fluid (seconds).

4.3.7 Combined Severity Calculation

The combined severity factor (CS) couples pH, reaction time, and temperature into a single factor that can be used to compare performance at various treatment conditions (Overend and Chornet, 1987). Ideally, two treatments at the same CS will hydrolyze

and/or degrade solution components equivalently. The CS was calculated from equation 4.12 (Nguyen et al., 1999).

$$CS = \log_{10}(t_{EQ} \cdot \exp[(T_{SS} - 100)/14.75]) - pH \qquad (4.12)$$

Where t_{EQ} is the equivalent reaction time for the component in minutes and T_{SS} is the equilibrium reaction temperature in °C.

4.4 Results and Discussion

4.4.1 Sucrose, Fructose, Glucose HPLC Method Development

An HPLC method was developed to separate and quantify sucrose, fructose and glucose concentrations in the dilute acid sucrose samples. The method utilized a new chromatography column unproven at NREL. The method development served two purposes; evaluating the Alltech Carbohydrate ES chromatography column for rapidly separating chemically similar sugar monomers and dimers and determining the sucrose, glucose, and fructose concentrations in the dilute acid sucrose samples after being subjected to pretreatment conditions. As noted in the *Materials and Methods* section for Chapter 4, the method was optimized using an isocratic binary mobile phase containing 25% (v/v) water and 75% (v/v) acetonitrile at a flow rate of 1 ml/min. The sample injection volume was optimized to 20 µl. Higher sample injection volumes saturated the column. Lower sample volumes showed reduced sensitivity (higher lower limits of quantification). The temperature of the chromatography column and the RID was

maintained at 30 °C to reduce the viscosity of the mobile phase. Figure 4.3 shows the chromatogram generated from the 10 mg/ml (each) sucrose, fructose, and glucose standard. The chromatogram clearly shows the baseline peak separation of the method. The initial, unlabeled, peak in the chromatogram is a solvent front generated by the injection of the aqueous sample. The change in the characteristics of the mobile phase was easily detected by the refractive index detector.

The analytical method was evaluated for accuracy, precision (coefficient of variation, CoV, standard deviation / mean), and lower level of detection (LLD, 10 times standard deviation of the baseline noise). The slope, intercept, and linearity of the calibration curve were also determined. These values are included in Table 4.2.

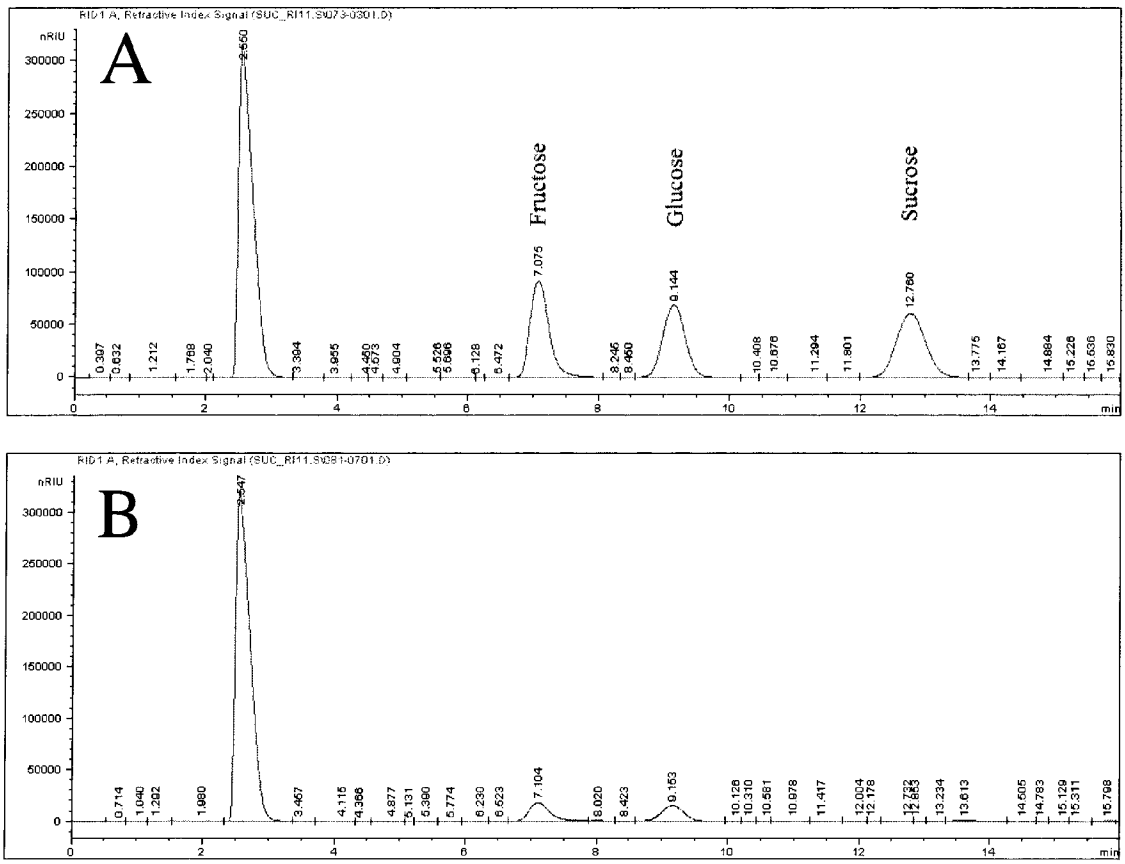

Figure 4.3: A) A typical chromatogram from the new HPLC-RID method for sucrose, fructose, and glucose quantification. The method obtains baseline separations of the sugar peaks and has a total cycle time of 18 minutes. B) Sample chromatogram from a 3 minute nominal reaction time, 160 °C sample containing 0.1% (w/w) sulfuric acid.

Sugar	Accuracy (%)	Precision (CoV)	LLD (g/L)	Retention Time (minutes)	Slope ((nRIU*s)/ (g/l))	Intercept (nRIU*s)	R^2
Sucrose	2.00	0.241	0.084	12.7	182126	23258	0.999
Fructose	0.223	0.920	0.212	7.1	177496	837.25	0.996
Glucose	0.070	0.697	0.139	9.1	148720	17902	0.998

Table 4.2: Values determined during HPLC-RID method calibration and validation.

4.4.2 *Temperature Gradients and Heating Times*

The temperature gradients within the bomb were evaluated both by estimation of the Biot number using Equation 4.10 and comparison of the lumped parameter model to experimental data for the temperature profile of the sample within the bomb as a function of time. The sample bomb consisted of two components, the outer hastelloy C pipe fittings and the aqueous sample inside the pipe fittings. The thermal conductivity of the hastelloy was higher and the specific heat was lower than water. With a lower thermal conductivity and a higher specific heat, temperature gradients were more likely to form in the aqueous sample than in the walls of the hastelloy piping. The Biot number was calculated using a vendor supplied (Techne, Staffordshire, UK) convection coefficient for heat transfer from the fluidized sand to metal of 500 $w/m^2 \cdot K$ (a range of 340 to 680 $w/m^2 \cdot K$ was cited as typical), the characteristic length of the outside dimension of ½" hastelloy pipe fittings, and the thermal conductivity of water. A Biot number of $Bi = 0.26$ was calculated from these assumptions. The value of 0.26 is slightly higher than the typical upper limit of 0.1 for using the lumped parameter model.

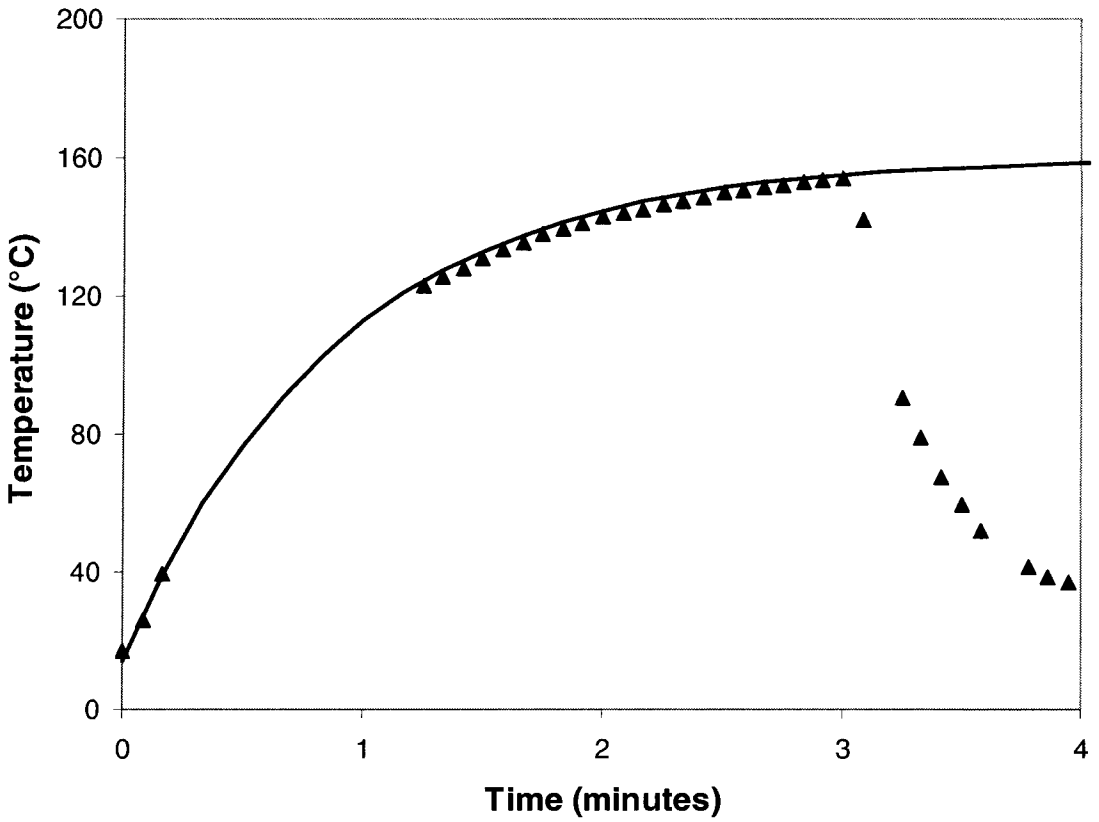

Figure 4.4: Temperature profile of the hastelloy sample bomb in a 160°C fluidized sand bath. The bomb was removed after 3 minutes and quenched in an ice bucket. The solid line represents the lumped body model and the triangles are instantaneous experimental temperatures.

The temperature profile for the aqueous sample in the bomb was experimentally measured using a hastelloy bomb filled with water and fitted with a thermocouple inserted through the center axis of the cylindrical bomb. This was the same thermocouple/bomb used to measure the sample temperature over time in subsequent experiments. Figure 4.4 plots the experimentally measured temperature inside the bomb as a function of time. Also shown in Figure 4.4 is the lumped body model calculated from Equation 4.11 using the estimated convection coefficient for heat transfer from the fluidized sand to hastelloy of 500 $w/m^2 \cdot K$, the surface area of the ½" hastelloy pipe fittings, and the specific heat of water. The lumped body model accurately describes the measured temperature inside the bomb as a function of time despite the Biot number being slightly out of range. Subsequent hydrolysis and degradation kinetic calculations assume no temperature gradients within the aqueous sample in the bombs as the samples heat up and cool down.

4.4.3 Temperature Profile and Equivalent reaction time

A temperature profile for a nominal 5 minute reaction time at 180 °C is shown in Figure 4.2 and was a typical temperature profile of all the runs. The equivalent reaction time plotted on the right ordinate axis was calculated from the temperature profile using Equation 4.9 and an activation energy of 113 kJ/mol and is included to visually illustrate the effect of heat up time on the estimated reaction time. The 5 minute nominal reaction time is equivalent to a reaction time of 3.6 min. This technique provides a method for normalizing the effect of non uniform temperatures on reaction kinetics for thermally sensitive samples.

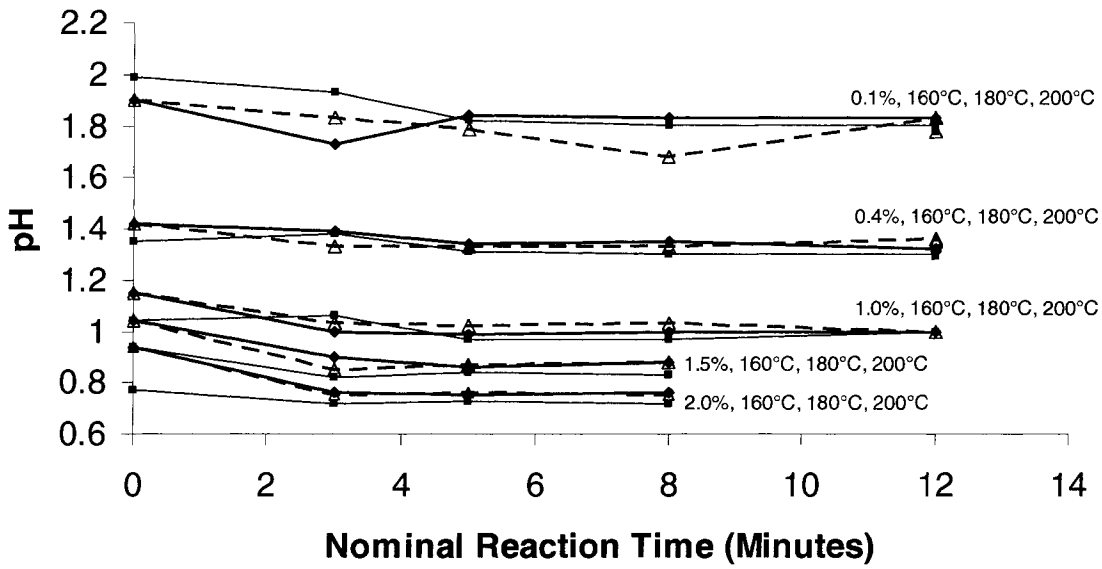

Figure 4.5: Sample pH for different reaction conditions. The pH for each sulfuric acid concentration remained approximately constant for all temperatures and nominal reaction times. The sample pH was assumed to be constant and the average pH for each sulfuric acid concentration was used for subsequent calculations.

4.4.4 *Post-Hydrolysis Sample pH*

The room temperature pH of the sucrose samples after subjection to various pretreatment conditions remained constant for all five of the sulfuric acid concentrations evaluated in this work (Figure 4.5). Constant pH was observed by Torres and Oliveira (1999) under similar un-buffered conditions and low pH. Average sample pH was the same for all pretreatment temperatures at the same acid concentration. The measured pH values were: 1.81 for 0.1% (w/w) sulfuric acid, 1.33 for 0.4% (w/w) sulfuric acid, 1.01 for 1.0% (w/w) sulfuric acid, 0.86 for 1.5% (w/w) sulfuric acid, and 0.74 for 2.0% (w/w) sulfuric acid. These values were used in subsequent calculations for the relationship of pre-exponential rate constants and pH and calculate the combined severity factor.

4.4.5 Sucrose Concentrations

Sucrose was not detected in any treated samples as it quickly hydrolyzed at all of the temperature and pH conditions used in this study, even at the least severe condition of 160°C, 0.1% acid and a 3 min nominal reaction time. However, both fructose and glucose were present in most samples. Previous sucrose hydrolysis studies were conducted at much lower temperatures (100 °C as opposed to 200 °C) or at much higher pH values ($\geq$ 4.0), reaction conditions where some sucrose survives. Thus, sucrose hydrolysis kinetics was not determined because no sucrose survived these treatments.

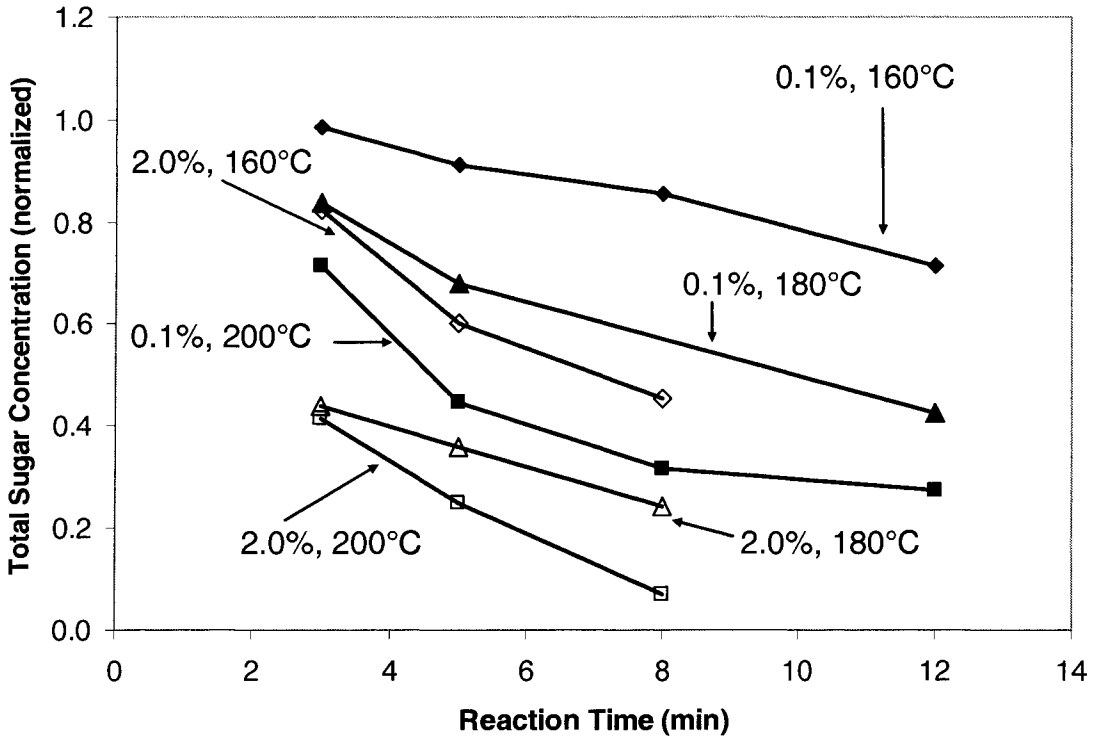

Figure 4.6: Normalized total sugar concentration (sum of fructose and glucose concentration divided by theoretical possible from complete sucrose hydrolysis) as a function of reaction time for various combinations of temperature and acid concentration.

The normalized total sugar concentration (sum of fructose plus glucose divided by theoretical fructose plus glucose from complete sucrose hydrolysis) is plotted as a function of the reaction time at various acid concentration/temperature combinations in Figure 4.6. Since sucrose is completely hydrolyzed, decreasing total sugar concentrations represent loss of fructose and glucose to other degradation products. At the lowest severity conditions (160°C, 0.1% acid) 75% of the sucrose is recovered in the form of fructose and glucose after 12 min of treatment. In contrast, less than 10% of the sugar survives at the highest severity treatments (200°C, 2.0% acid, 8 min). At conditions between these two extremes, which are commonly encountered during dilute acid pretreatment of biomass (Schell et al., 2003), 25% to 80% of the sugars survive and thus are available for conversion to ethanol or other products.

4.4.6 *Fructose Degradation*

Fructose concentration is plotted as a function of the nominal reaction time at various temperature and acid concentration combinations in Figure 4.7. At the lowest severity condition (160°C, 0.1% acid), 95% of the theoretical fructose available from sucrose survived after a 3 min nominal reaction time. However, no fructose survived at mid- to high-severity conditions. The traditional method of fitting Arrhenius kinetic parameters based on linearization and plotting 1/T versus $\ln(k_S)$ was not applied to this data due to the difficulty of accurately determining k_S when fructose completely degraded. Therefore, the ODE method described in the materials and methods section was used to estimate kinetic parameters for fructose degradation.

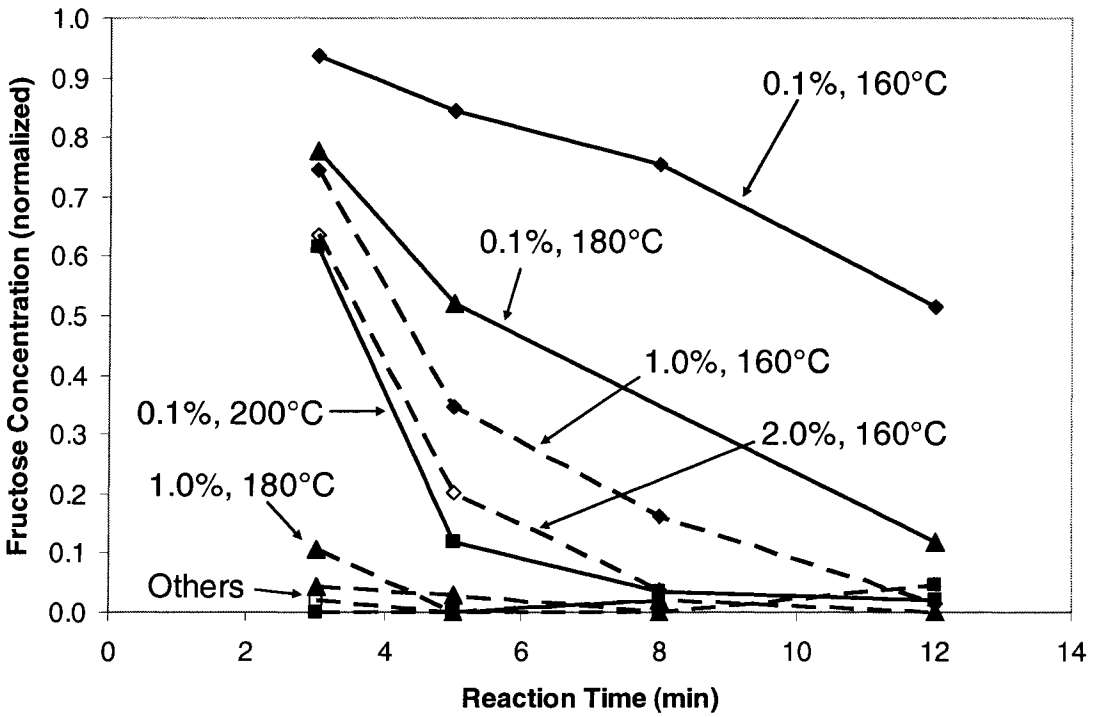

Figure 4.7: Fructose concentration as a function of nominal reaction time for various combinations of temperature and acid concentration. Three conditions resulting in very little recovered fructose are labeled on the graph as "others." These three data sets are for conditions of 200°C, 1.0%; 180°C, 2.0%; and 200°C, 2.0%.

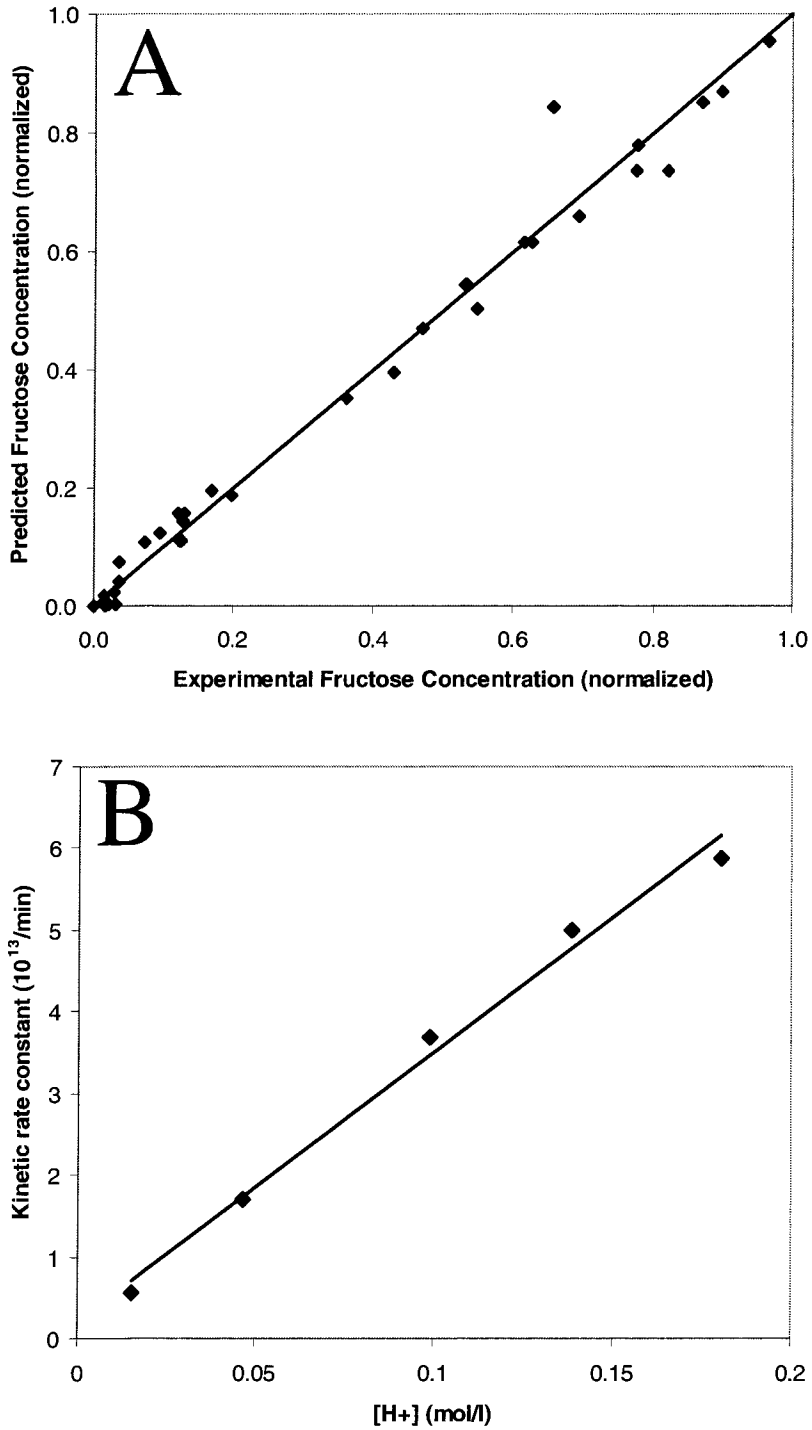

Figure 4.8: Results from the ODE model for fructose degradation showing A) experimental versus predicted fructose concentration and B) kinetic rate constants for fructose degradation as a function of H^+ concentration.

Figure 4.8A plots predicted fructose concentration as a function of the measured concentration. Estimated values for the kinetic parameters are listed in Table 4.3. These parameter values were used in Equation 4.4 in conjunction with the measured temperature profiles to predict the final fructose concentration at each treatment condition. As Figure 4.8A shows, good correlation is obtained between predicted and experimental values. However, one outlier point associated with treatment at a 3 min nominal reaction time, 0.1% acid and 200°C was not well predicted by the kinetic model.

Figure 4.8B shows the dependence of the pre-exponential constant, k, on pH. A linear relationship ($R^2 = 0.99$) between k and $[H^+]$ was observed with a slope of 3.31×10^{14} $l \cdot mol\ H^{+-1} \cdot min^{-1}$ (k^H) and an intercept of 1.92×10^{12} min^{-1} (k^O). The model based on the sum of kinetic constants for rate dependence on pH (Table 4.1, row 3) best describes fructose degradation under the treatment conditions studied in this work. This suggests that the reaction rate dependence on pH includes both solvent and free proton effects. Results show that the rate constant, k_S, behaves similarly to that observed by Kuster and Temmink (1977) for fructose degradation to 5-hydroxymethylfurfural at 175°C over pHs ranging from 1 to 4.

Kinetic Parameter	Fructose	Glucose
Ea (kJ/mol)	117	113
$k_{0.1\%}$ (min^{-1})	5.61×10^{12}	3.10×10^{11}
$k_{0.4\%}$ (min^{-1})	1.70×10^{13}	5.17×10^{11}
$k_{1.0\%}$ (min^{-1})	3.68×10^{13}	6.38×10^{11}
$k_{1.5\%}$ (min^{-1})	5.00×10^{13}	9.87×10^{11}
$k_{2.0\%}$ (min^{-1})	5.87×10^{13}	1.02×10^{12}

Table 4.3: Kinetic parameters for acid-catalyzed thermal degradation of fructose and glucose.

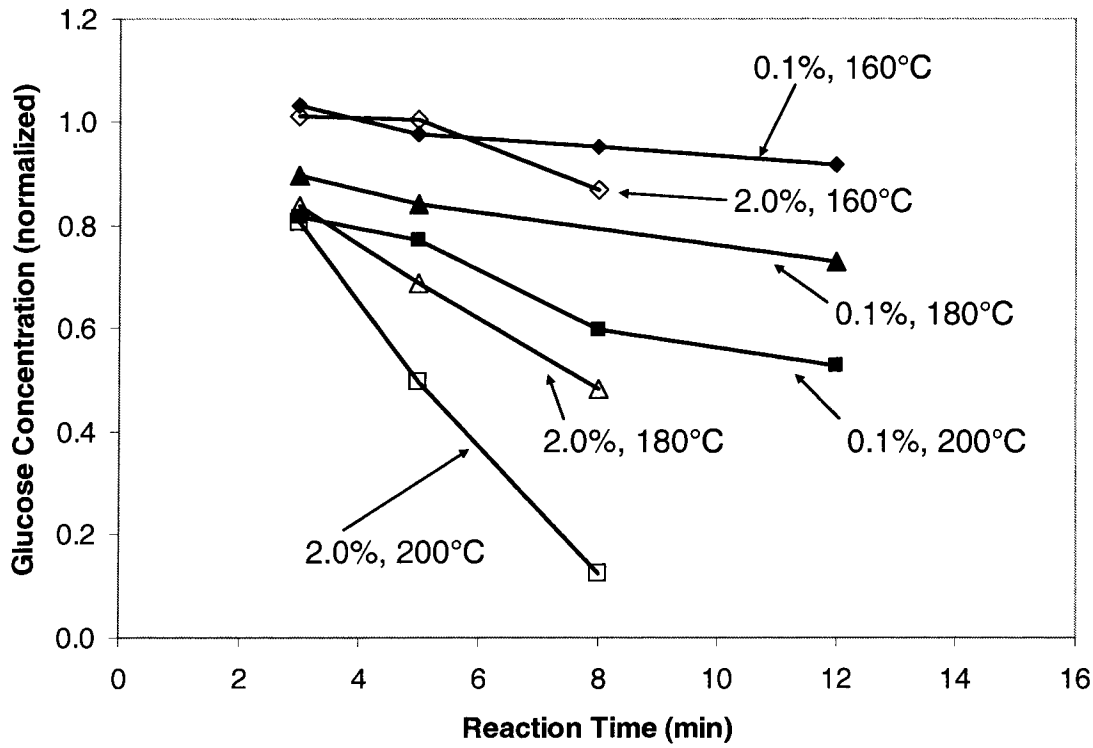

Figure 4.9: Glucose concentration as a function of nominal reaction time for various treatment conditions.

4.4.7 Glucose Degradation

Glucose concentrations are shown as a function of reaction time at various treatment conditions in Figure 4.9. At the least severe condition (160°C, 0.1% acid) 80% of the glucose survives treatment for the longest nominal reaction time (12 min) used in this work, and as expected at increasing severities less glucose survives. But even at the most severe condition (200°C, 2.0% acid) 10% of the glucose survives treatment at nominal reaction times less than 8 min. A comparison of Figures 4.7 and 4.9 clearly illustrates that glucose is significantly more stable than fructose over the range of treatment conditions investigated.

The ODE method used to determine kinetic parameters for fructose degradation was not appropriate for determining glucose kinetic parameters because glucose concentration did not change as rapidly (see Figure 4.9) at the treatment conditions tested. In this case, rate constant parameters were calculated using the linearized form of the Arrhenius equation (Equations 4.5 and 4.6). Pre-exponential factors and activation energy were empirically fit as outlined in material and methods section. The best fit kinetic parameters are given in Table 4.3 and agree well with the results of Mosier et al. (2002), who reported an activation energy of 118 kJ/mol for glucose degradation over a similar temperature and pH range.

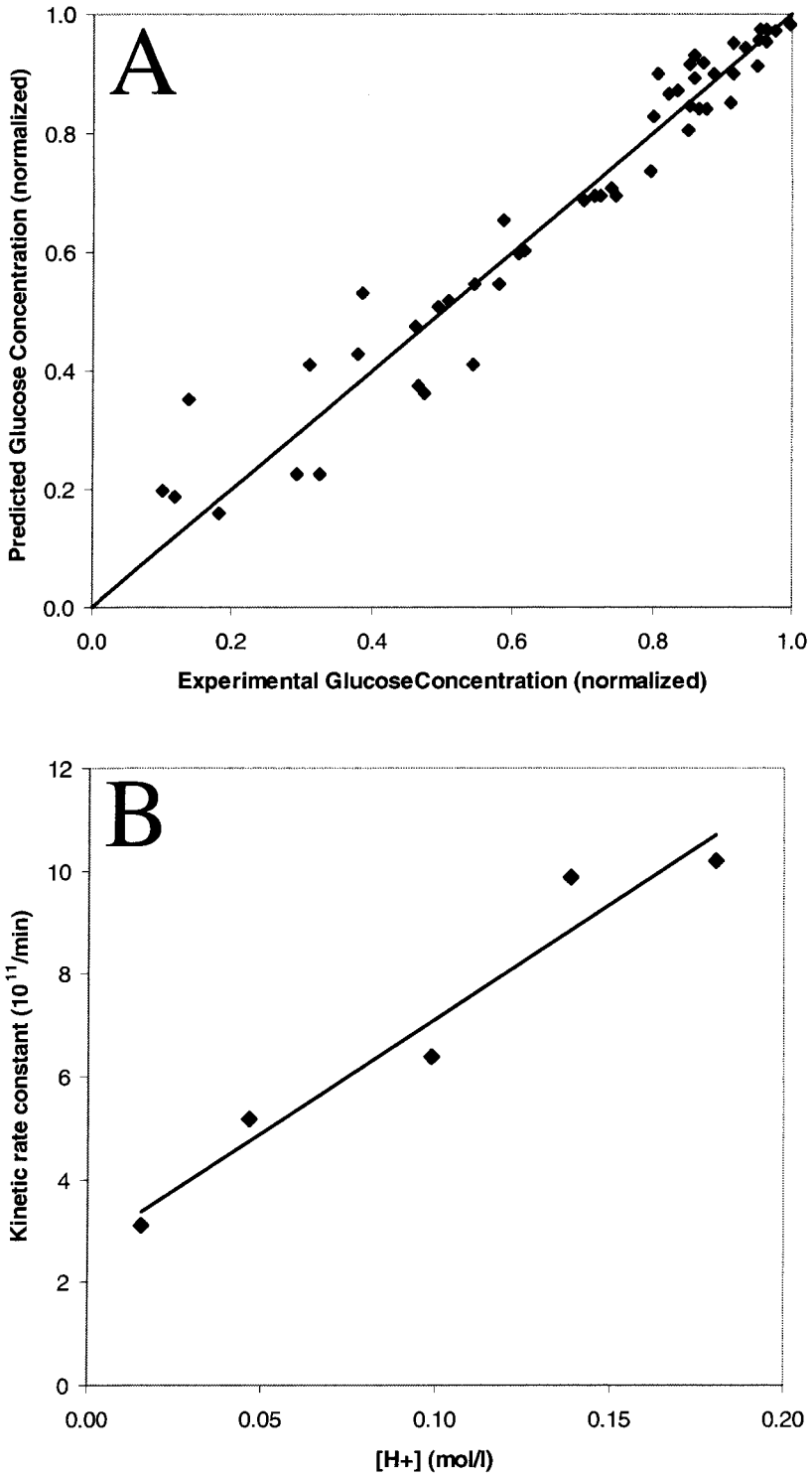

Figure 4.10: Results from the kinetic model for glucose degradation showing A) experimental versus predicted glucose concentration and B) kinetic rate constants for glucose degradation as a function of H^+ concentration.

The resulting kinetic parameters were used in Equation 4.4 along with the measured temperature profile to calculate the predicted glucose concentration at each treatment condition using a 4^{th} order Runge-Kutta method implemented in MatLab. The experimental values are plotted against the predicted values in Figure 4.10A. Although the residuals appear to be well distributed, they increase in magnitude at the more severe reaction conditions. Nevertheless, good fit was achieved at low- to mid-severity conditions and the model can be used to accurately predict glucose concentrations.

A linear relationship (R^2 = 0.95) between k and $[H^+]$ was also observed for glucose degradation as illustrated in Figure 4.10B. The slope of the line is 4.46 x 10^{12} l·mol H^{+-1}·min^{-1} (k^H) with an intercept of 2.67 x 10^{11} min^{-1} (k^O). The sum of kinetic constants for rate dependence model (Table 4.1, row 3,) also is useful for describing glucose degradation kinetics over the range of treatment conditions studied.

4.4.8 Dependence of Kinetic Rate Constant, Ks, on pH and Temperature

The kinetic rate constant, Ks, in Equation 4.1 is a function of the pretreatment conditions, pH and temperature, and the thermodynamic properties of the degradation process; activation energy and pre-exponential constants. To guide the selection of the pretreatment conditions, the relative impact of pH and temperature on the degradation of fructose and glucose were determined by contour mapping the degradation rate constant as a function of either pH or temperature while holding the other variable at different constant values. The advantage to mapping kinetic rate constants in this manner is that thresholds are frequently easy to identify where the behavior of the system is much

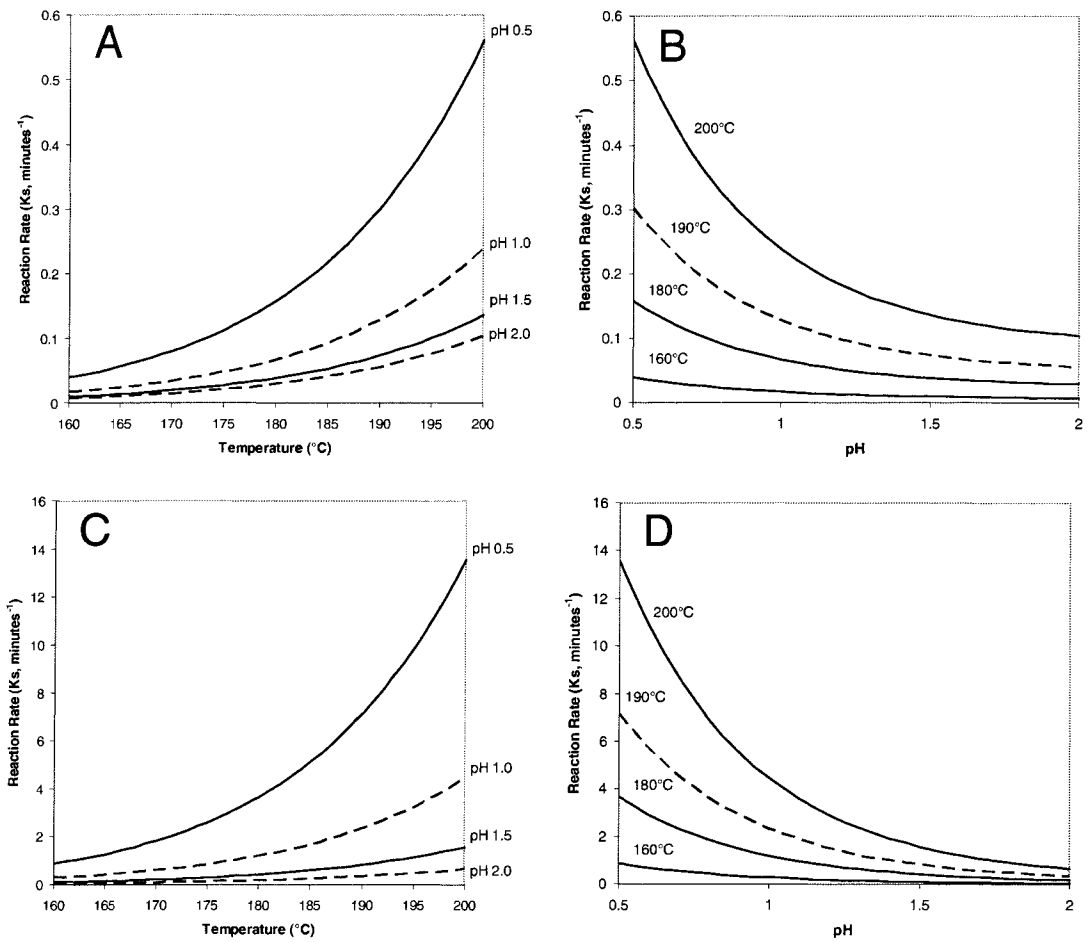

Figure 4.11: Dependence of glucose and fructose degradation kinetic rate constant on pH and temperature. A) The kinetic rate constant for glucose degradation as a function of temperature. B) The kinetic rate constant for glucose degradation as a function of pH. C) The kinetic rate constant for fructose degradation as a function of temperature. D) The kinetic rate constant for fructose degradation as a function of pH.

different on each side of the threshold. Figure 4.11 graphically shows the results of the degradation rate constant contour mapping.

Two features were readily apparent from the contour mapping of the system. First, the degradation rates for fructose are much larger than for glucose. The degradation rate for fructose is almost 30 times the degradation rate for glucose under the most severe pretreatment conditions. Second, both fructose and glucose have pH and temperature thresholds where the degradation kinetic rate constant starts to rapidly increase with changes in pH or temperature. In Figure 4.11A, the temperature threshold for glucose degradation is approximately 185°C. Above this temperature, the degradation rate constant rapidly increases. Below the threshold temperature, changes in the temperature affect the rate constant, but not nearly as significantly as temperature changes above 185°C. In Figure 4.11B, the pH threshold for glucose degradation is approximately 1.25. Below this pH, the degradation rate constant rapidly increases. Above the threshold pH, changes in the pH do not affect the rate constant to the same extent.

Fructose degradation rate constants showed similar thresholds for temperature and pH. Figure 4.11C shows the temperature dependence of the fructose degradation kinetic rate constant. The threshold temperature for fructose was approximately 180°C, lower than the glucose threshold temperature of 185°C. The threshold pH for fructose degradation was also lower than for glucose. The threshold pH for fructose is approximately 1.0. The data appears to indicate that fructose degradation under pretreatment conditions was

more sensitive to temperature increases and less sensitive to decreases in pH than glucose degradation was. For both glucose and fructose, the maximum degradation rate constants occur at the lowest pH and highest temperature in the experimental reaction space.

4.4.9 Fructose and Glucose Degradation Products

The sucrose hydrolysis and degradation pathway has been extensively studied. Sucrose hydrolysis to fructose and glucose is an important reaction in the sugar industry (Vukov, 1965; Clarke et al., 1997) as it results in a loss of a commercial product and decreased yield. The dehydration of fructose to 5-HFM has been studied as a method to manufacture 5-HMF as a valuable chemical commercial product (Kuster and Temmink, 1977) with researchers going as far as to investigate exotic catalysts such as H-mordenites to improve the yield (Moreau et al., 1996). Glucose has a similar degradation pathway to 5-HMF. Glucose degradation under dilute-acid biomass pretreatment conditions has been studied due to its large impact on creating ethanol and other biomass derived products from cellulose (Clarke et al., 1997; Mosier et al., 2002; Xiang et al., 2004; Qian et al., 2005a; Qian et al., 2005b). Severe pretreatment conditions prepare cellulose for saccrification but also degrade the glucose and other sugars liberated from the cellulose. The 5-HMF further degrades under pretreatment conditions through a hydrolysis reaction for equimolar formic acid and levulinic acid (Kuster and Temmink, 1977; Mosier et al., 2002).

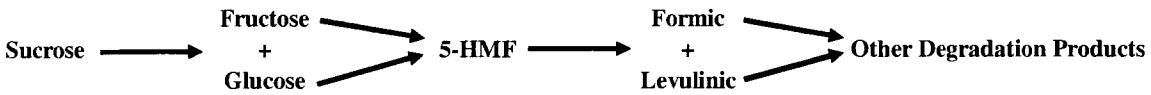

Figure 4.12: Proposed hydrolysis and degradation pathway for sucrose investigated in this work.

The hydrolysis and degradation pathway outlined in Figure 4.12 for sucrose under the low pH and high temperatures utilized for corn stover pretreatment is the simplest of the models and was evaluated in this work. Much more complex pathways have been identified for clean aqueous solutions and for solutions containing lignocellulosic biomass have been investigated but were outside the scope of this research (Clarke et al., 1997; Xiang et al., 2004; Qian et al., 2005a; Qian et al., 2005b). Degradation pathways for fructose and glucose under different temperature and pH conditions (such as low temperature or neutral or basic pH) are much different than under acidic conditions (Clarke et al., 1997; Kabyemela et al., 1999).

The applicability of the hydrolysis and degradation model presented in Figure 4.12 to the experimental data collected was evaluated using a total carbon mass balance. The total number of carbon atoms in the initial sucrose before pretreatment conditions was compared to the total number of carbon atoms in the glucose, fructose, 5-HMF, formic acid, and levulinic acid in the post-pretreatment samples. The total carbon balance results are shown in Figure 4.13. The carbon mass balance closed (all carbon atoms accounted for) when the normalized total carbon value was 1.0. In general, greater than 85% of the carbon was accounted for in the lower severity conditions (high pH, low temperature, short reaction time). As the conditions become more severe, less of the carbon is accounted for. Under the most extreme conditions tested, only 60% of the initial carbon can be accounted for in the final samples. A total normalize carbon balance of less than one indicated either the formation of additional degradation products not measured or inaccuracies in the analytical methods. The post-pretreatment samples for

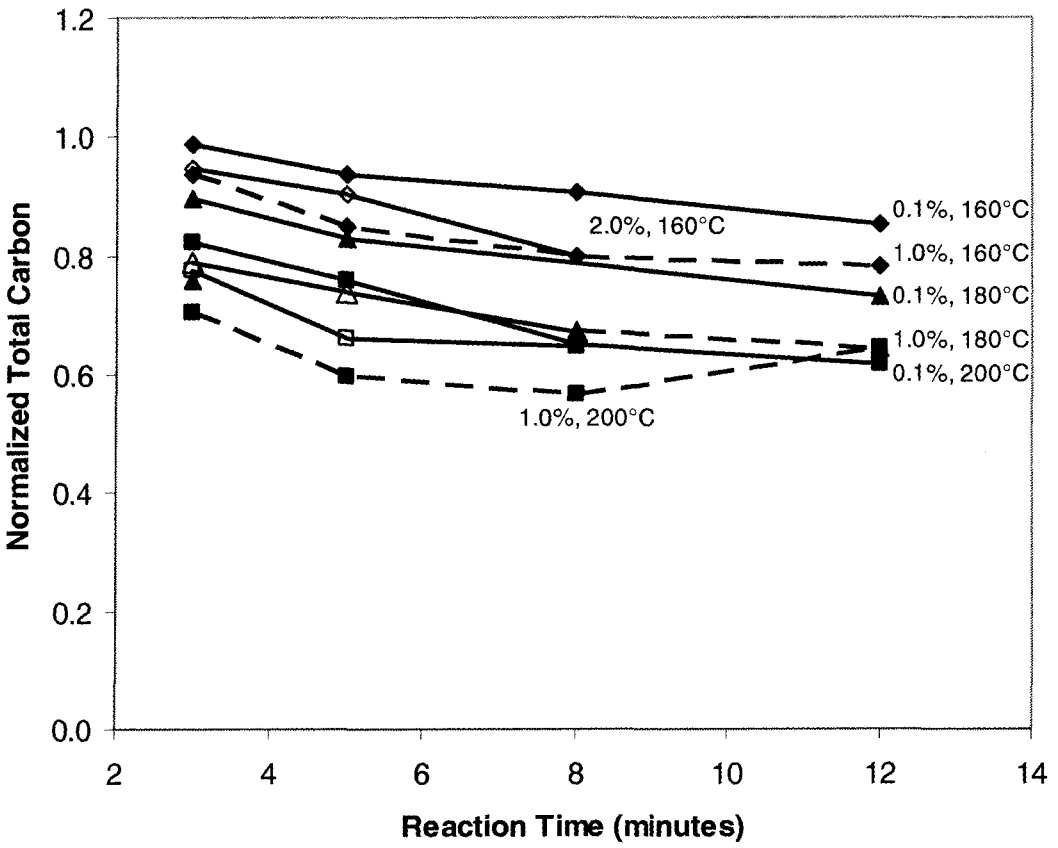

Figure 4.13: Total carbon balance around initial sucrose in pretreatment samples. Sucrose, fructose, glucose, 5-HMF, formic acid, and levulinic acid concentrations were measured in the samples after pretreatment conditions and the total carbon atoms were summed and normalized using the initial number of carbon atoms in the initial sucrose samples. The total carbon balance is less than one indicating either the formation of additional degradation products or inaccuracies in the analytical methods.

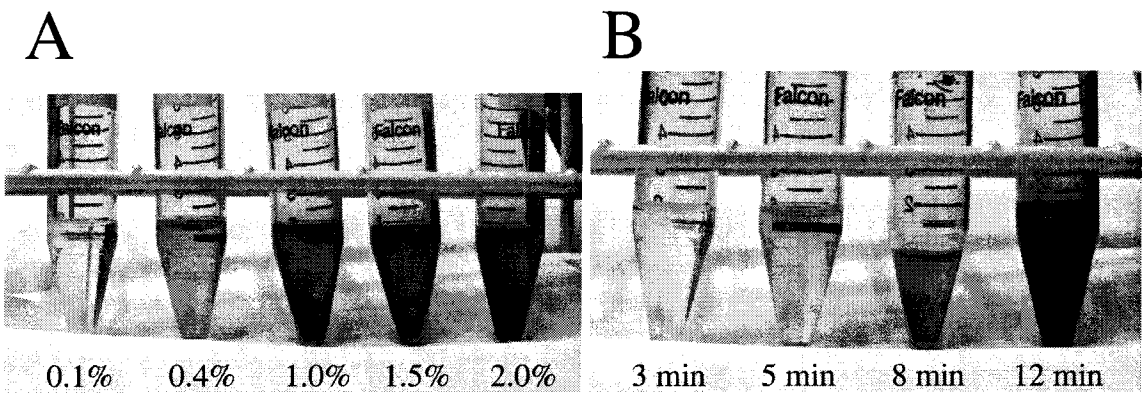

Figure 4.14: Color change and solid precipitates in pretreatment samples. A) The color change and solid formation increases with a decrease in pH. The samples are labeled according to sulfuric acid concentration %(w/w). The samples were all subjected to pretreatment conditions of 180°C for 5 minutes. B) The color change and solid formation increases as reaction time increases. The samples are labeled by nominal reaction time. The 3 minute sample had no color change or solid precipitate. The 12 minute sample had significant color change and solid precipitate formation. All four samples contain 0.1% sulfuric acid and were pretreated at 180°C.

the more severe conditions visibly contained solid precipitate material. The precipitates were likely the result of the formation of non-cellulosic polymeric compounds or other condensation reactions (Qian et al., 2005a). The dependence of the formation of these products on temperature, pH, and reaction time is shown in Figure 4.14.

The sucrose hydrolysis and degradation pathways as defined in Figure 4.12 were not complete under the pretreatment conditions studied in this work. Trends were observed in the degradation products measured in the pretreatment samples and were used to define guidelines for future hydrolysis and degradation work.

4.4.10 Kinetic Parameters for 5-HMF Formation from Fructose and Glucose

The ODE method used to fit the fructose kinetic parameters was modified to fit the 5-HMF kinetic parameters. The method was adapted by modifying the governing relationship for 5-HMF concentrations in the solution at any given time. For the fructose ODE method, fructose concentration was assumed to be equal to the fructose concentration at the previous time step minus the fructose degradation for the current time step. The concentration of 5-HMF was treated as and unsteady state with both new 5-HMF produced through glucose and fructose degradation at each time step and 5-HMF lost through degradation. A pH dependent Arrhenius model was used for the degradation rate of 5-HMF. The generation of 5-HMF was calculated using the fructose and glucose kinetic parameters previously calculated and assuming all glucose and fructose

degradation produces 5-HMF. The 5-HMF concentrations were normalized based on initial sucrose concentrations. A ½ multiplier was applied to the glucose and fructose degradation rates to account for the difference in the basis for normalization. The ODE used for calculating 5-HMF concentrations was:

$$HMF_{n+1} = -\frac{1}{2}\frac{dG}{dt} + -\frac{1}{2}\frac{dF}{dt} - \frac{dHMF_{n+1}}{dt} \tag{4-13}$$

$$\frac{dHMF_{n+1}}{dt} = -k\exp\left(\frac{-Ea_{HMF}}{RT}\right)HMF_n \tag{4-14}$$

Kinetic rate constants and activation energy were empirically fit using a least squares analysis of the experimental 5-HMF concentration measurements and temperature profiles for each data point as for fructose. The fit parameters were then used in conjunction with the temperature profiles to predict a 5-HMF concentration for each data point. The experimental values were plotted against the fit values to determine the quality of the fit parameters. The ODE method for 5-HMF did not accurately predicted the experimental 5-HMF measurements (Figure 4.15A). The predicted (fit) 5-HMF values had a significant amount of scatter with few predicted values matching experimental values. The 5-HMF concentrations successfully predicted at high severities is due primarily to very low 5-HMF concentrations. The residuals were plotted against the severity of the individual data points (Figure 4.15B) and showed a clear relationship between the nature of the residual and the severity of the condition. At severities lower than 1.6, the method over-estimates the 5-HMF concentrations (negative residual). At severities higher than 1.6, the method under-estimated the 5-HMF concentration but was closer to the actual value.

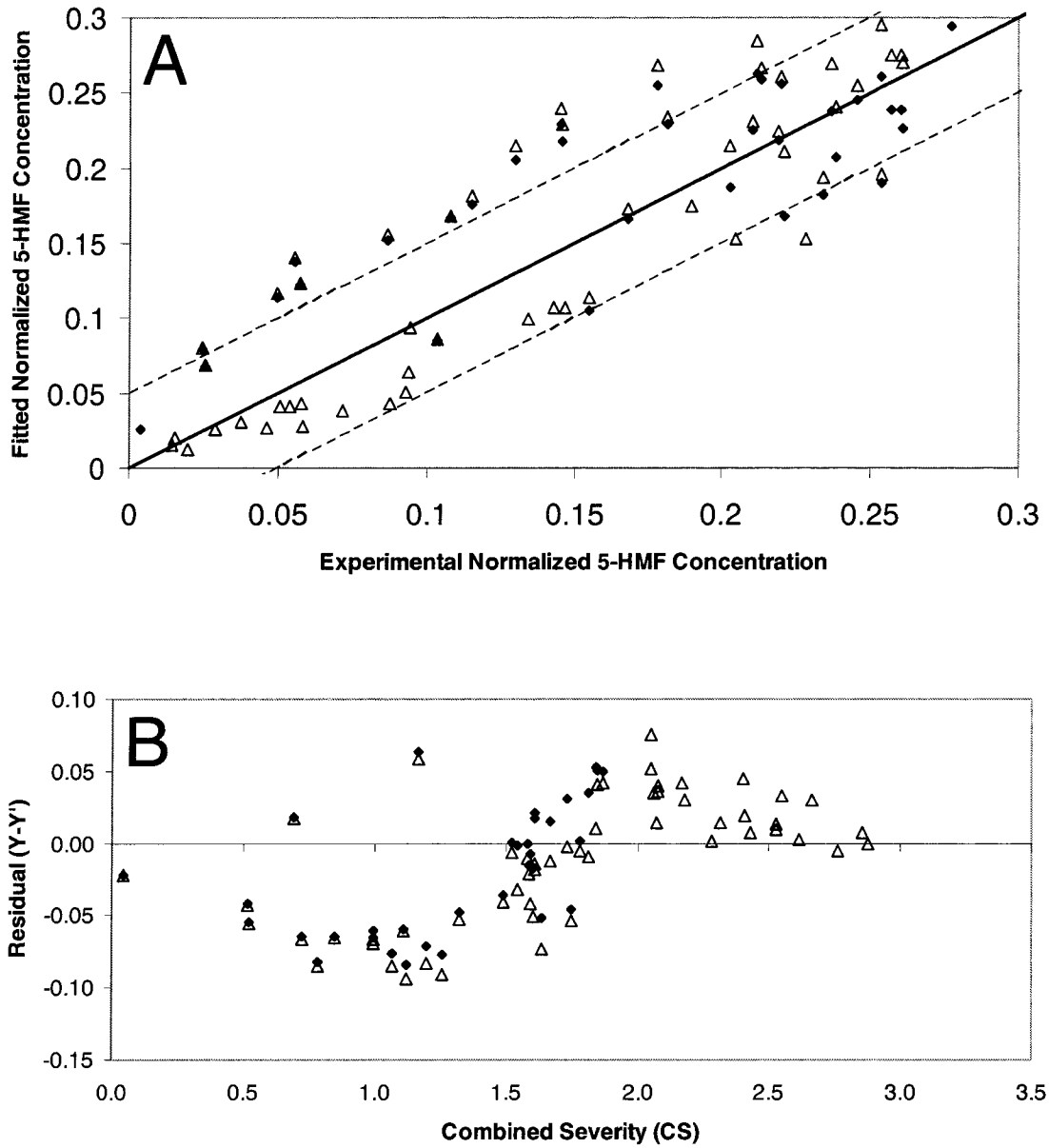

Figure 4.15: Evaluation of fitted kinetic parameters for 5-HMF formation. A) The kinetic parameters fitted for fructose and glucose degradation were used in conjunction with an Arrhenius degradation model for 5-HMF to empirically fit 5-HMF concentrations using a least squares analysis as outlined in the text. The dashed lines were equivalent to residuals of ±0.05. B.) The residuals were plotted against the combined severity of the pretreatment condition for the full data set (open triangles). A clear pattern was seen in the residuals. The data for samples with a combined severity of less than 2.0 were used for fitting the kinetic parameters (solid diamonds), but did not improve the model fit for the data.

Parameter	Value	Units
Ea	93.6	KJ/mol
$k_{0.1\%}$	8.35E+09	min^{-1}
$k_{0.4\%}$	1.94E+10	min^{-1}
$k_{1.0\%}$	4.11E+10	min^{-1}
$k_{1.5\%}$	5.64E+10	min^{-1}
$k_{2.0\%}$	6.37E+10	min^{-1}

Table 4.4: Kinetic parameters for 5-HMF degradation.

A second data set was generated consisting only of data points from reaction conditions with a severity of less than 2.0 to re-evaluate the model under the hypothesis that additional reactions pathways form under more severe conditions as determined from the total carbon balances (Figure 4.13) and visually (Figure 4.14). The modified data set did not improve the fit of the model (Figure 4.15A,B). The dependence of the pre-exponential constant, k, on pH was not evaluated due to the generally poor fit of the model. The fit kinetic parameters for 5-HMF degradation are included in Table 4.4.

4.4.11 Combined Severity Impact on Sample Composition

Plotting the degradation of solution components against the severity of the can indicate potentially critical regimes in the pretreatment conditions and the sensitivity of the components to the reaction severity. In Figure 4.16, fructose, glucose, and 5-HMF concentrations are plotted as a function of the CS. This figure clearly illustrates how glucose is more stable than fructose over the entire range of conditions tested. For treatments with a CS of 1.5, the majority of the glucose and only small fraction of fructose survives. The dependence of 5-HMF on the CS was also pronounced. As previously discussed, 5-HMF is formed by the dehydration of glucose and fructose but the 5-HMF is at the same time re-hydrated to form levulinic and formic acid under treatment conditions. Treatment at conditions with a CS below 1.0 did not degrade sufficient fructose and glucose to form significant amounts of 5-HMF. Treatment at conditions greater than 1.6 degraded all of the fructose and a significant fraction of the glucose as shown in Figure 4.16. The maximum concentration of 5-HMF (25% of the total theoretical yield) occurred at a CS of 1.6.

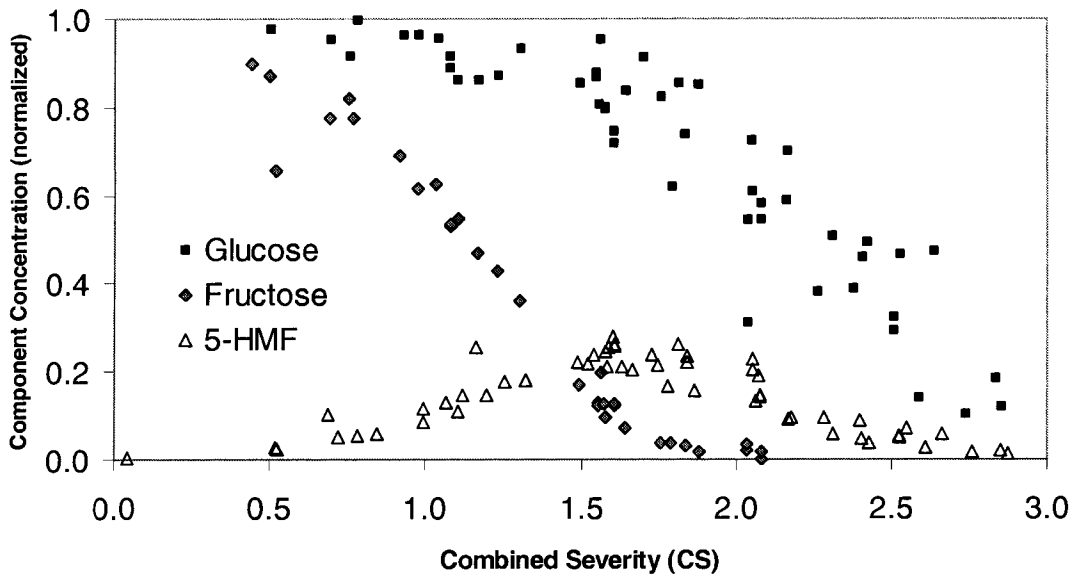

Figure 4.16: Fructose, glucose, and 5-HMF concentrations as a function of the combined severity factor (CS). All components were normalized based on initial sucrose concentrations and reaction model stoichiometry of 1 sucrose → glucose + fructose → 2 5-HMF.

The results show that dilute acid pretreatment conditions have a significant impact on the extent of recovery of sucrose-derived sugars from biomass feedstocks. At low CS (<1.0), sucrose-derived fructose and glucose survive pretreatment and are available for fermentation to ethanol, although treatment as such conditions may not be severe enough to make the biomass highly reactive to subsequent enzymatic conversion of cellulose. The mid CS region (1.0 to 2.2) produces large amounts of 5-HMF from sucrose that may inhibit fermentative microorganisms (Delgenes et al., 1996; Larsson et al., 1999). At high CS (>2.2), the majority of the sucrose-derived fructose and glucose are degraded, but 5-HMF concentrations are also reduced. Treatment at higher CS tends to increase the digestibility of the cellulose remaining in the treated material (Schell et al., 2003).

The relative degradation rates of glucose, fructose, and 5-HMF can be hypothesized based on Figure 4.16. First, fructose was almost completely degraded by reactions with a 1.6 severity. The concentration of 5-HMF increased as fructose degraded. The increase in 5-HMF concentration did not account for all of the loss of fructose, only half of the loss of fructose. Full fructose degradation to 5-HMF would result in a normalized 5-HMF concentration of 0.5 without any glucose degradation. Very little glucose degrades in severity 1.6 reactions. From this observation, either an additional degradation pathway accounted for half of the fructose degradation or 5-HMF degraded at half the rate of fructose. Second, after the fructose completely degraded (CS>1.6), the concentrations of 5-HMF started to decrease as severity increased. If all of the glucose was degrading to 5-HMF, then the rate of degradation of the 5-HMF was greater than or equal to that of

glucose under these conditions. The slope of the decrease in 5-HMF concentrations appeared to be the same as the slope of the glucose degradation. Both concentrations started at maximums around severity 1.6 and full disappear at severity of 3.0. The degradation rate of 5-HMF appeared to be approximately the same as the degradation rate of glucose and slower than that of fructose.

As expected, the formation of formic acid and levulinic acid increased as the severity factor increased. At a severity of 1.6, very little formic acid and levulinic acid formed. If the 5-HMF was degrading as fructose degraded to account for the difference between 5-HMF and fructose concentrations, formic and levulinic concentrations would have been approximately 0.25. For some conditions, approximately 0.25 normalize formic acid concentrations were present. Most formic acid concentrations were too low, however, to account for sufficient 5-HMF concentrations. This observation, along with the carbon balance outlined in Figure 4.13 supports the hypothesis that additional degradation pathways account for a significant carbon loss under dilute acid pretreatment conditions as determined theoretically (Qian et al., 2005a; Qian et al., 2005b) and analytically (Kuster and Temmink, 1977; Clark, 1997; Xiang, 2004).

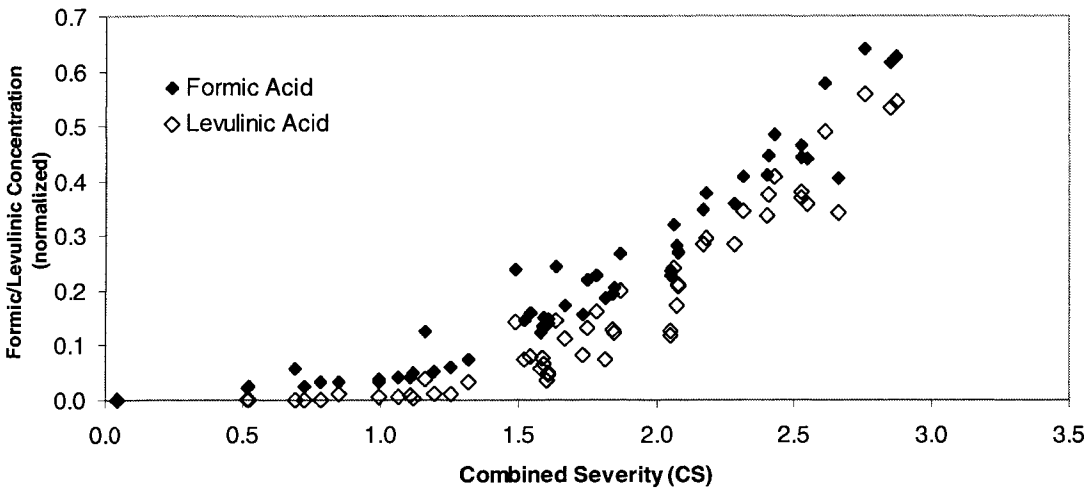

Figure 4.17: Experimental formic acid and levulinic acid concentrations after pretreatment conditions. The 5-HMF degradation products increase as the combined severity of the sample increases past as CS of 1.6 (the maximum 5-HMF concentration).

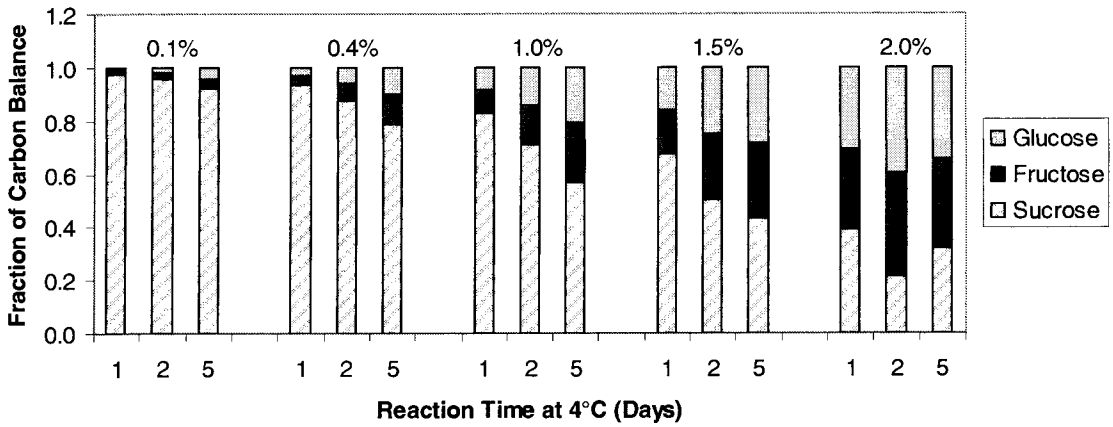

Figure 4.18: Hydrolysis of sucrose under refrigerated conditions (4 °C).

4.4.12 Sucrose Degradation Under Refrigerated Conditions

The sucrose stock solutions containing 0.1 to 2.0 %(w/w) sulfuric acid degraded over time even when stored at 4 °C. At the higher sulfuric acid concentrations studied, the hydrolysis of sucrose to fructose and glucose occurred quickly (Figure 4.18). The carbon balance closed for each sample. Closure of the carbon balance indicated that the sucrose was hydrolyzing to fructose and glucose but that the fructose and glucose were not further degrading. Since sucrose was assumed to completely hydrolyze during the heat-up of the hastelloy bombs to reaction temperature, the kinetic parameters presented in this work are not believed to be impacted by the hydrolysis of the sucrose stock solutions. All stock sucrose solutions were used within 48 hours of preparation.

4.5 Conclusions

At the treatment conditions used in this study, which are similar to those used for dilute sulfuric acid pretreatment of lignocellulosic biomass to increase its enzymatic digestibility, sucrose is rapidly hydrolyzed to fructose and glucose. No sucrose remained in solution even at the least severe reaction condition investigated (160°C, 0.1% (w/w) acid, 3 min reaction time). However, varying amounts of fructose and glucose remained after treatment, with measured concentrations ranging from near the theoretical maximums that could be derived from sucrose when treated at low severity conditions to nearly zero for treatment at the most severe condition (200°C, 2.0% acid, 8 min reaction time). Fructose exhibited much faster degradation kinetics than glucose. Due of the large differences reaction rates, different methods were needed to accurately determine kinetic parameters for fructose and glucose degradation. The ODE method was used to calculate

kinetic parameters for fructose degradation, whereas multivariable linear regression was sufficient to determine glucose degradation kinetic parameters. The rates of both fructose and glucose degradation are well modeled as a function of both solvent effects and acid concentration.

Degradation pathways for a significant percentage of the fructose and glucose are likely to contain intermediates other than 5-HMF. The total carbon balance and relative fructose and glucose concentrations do not match measured 5-HMF, formic acid, and levulinic acid concentrations. It is believed that the fructose and glucose polymerize in one or more degradation pathways to form the solid precipitate observed in higher CS pretreatment conditions.

Although it is known that agricultural and herbaceous feedstocks contain sucrose, prior to this study we had assumed that none of the sucrose-derived sugars survived dilute acid pretreatment. The fact that a significant amount of glucose and at some conditions fructose survive suggests that improving sucrose recoveries offers a strategy to increase sugar yields during pretreatment. In particular, less severe pretreatment conditions could be chosen that preserve more of these sugars. While such conditions would likely also leave more unconverted hemicellulose, the optimal treatment condition would depend on the amount of sucrose present in the raw feedstock in relation to the amount of hemicellulosic and cellulosic sugars that could subsequently be recovered by enzymatic hydrolysis. Implementation of single pass harvesting technology for agricultural crops might enable a larger amount of the sucrose to be obtained in these types of cellulosic

materials at the time of harvest. A more immediate use of these results is to understand how much glucose present in dilute acid hydrolysate is derived from sucrose versus that derived from cellulose, which is necessary to improve cellulose mass balance closure calculations for a dilute acid pretreatment process.

Chapter 5

CONCLUSIONS, COMMENTS, AND FUTURE WORK

5.1 Novel contributions to scientific literature

The novel concepts presented in this work are not new scientific apparatus, ground-breaking new fields of research, or uncovering deeper mechanisms of life. The novel concepts presented in this work are creative ideas and approaches that improve the way existing concepts are described in engineering terms. The removal of the system time-lag from the membrane chromatography breakthrough data without assuming the underlying mechanisms of the solute-membrane interactions or flow distributions has broad applications. Other researchers have applied time delays to frontal analysis methods to better describe experimental data, but doing so required extensive assumptions to be made about the mechanistic interactions between the solute and the membrane. The methodology outlined in Chapter 2 obviates this requirement and is applicable to a wide range of new investigations where the underlying mechanisms are not known. As shown in Chapter 3, fitting the discrete pore size distribution to a continuous log-normal distribution based on normalized flow improves flux calculations for ultrafiltration applications by better representing the larger, flow dominating, pores in the fitted

distribution. As described in Chapter 4, the manipulation of the Arrhenius equation to compensate for changes in the reactor temperature during a batch "isothermal" experiment significantly improved the quality of the fit parameters calculated from a well known linearization method used extensively in literature. The sucrose work also demonstrated the application of an ordinary differential equation to fit a complex and diverse data set. All four approaches were creative applications of new solutions to existing concepts that improve the engineering description of the physical system.

5.2 Membrane chromatography and system time-lag

All membrane chromatography systems contain time lags that are attributable to the tubing, membrane holder, and peripheral equipment. For small membrane chromatography systems, these time lags can significantly impact the observed break-through curve. As discussed in Chapter 2, these time lags can be removed by analyzing the membrane washing step in the chromatography cycle and applying a numerical method to remove the zero and first order time delays. Removing the system time lag also allowed for accurate scale-up of the 5 cm^2 membrane holder to the 100 cm^2 membrane module in the case study. Future application of this work will most likely be in the investigation of small custom membranes. Membrane chromatography systems currently lend themselves to scale-up from the 100 cm^2 column size to lab bench and commercial scales. A reliable method to bridge the scale-up of the 5 cm^2 to the 100 cm^2 membrane module will allow researchers to investigate much smaller membrane systems with confidence that the results can be scaled-up.

5.3 Ultrafiltration modeling

The determination of discrete surface pore size distribution by SEM and fitting a continuous log-normal distribution to the normalized flow data calculated from the discrete distribution accurately described the flux through the membrane. The next step in this area of research is to develop methods to more accurately describe the pore size distribution within the bulk 3-dimensional membrane. Microfiltration membranes have been impregnated in resin and a microtome used to section the membrane into 20 μm thick sections (Nakao, 1994). This method is applicable to ultrafiltration membranes if the technological hurdle of flowing the resin into the internal pores of the membrane can be overcome. A second method is the use of electron spin resonance (ESR) or nuclear magnetic spin resonance (NMR) to observe mobile probes within the pores themselves. The goal of such research would be to construct a 3-dimensional model of the ultrafiltration membrane with the intent of improving the rejection profile calculations.

5.4 Sucrose hydrolysis and degradation kinetics

The mathematical methods and models developed to fit the kinetic parameters for fructose and glucose degradation are superior to typical methods when applied to hastelloy bombs and sand bath systems such as were used in this work. The methodology provides a framework for continued research into the fate of sucrose-derived fructose and glucose under cellulosic biomass pretreatment conditions. The next step in this research is to spike biomass samples with known amounts of sucrose and subject the samples to pretreatment conditions. Ideally, the initial conditions would be selected such that

fructose would be expected to survive. Measuring the final concentrations of glucose, fructose, xylose, and other degradation and feed products would allow the pure-sucrose kinetic models to be validated or revised under actual pretreatment conditions. The kinetic studies performed in this work used "ideal" sucrose solutions containing only sucrose, sulfuric acid, and water. Trace constituents of the biomass may affect the degradation kinetics or pathways through side reactions. Ash may neutralize the pretreatment acid, and acetic acid may exacerbate the degradation. Cellulose may interact with intermediate degradation products and increase or decrease the solid precipitants observed in this work. These additional effects caused by the biomass need to be quantified in order for the sucrose degradation kinetics to be meaningful for commercial applications and for more accurate carbon mass balance measurements for improved computational data.

From here, the research could branch in two directions. First, hastelloy bombs are not a completely accurate model system for the pilot plant. Additional equipment and methodology should be explored to better model the steam injection system used in the continuous pilot scale process. The significant differences between the bomb and the steam injected pilot scale pretreatment reactor system include: constant volume in the bomb vs. constant pressure in the steam injection reactor, batch operation of the bomb vs. continuous operation of the steam injection reactor, and clean solution in the bomb (as tested to date) vs. biomass pellets in the injector. The pellet effects are primarily diffusion limitations associated with the acid penetrating the biomass pellets. Second, attempts should be made to combine the models for sucrose, cellulose, and hemi-

cellulose (xylose) hydrolysis for pretreatment and subsequent sugar cofermentation to optimize the overall yield of ethanol (based on the original mass of biomass). A combined model might reveal operational parameters for pretreatment (temperature, pH, reaction time) and cofermentation (temperature, pH, fermentation time, enzyme loading) that warrant further investigation and more insight into the interdependence of these processing steps.

REFERENCES

Agblevor, F.A.; Murden, A.; Hames, B.R.; *Improved method of analysis of biomass sugars using high-performance liquid chromatography.* **Biotechnolgy Letters**, 26:1207-1210, 2004.

Armstrong, J.K.; Wenby, R.B.; Meiselman, H.J.; Fisher, T.C.; *The hydrodynamic radii of macromolecules and their effect on red blood cell aggregation.* **Biophysical Journal**, 87:4259-4270, 2004.

Baltus, R.E.; *Characterization of the pore area distribution in porous membranes using transport measurements.* **Journal of Membrane Science**, 123:165-184, 1997a.

Baltus, R.E.; *The use of moment theory to interpret diffusion and sieving measurements in terms of the pore size distribution in heteroporous membranes.* **Journal of Membrane Science**, 130:157-172, 1997b.

Baltus, R.E.; *Characterization of gel-filled porous membranes using moment-based interpretation of transport measurements.* **Journal of Membrane Science**, Article in Press.

Bhattacharya, S.; Hwang, S-T; *Concentration polarization, separation factor, and Peclet number in membrane processes.* **Journal of Membrane Science**, 132:73-90, 1997.

Bungay, P.M.; Brenner, H.; *The motion of a closely-fitting sphere in a fluid-filled tube.* **International Journal of Multiphase Flow**, 1:25-56, 1973.

Calvo, J.I.; Pradanos, P.; Hernandez, A.; Bowen, W.R.; Hilal, N.; Lovitt, R.W.; Williams, P.M.; *Bulk and surface characterization of composite UF membranes atomic force microscopy, gas adsorption-desorption and liquid displacement techniques.* **Journal of Membrane Science**, 128:7-21, 1997.

Charcosset, C.; Su, Z.; Karoor, S.; Daun, G.; Colton, C.K.; *Protein A immunoaffinity hollow fiber membranes for immunoglobulin G purification: experimental characterization.* **Biotechnology and Bioengineering**, 48:415-427, 1995.

Charcosset, C.; *Purification of proteins by membrane chromatography.* **Journal of Chemical Technology and Biotechnology**. 71:95-110, 1998.

Clarke, M.A.; Edye, L.A.; Eggleston, G.; *Sucrose decomposition in aqueous solution and losses in sugar manufacture and refining.* **Advances in Carbohydrate Chemistry and Biochemistry**, 52:441-470, 1997.

Deen, W.M.; *Hindered transport of large molecules in liquid-filled pores.* **AIChE Journal**, 33:1409-1423, 1987.

Derjani-Bayeh, S.; Rodgers, V.G.J.; *Sieving variations due to the choice in pore size distribution model.* **Journal of Membrane Science**, 209:1-17, 2002.

Dietz, P.; Hansma, P.K.; Inacker, O.; Lehmann, H.-D.; Herrmann, K.-H.; *Surface pore structures of micro-and ultrafiltration membranes imaged with the atomic force microscope.* **Journal of Membrane Science**, 65:101-111, 1992.

Farrell, A.E.; Plevin, R.J.; Turner, B.T.; Jones, A.D.; O'Hare, M.; Kammen, D.M.; *Ethanol can contribute to energy and environmental goals.* **Science**, 311:506-508, 2006.

Gadam, S.; Phillips, M.; Orlando, S.; Kuriyel, R.; Pearl, S.; Zydney, A.; *A liquid porosimetry technique for correlating intrinsic protein sieving: Applications in ultrafiltration processes.* **Journal of Membrane Science**, 133:111-125, 1997.

Gebauer, K.H.; Thommes, J.; Kula, M.R.; *Breakthrough performance of high-capacity membrane adsorbers in protein chromatography.* **Chemical Engineering Science**, 52:405-419, 1997.

Germic, L.; Ebert, K.; Bouma, R.H.B.; Borneman, Z.; Mulder, M.H.V.; Strathmann, H.; *Characterization of polyacrylonitrile ultrafiltration membranes.* **Journal of Membrane Science**, 132:131-145, 1997.

Ghosh, R.; *Bioseparation using supported liquid membrane chromatography.* **Journal of Membrane Science**, 192:243-247, 2001.

Ghosh, R.; *Protein separation using membrane chromatography: opportunities and challenges.* **Journal of Chromatography A**, 952:13-27, 2002.

Giovannini, R.; Freitag, R.; Tennikova, T.; *High-Performance Membrane Chromatography of Supercoiled Plasmid DNA.* **Analytical Chemistry**, 70:3348-3354, 1998.

Gumi, T.; Valiente, M.; Khulbe, K.C.; Palet, C.; Matsuura, T.; *Characterization of activated composite membranes by solute transport, contact angle measurement, AFM and ESR.* **Journal of Membrane Science**, 212:123-134, 2003.

Guo, W.; Ruckenstein, E.; *A new matrix for membrane affinity chromatography and its application to the purification of concanavalin A.* **Journal of Membrane Science**, 182:227-234, 2001.

Guo, W.; Ruckenstein, E.; *Crosslinked mercerized cellulose membranes for the affinity chromatography of papain inhibitors.* **Journal of Membrane Science**, 197:53-62, 2002.

Hagedorn, J.; Kasper, C.; Freitag, R.; Tennikova, T.; *High performance flow injection analysis of recombinant Protein G.* **Journal of Biotechnology**, 69:1-7, 1999.

Han, B.; Carvalho, W.; Canilha, L.; da Silva, S.S., Almeida e Silava J. B.; McMillan, J. D., Wickramasinghe, S. R.; *Adsorptive membranes vs. resins for acetic acid removal from biomass hydrolysates.* **Desalination**, 18x:000-000, 200x.

Hao, W.; Wang, J.; Li, J.; *Modeling, by frontal analysis, of the adsorption of bovine serum albumin on cibacron blue-modified cellulose membranes.* **Chromatographia**, 60:449-454, 2004.

Haralampu, S.G.; Saguy, I.; Karel, M.; *Estimation of Arrhenius model parameters using three least squares methods.* **Journal of Food Processing and Preservation**, 9:129-143, 1985.

Herak, D.C.; Merrill, E.W.; *Affinity Cross-Flow Filtration: Some New Aspects.* **Biotechnology Progress**, 6:33-40, 1990.

Hernandez, A.; Calvo, J.I.; Pradanos, P.; Tejerina, F.; *Pore size distributions of track-etched membranes; comparison of surface and bulk porosities.* **Colloids and Surfaces A: Physicochemical and Engineering Aspects**, 138:391-401, 1998.

Kabyemela, B.M.; Adschiri, T.; Malaluan, R.M.; Arai, K.; *Glucose and fructose decomposition in subcritical and supercritical water: Detailed reaction pathway, mechanisms, and kinetics.* **Industrial and Engineering Chemistry Research**, 38:2888-2895, 1999.

Khayet, M.; Matsuura, T.; *Determination of surface and bulk pore sizes of flat-sheet and hollow-fiber membranes by atomic force microscopy, gas permeation and solute transport methods.* **Desalination**, 158:57-64, 2003.

Khayet, M.; Khulbe, K.C.; Matsuura, T.; *Characterization of membranes for membrane distillation by atomic force microscopy and estimation of their water vapor transfer coefficients in vacuum membrane distillation process.* **Journal of Membrane Science**, 238:199-211, 2004.

Khulbe, K.C.; Matsuura, T.; *Characterization of synthetic membranes by Raman spectroscopy, electron spin resonance, and atomic force microscopy; a review.* **Polymer**, 41:1917-1935, 2000.

Kim, M.; Saito, K.; Furusaki, S.; Sato, T.; Sugo, T.; Ishigaki, I; *Adsorption and elution of bovine γ-globulin using an affinity membrane containing hydrophobic amino acids as ligands.* **Journal of Chromatography**, 585:45-51, 1991.

Kinniburgh, D. G.; General purpose adsorption isotherms. Environmental Science and Technology, 20:895-904, 1986

Kiyohara, S.; Sasaki, M.; Saito, K.; Sugita, K.; Sugo, T.; *Amino acid addition to epoxy-group-containing polymer chain grafted onto a porous membrane.* **Journal of Membrane Science**, 109:87-92, 1996.

Klein, E.; *Affinity membranes: a 10-year review.* **Journal of Membrane Science**, 179:1-27, 2000.

Kochan, J.E.; Wu, Y.-J.; Etzel, M.R.; *Purification of bovine immunoglobulin G via protein G affinity membranes.* **Industrial & Engineering Chemical Research**, 35:1150-1155, 1996.

Kubota, N.; Miura, S.; Saito, K.; Sugita, K.; Watanabe, K.; Sugo, T.; *Comparison of protein adsorption by anion-exchange interaction onto porous hollow-fiver membrane and gel bead-packed bed.* **Journal of Membrane Science**, 117:135-142, 1996.

Kubota, N.; Kounosu, M. Saito, K.; Sugita, K.; *Protein adsorption and elution performances of porous hollow-fiber membranes containing various hydrophobic ligands.* **Biotechnology Progress**, 13:89-95, 1997a.

Kubota, N.; Kounosu, M.; Saito, K.; Sugita, K.; Watanabe, K.; Sugo, T.; *Repeated use of a hydrophobic ligand-containing porous membrane for protein recovery.* **Journal of Membrane Science**, 134:67-73, 1997b.

Kubota, N.; Konno, Y. Saito, K.; Sugita, K.; Watanabe, K.; Sugo, T.; *Module perfomance of anion-exchange porous hollow-fiber membranes for high-speed protein recovery.* **Journal of Chromatography A**, 782:159-165, 1997c.

Kuster, F.M.; Temmink, H.M.G.; *The influence of pH and weak-acid anions on the dehydration of D-fructose.* **Carbohydrate Research**, 54:185-191, 1977.

Lee, S.; Park, G.; Amy, G.; Hong, S-K; Moon, S-H; Lee, D-H; Cho, J.; *Determination of membrane pore size distribution using the fractional rejection of nonionic and charged macromolecules.* **Journal of Membrane Science**, 201:191-201, 2002.

Li, Y.; Cooper, J.; Lee, C.S.; *Miniaturized membrane-based reversed-phase chromatography and enzyme reactor for protein digestion, peptide deparation, and protein identification using electrospray ionization mass spectrometry.* **Journal of Chromatography A**, 979:241-247, 2002.

Lin, S.Y.; Suen, S.Y. *Protein separation using plate-and-frame modules with ion-exchange membranes.* **Journal of Membrane Science**, 204:37-51, 2002.

Lode, F.G.; Rosenfeld, A.; Yuan, Q.S.; Root, T.W.; Lightfoot, E.N.; *Refining the scale-up of chromatographic separations.* **Journal of Chromatography A**. 796:3-14, 1998.

Longhinotti, E.; Pozza, F.; Furlan, L.; Sanchez, M. de N. de M.; Klug, M.; Laranjeira, M. C.M.; Favere, V. T.; *Adsorption of anionic dyes on the biopolymer chitin.* **Journal of Brazilian Chemical Society**. 9:435-440, 1998.

Luksa, J.; Menart, V.; Milicic, S.; Kus, B.; *Purification of human tumour necrosis factor by membrane chromatography.* **Journal of Chromatography A**, 661:161-168, 1994.

Lutkemeyer, D.; Bretschneider, M.; Buntemeyer, H.; Lehmann, J.; *Membrane chromatography for rapid purification of recombinant antithrombin III and monoclonal antibodies from cell culture supernatant.* **Journal of Chromatography**, 639:57-66, 1993.

Miloshevich, L. M.; Paukkunen, A.; Vomel, H.; Oltmans, S. J.; *Development and validation of a time-lag correction for vaisala radiosonde humidity measurements.* **Journal of atmospheric and oceanic technology**. 21:1305-1327, 2004.

Mochizuki, S.; Zydney, A.; *Theoretical analysis of pore size distribution effects on membrane transport.* **Journal of Membrane Science**, 82:211-227, 1993.

Moreau, C.; Durand, R.; Razigade, S.; Duhamet, J.; Faugeras, P.; Rivalier, P.; Ros, P.; Avignon, G.; *Dehydration of fructose to 5-hydroxymethylfurfural over H-mordenites.* **Applied Catalysis A: General**, 145:211-224, 1996.

Moscariello, J.; Purdom, G.; Coffman, J.; Root, T.W.; Lightfoot, E.N.; *Characterizing the performance of industrial-scale columns.* **Journal of Chromatography A**, 908:131-141, 2001.

Mosier, N.S.; Ladisch, C.M.; Ladisch, M.R.; *Characterization of acid catalytic domains for cellulose hydrolysis and glucose degradation.* **Biotechnology and Bioengineering**, 79:610-618, 2002.

Mosier, N.; Wyman, C.; Dale, B.; Elander, R.; Lee, Y.Y.; Holtzappel, M.; Ladisch, M.; *Reatures of promising technologies for pretreatment of lignocellulosic biomass.* **Bioresource Technology,** 96:673-686, 2005.

Nakao, S.; *Determination of pore size and pore size distribution. 3. Filtration membranes.* **Journal of Membrane Science**, 96:131-165, 1994.

Nguyen, Q.A.; Tucker, M.P.; Keller, F.A.; Eddy, F.P.; *Two-stage dilute acid pretreatment of softwoods,* **21st Symposium on Biotechnology for Fuels and Chemicals**, 1999.

Pradanos, P.; Rodriguez, M.L.; Calvo, J.I.; Hernandez, A.; Tejerina, F.; de Saja, J.A.; *Structural characterization of an UF membrane by gas adsorption-desorption and AFM measurements.* **Journal of Membrane Science**, 117:291-302, 1996.

Qian, X.; Nimlos M.R.; Johnson, D.K.; Himmel, M.E.; *Acidic sugar degradation pathways.* **Applied Biochemistry and Biotechnology**, 121-124:989-997, 2005a.

Qian, X.; Nimlos, M.R.; Davis, M.; Johnson, D.K.; Himmel, M.E.; *Ab initio molecular dynamics simulations of β-D-glucose and β-D-xylose degradation mechanisms in acidic aqueous solution.* **Carbohydrate Research**, 340:2319-2327, 2005b.

Ragauskas, A.J.; Williams, C.K.; Davison, B.H.; Britovsek, G.; Cairney, J.; Eckert, C.A.; Frederick, W.J. Jr.; Hallett, J.P.; Leak, D.J.; Liotta, C.L.; Mielenz, J.R.; Murphy, R.; Templer, R.; Tschaplinski, T.; *The path forward for biofuels and biomaterials.* **Science**, 311:484-489, 2006.

Ramaswarmy, S.; Greenberg, A.R.; Peterso, M.L.; *Non-invasive measurement of membrane morphology via UFDR: pore-size characterization.* **Journal of Membrane Science**, 239:143-154, 2004.

Reif, O.W.; Nier, V.; Bahr, U.; Freitag, R.; *Immobilized metal affinity membrane adsorbers as stationary phases for metal interaction protein separation.* **Journal of Chromatography A**, 664:13-25, 1994.

Roper, D.K.; Lightfoot, E.N.: *Separation of biomolecules using adsorptive membranes.* **Journal of Chromatography A**, 702:3-26, 1995a.

Roper, D.K.; Lightfoot, E.N.; *Estimating plate heights in stacked-membrane chromatography by flow reversal.* **Journal of Chromatography A**. 702:69-80, 1995b.

Sadeghi, F.; Swartzel, K.R.; *Generating kinetic data for use in design and evaluation of high temperature food processing systems.* **Journal of Food Science**, 55:851-853, 1990.

Santarelli, X; Domergue, F.; Clofent-Sanchez, G.; Dabadie, M.; Grissely, R.; Cassagne, C.; *Characterization and application of new macroporous membrane ion exchangers.* **Journal of Chromatography B**, 706:13-22, 1998.

Schell, D.J.; Farmer, J.; Newman, M.; McMillan, J.D.; Dilute-*sulfuric acid pretreatment of corn stover in pilot-scale reactors.* **Applied Biochemistry and Biotechnology**, 105-108:69-85, 2003.

Schell, D.J.; Riley, C.J.; Dowe, N.; Farmer, J.; Ibsen, K.N.; Ruth, M.F.; Toon, S.T.; Lumpkin, R.E.; *A bioethanol process development unit: initial operating experiences and results with a corn fiber feedstock.* **Bioresource Technology**, 91:179-188, 2004.

Shiosaki, A.; Goto, M.; Hirose, T.; *Frontal analysis of protein adsorption on a membrane adsorber.* **Journal of Chromatography A**, 697:1-9, 1994.

Suen, S.-Y.; Etzel, M.R.; *A mathematical analysis of affinity membrane bioseparations.* **Chemical Engineering Science**. 47:1355-1364, 1992.

Suen, S.Y.; Chang, Y.S.; *Adsorption and desorption of lysozyme and albumin to cibacron blue 3GA using gel beads and membrane discs.* **Journal of the Chinese Institute of Chemical Engineering**., 29:307-317, 1998.

Suen, S.Y.; Tsai, Y.D.; *Comparison of ligand density and protein adsorption on dye-affinity membranes using different spacer arms.* **Separation Science and Technology**, 35:69-87, 2000.

Suen, S.Y.; Chiu, H.C.; Tsai, Y.D.; *Polysaccharide-modified poly(ether sulfone) hollow fibers as solid supports for affinity adsorption: equilibrium adsorption study.* **Separation Science and Technology**, 35:1343-1362, 2000.

Swartzel, K.R.; *Arrhenius kinetics as applied to product constituent losses in ultra high temperature processing.* **Journal of Food Science**. 47:1886, 1982.

Teeters, M.A.; Root, T.W.; Lightfoot, E.N.; *Performance and scale-up of adsorptive membrane chromatography.* **Journal of Chromatography A**, 944:129-139, 2002.

Tennikova, T.B.; Bleha, M.; Svec, F.; *High-performance membrane chromatography of proteins, a novel method of protein separation.* **Journal of Chromatography**. 555:97-107, 1991.

Tennikova, T.B.; Svec, F.; *High-performance membrane chromatography: highly efficient separation method for proteins in ion-exchange, hydrophobic interaction and reversed-phase modes.* **Journal of Chromatography**, 646:279-288, 1993.

Thömmes, J.; Kula, M.-R.; *Membrane chromatography—an integrative concept in the downstream processing of proteins.* **Biotechnology Progress**, 11:357-367, 1995.

Torres, A.P.; Oliveira, F.A.R.; Silva, C.L.M.; Fortuna, S.P.; *The influence of pH on the kinetics of acid hydrolysis of sucrose.* **Journal of Food Process Engineering**, 17:191-208, 1994.

Torres, A.P.; Oliveira, F.A.R.; *Application of the acid hydrolysis of sucrose as a temperature indicator in continuous thermal processes.* **Journal of Food Engineering** 40:181-188, 1999.

Tsai, Y.D.; Suen, S.Y.; *Breakthrough curve performance using plate-and-frame affinity-membrane modules.* 40:854-861, 2001.

Vukov, K.; *Kinetic aspects of sucrose hydrolysis.* **International Sugar Journal**, 67:172-175,1965.

Wang, F.Y.; Yu, Q.; *Optimal protein separations with time lags in control functions.* **Journal of Process Controls**. 4:135-142, 1994.

Weiner, C.; Sara, M.; Dasgupta, G.; Sleytr, U.B.; *Affinity cross-flow filtration: purification of IgG with a novel protein A affinity matrix prepared from two-dimensional protein crystals.* **Biotechnology and Bioengineering**, 44:55-65, 1994.

Xiang, Q.; Lee, Y.Y.; Torget, R.W.; *Kinetics of glucose decomposition during dilute-acid hydrolysis of lignocellulosic biomass.* **Applied Biochemistry and Biotechnology**, 113-116:1127-1138, 2004

Yang, L.; Chen, P.; *Chitosan/coarse filter paper composite membrane for fast purification of IgG from human serum.* **Journal of Membrane Science**, 205:141-153, 2002.

Yuan, Q.S.; Rosenfeld, A.; Root, T.W.; Klingenberg, D.J.; Lightfoot, E.N.; *Flow distribution in chromatographic columns.* **Journal of Chromatography A**. 831:149-165, 1999.

Zeng, X.; Ruckenstein, E.; *Membrane chromatography: preparation and applications to protein separation.* **Biotechnology Progress**, 15:1003-1019, 1999.

Zhao, C.; Zhou, X.; Yue, Y.; *Determination of pore size and pore size distribution on the surface of hollow-fiber filtration membranes: a review of methods.* **Desalination**, 129:107-123, 2000.

Zydney, A.L.; Aimar, P.; Meireles, M.; Pimbley, J.M.; Belfort, G.; *Use of the log-normal probability desnsity function to analyze membrane pore size distributions: functional forms and discrepancies.* **Journal of Membrane Science**, 91:293-298, 1994.

APPENDIX A

SCHEMATICS FOR EXPERIMENTAL APPARATUS

A.1 Apparatus for Chapter 2

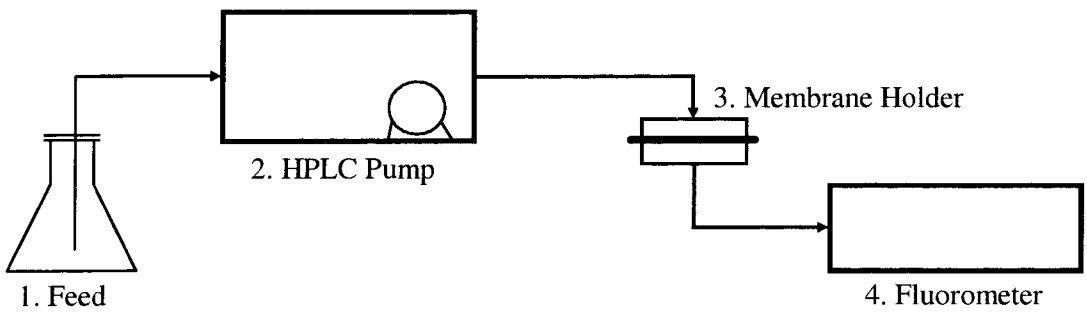

1. Feed solution (buffer, buffer and protein, or buffer with salt) in a 250 ml Erlenmeyer flask.
2. Waters 501 HPLC pump.
3. Sartorius 6 mbH D-3400 (5 cm^2) or Sartobind Q 100 (100 cm^2) membrane holder.
4. Waters 474 Scanning fluorescence detector.

A.2 Apparatus for Chapter 3

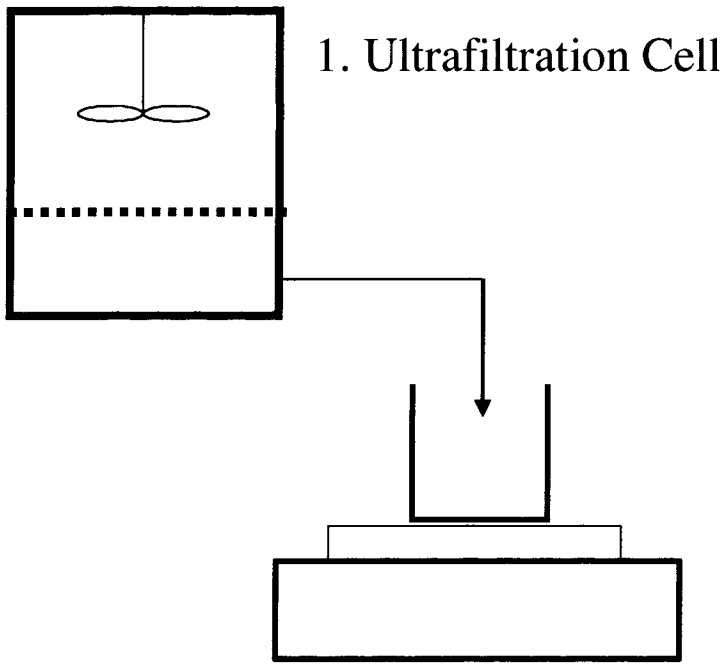

1. Millipore model 8050 stirred ultrafiltration cell.
2. Mettler Toledo scale and beaker.

A.3 Apparatus for Chapter 4

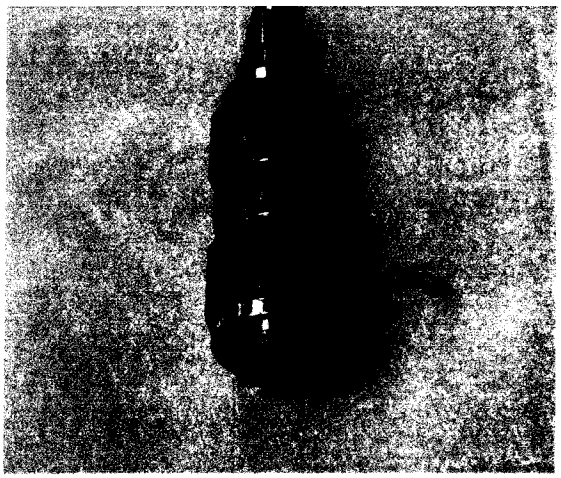

1. Hastelloy Bomb

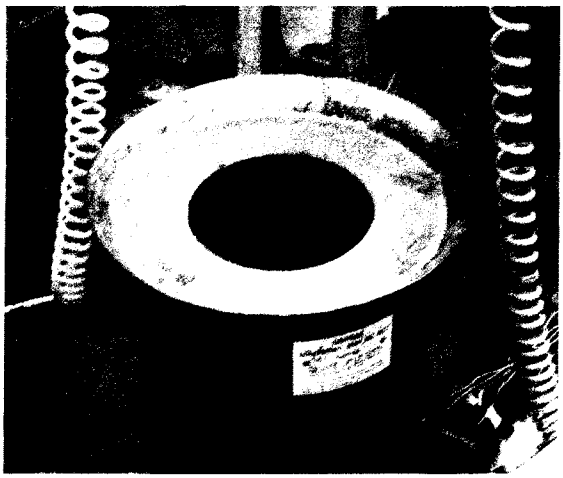

2. Sand Bath

1. Hastelloy C Swagelok ½" union and caps.
2. Techne SBL-2D fluidized sand bath.

APPENDIX B

MATLAB PROGRAMS

B.1 Remove first-order time lag and smoothing, *CurveSmoothing*

```
%Removing time delay from breakthrough curves and apply curve smoothing

clear
format short e

%Del t is the flow divided by the time increment (s) / 60 sec/min
Delt = 9.96/12;    %for 10 ml/min nominal flow rate
%Delt = 3.97/12;    %for 4 ml/min nominal flow rate
%Delt = 0.46/12;    %for 0.5 ml/min nominal flow rate
%Delt = 0.183/12;     %for 0.2 ml/min

Tau = 24;  %time for 63% range - Vcstr for 10.0 ml/min
%Tau = 26;  %time for 63% range - Vcstr for 4.0 ml/min
%Tau = 2.3;  %time for 63% range - Vcstr for 0.5 ml/min
%Tau = 1.9;    %time for 63% range - Vcstr for 0.2 ml/min

delY=0.35; %User defined tolerance value for the data smoothing
SmoothIt=50;   %User defined number of smoothing iterations

X=exp(-Delt/Tau);

%Load adjusted break through curve from text file-data with zero order time
%delay removed, 5 ml in this case
BrkRaw = load('adjbrk10mlmin.txt');

datanum = length(BrkRaw);

%Zero BrkAdj, BrkFinal
BrkFinal = zeros(datanum,1);
BrkAdj = zeros(datanum,1);

%Run numerical method to remove time delay from the data
for k = 2:datanum;
   BrkAdj(k)=(BrkRaw(k)-(BrkRaw(k-1)*X))/(1-X);
end

% Data smoothing preparation
Y = BrkAdj;
Ys = zeros(datanum,1);
```

```
Ysf = zeros(datanum,1);
Ysr = zeros(datanum,1);
Yc = zeros(datanum,1);
Yh = zeros(datanum,1);
Yl = zeros(datanum,1);

D = zeros(datanum,1);

%Start Iteration loop for smoothing
for j=1:SmoothIt

   %Fill matrices in order Y-D-Yc-Yh-Yl-Ys

   for i=3:datanum-2;
      D(i)=(Y(i+1)-Y(i))/Delt;
   end

   for i=2:datanum-3;
      Yc(i+1)=(D(i)*Delt+Y(i+2)+2*Y(i))/3;
   end

   for i=1:datanum;
      Yh(i)=Y(i)+delY;
      Yl(i)=Y(i)-delY;
   end

   for i=2:datanum-3;
      if Yc(i+1)>Yh(i+1);
         Ysf(i+1)=Yh(i+1);
      elseif Yc(i+1)<Yl(i+1);
         Ysf(i+1)=Yl(i+1);
      else Ysf(i+1)=Yc(i+1);
      end
   end

   %Calculate matrix in the reverse direction
   %Fill matrices in order Y-D-Yc-Yh-Yl-Ys
   for i=datanum-2:-1:3;
      D(i)=(Y(i-1)-Y(i))/Delt;
   end

   for i=datanum-2:-1:3;
      Yc(i-1)=(D(i)*Delt+Y(i-2)+2*Y(i))/3;
   end

   for i=datanum:-1:1;
      Yh(i)=Y(i)+delY;
      Yl(i)=Y(i)-delY;
   end

   for i=datanum-2:-1:3;
      if Yc(i-1)>Yh(i-1);
         Ysr(i-1)=Yh(i-1);
      elseif Yc(i-1)<Yl(i-1);
         Ysr(i-1)=Yl(i-1);
      else Ysr(i-1)=Yc(i-1);
```

```
    end
  end
  Ys=(Ysf+Ysr)/2; %average the Ys values for forward and reverse
  Ys(datanum-2)=1;
  Ys(datanum-1)=1;
  Ys(datanum)=1;
  Y=Ys;
end

BrkFinal=Y;
```

B.2 Estimating boundaries for pores and over-writing image, *PoreHistPrepA*

```
%Image analysis for Q membrane pore size distributions - overwrite boarders
%on image for modification by hand

clear

%Load image into an array, IM
IM=imread('500 s 50000 1.tif');

%Define the level for pore selection, used in the im2bw command
BWlevel = 0.35;

%Convert image from gray scale to black and white
BW = im2bw(IM,BWlevel);

%Invert the image for analysis, done by using the '~' prefix
InvertBW = (~BW);

[L,num] = bwlabel(InvertBW);

%Plot IM
figure
imshow(IM)

%Plot BW image
%figure
%imshow(BW)

%Determine boundaries
[B,L2] = bwboundaries(InvertBW,'noholes');

%Plot IM with boundaries
h = figure
imshow(IM)
hold on
for k = 1:length(B)
  boundary = B{k};
  plot(boundary(:,2), boundary(:,1), 'g', 'LineWidth', 2)
end

ModIM = IM;       %For overwriting border onto the original image
```

```
%ModIM = zeros(1024,1280);      %For creating a "trace" of the boundaries

for j = 1:length(B)
  Border = B{j};
  for s = 1:length(Border)
     ModIM(Border(s,1),Border(s,2)) = 0;
  end
  clear Border;
end
%InvertModIM = (~ModIM);

figure
imshow(ModIM)
%imshow(InvertModIM)

imwrite(ModIM,'500-s-1m.bmp');
%imwrite(InvertModIM,'mod-6-1-800bw.bmp');
```

B.3 Defining boundaries of pores, *PoreHistPrepB*

```
%Image analysis for Q membrane pore size distributions - convert
%hand-modified images to black and white

clear

%Load image into an array, IM
IM=imread('500-s-1mc.bmp');

%Define the level for pore selection, used in the im2bw command
BWlevel = 0.05;

%Convert image from gray scale to black and white
BW = im2bw(IM,BWlevel);

%Plot IM
figure
imshow(IM)

%Plow black and white
figure
imshow(BW)

imwrite(BW,'500-s-1mf.bmp');
```

B.4 Prepare final black and white image, *PoreHistPrepC*

```
%Image analysis for Q membrane pore size distributions - convert
%hand-modified images to black and white

clear

%Load image into an array, IM
IM=imread('500-s-1mf.bmp');

BW = IM;
[m,n]= size(BW);

for i=1:m;
   for j=1:n;
      if BW(i,j)>250;
         BW(i,j)=0;
      elseif BW(i,j)<3;
         BW(i,j)=0;
      else
         BW(i,j)=255;
      end
   end
end

%Plot IM
figure
imshow(IM)

%Show black and white
figure
imshow(BW)

imwrite(BW,'500-s-1mf.bmp');
```

B.5 Generate histogram, *PoreHistBatch*

```
%Image analysis for ca membrane pore size distributions

clear
format short e

%Define pixel area and width for pore area and diameter calculations
PixWidth=1.8868;        %In nm for x50000 magnification

%Define the level for pore selection, used in the im2bw command
BWlevel = 0.2;

%Load histogram bins from text file porebins'n'
histbins = load('porebins1.txt');
```

```
%Load list of file names to evaluate
filenames = textread('BWsamplelistNew.txt','%s');

filenum = length(filenames)

%Zero histtotal, Etotal, SA
histtotal= zeros(length(histbins),1);
Etotal=0;
SAtotal=0;

%Main loop for generating histograms
for j = 1:filenum;

  F = char(filenames(j))

  clear PoreArea;
  clear PoreDiameter;
  clear PoreCircum;
  clear PoreFlow;
  clear histtemp;
  clear HistFlow;
  clear HistSA;

  %Load image into an array, IM
  IM=imread(F);


  %Convert image from gray scale to black and white
  BW = im2bw(IM,BWlevel);

  %Invert the image for analysis, done by using the '~' prefix
  InvertBW = (~BW);

  [L,num] = bwlabel(InvertBW);

  stats=regionprops(L,'area','EquivDiameter');

  %Evaluate the area and equivalent diameter of each pore in the image
  for i=1:num;
    PoreArea(i)=stats(i).Area;
    PoreDiameter(i)=stats(i).EquivDiameter*PixWidth;
    PoreCircum(i)=pi*PoreDiameter(i);
    PoreFlow(i)=(0.5*PoreDiameter(i))^4;
  end

  E=sum(PoreArea)/(1280*1024);  %displays fraction of picture that is a pore, ~0.7
  SA=sum(PoreCircum);  %calculates total pore circumformance in image
  Flow=sum(PoreFlow);  %calculates total flow through image

  %Generate Histogram of equivalent pore diameter (in umeters)

  histtemp = histc(PoreDiameter,histbins);

  histeval(:,j)=histtemp(:);

  for k=1:length(histbins);
```

```
        HistFlow(k)=histtemp(k)*(0.5*histbins(k))^4;
        HistSA(k)=histtemp(k)*pi*histbins(k);
    end

    FlowEval=sum(HistFlow);
    SaEval=sum(HistSA);

    MaxPore=max(PoreDiameter);

    DisplayData(:,j)=[num,E,MaxPore,SA,SaEval,Flow,FlowEval]';

    histtotal(:) = histtotal(:) + histtemp(:);

end
```

B.5.1 Example of text file for pore size bins, *porebins5*

```
2.5
7.5
12.5
17.5
22.5
27.5
32.5
37.5
42.5
47.5
52.5
57.5
62.5
67.5
72.5
77.5
82.5
87.5
92.5
97.5
102.5
107.5
112.5
117.5
122.5
127.5
132.5
137.5
142.5
147.5
152.5
157.5
162.5
167.5
172.5
```

```
177.5
182.5
187.5
192.5
197.5
200
```

B.5.2 Example text file of image names, *BWsamplelist*

```
500-s-1mf.bmp
500-s-2mf.bmp
500-s-3mf.bmp
500-s-4mf.bmp
500-s-5mf.bmp
500-s-6mf.bmp
500-s-7mf.bmp
500-s-8mf.bmp
500-s-9mf.bmp
500-s-10mf.bmp
```

B.6 Log-normal distribution fitting – pore radius, *lognormfit*

```
%nonlinear fitting for lognormal pore size distribution
%Log normal distribution as defined in Zydney et al., 1994
%Data generated from image analysis

clear

No=2154; %From image analysis for 5 um bins

RawData = load('PoredataTrunc5.txt'); %[diameter,fR]
Reval = 1:65; %Pore radii in 1 um increments for intergration

r = RawData(:,1)/2;
fR = RawData(:,2);

Index = length(RawData);

options=optimset('MaxIter',10000);

sig1 = 5;
Rm = 25;
n0 = 50;

params0=[sig1,Rm];

params = fminsearch(@lognorm1,params0,options,r,fR,Index,No,n0,Reval);

sig1 = params(1);
Rm = params(2);
%n0 = params(3);
```

```
for i = 1:65;
   PDF(i)=n0/No*exp(-(log(Reval(i))-log(Rm))^2/(log(sig1)^2));
end

For i = 1:65;
   Eval(i)=n0/No*exp(-(log(Reval(i))-log(Rm))^2/(log(sig1)^2));
end

n0=n0/(sum(Eval))

for j =1:Index;
   DataEst(j,1)=(PDF(1,j)-fR(j,1))^2;
end

sum(DataEst(:,1))
params'
```

B.6.1 Example of distribution data, *poredataTrunc5*

10	0.00018
15	0.00108
20	0.00504
25	0.01664
30	0.02635
35	0.02608
40	0.02302
45	0.01987
50	0.01448
55	0.01223
60	0.01061
65	0.00818
70	0.00540
75	0.00603
80	0.00441
85	0.00324
90	0.00216
95	0.00243
100	0.00216
105	0.00135
110	0.00126
115	0.00126
120	0.00162
125	0.00108
130	0.00090

B.7 Log-normal distribution function – pore radius, *lognorm*

```
%Lognormal Distribution Function

function f=lognorm(beta0,r)  %beta is the array beta0 = [sig,R]

sig = beta0(1);
R = beta0(2);

x1 = r(:);

NumData = length(x1);

for i = NumData;
   Y1(i)=1/(sig*x1(i)*(2*pi)^0.5)*exp((-1/2*sig^2)*(log(x1(i))-log(R))^2);
end

f = Y1';
```

B.8 Log-normal distribution fitting – normalized flow, *lognormfitFlow*

```
%nonlinear fitting for lognormal pore size distribution
%Log normal distribution as defined in Zydney et al., 1994
%Data generated from image analysis

clear

No=2154; %From image analysis for 5 um bins

RawData = load('FlowdataTrunc5.txt'); %[diameter,fR]

r = RawData(:,1)/2;
fR = RawData(:,2);

Index = length(RawData);

options=optimset('MaxIter',10000);

sig1 = 2.5;
Rm = 15;
n0 = .76932E-05;

params0=[sig1,Rm,n0];

params = fminsearch(@lognorm2,params0,options,r,fR,Index,No);

sig1 = params(1);
Rm = params(2);
n0 = params(3);

params'
```

B.8.1 Example of distribution data, *FlowdataTrunc5*

```
10      1.08E-07
15      3.27E-06
20      4.82E-05
25      3.89E-04
30      1.28E-03
35      2.34E-03
40      3.53E-03
45      4.87E-03
50      5.41E-03
55      6.69E-03
60      8.23E-03
65      8.74E-03
70      7.75E-03
75      1.14E-02
80      1.08E-02
85      1.01E-02
90      8.47E-03
95      1.18E-02
100     1.29E-02
105     9.81E-03
110     1.10E-02
115     1.32E-02
120     2.01E-02
125     1.58E-02
130     1.54E-02
```

B.9 Log-normal distribution function – normalized flow, *lognormFlow*

```
function f=lognorm2(params,r,fR,Index,No,n0);

%params is the array params = [sig,Rm,n0]

%DataEst = zeros(Index,1);

%Lognormal Distribution Function
sig1 = params(1);
Rm = params(2);
n0 = params(3);

%n0 = No*(1/pi)^0.5*exp(-1*(log(sig1))^2/4)*(1/(Rm*log(sig1)));

for i = 1:Index;
   PDF(i)=n0/No*exp(-(log(r(i))-log(Rm))^2/(log(sig1)^2))*r(i)^4;
end

for j =1:Index;
   DataEst(j,1)=(PDF(1,j)-fR(j,1))^2;
end

Resid=sum(DataEst);
```

```
f = Resid;
```

B.10 Frucotose ODE method, *FrucFit*

```
%nonlinear curve fitting for fructose degradation
%Arrhenius model only, pH constant in each group of data
%Data generated from thermal bath experiments
%C = Sugar Concentration, dimensionless
%K = kinetic rate constant in 1/sec
%T = Temperature of sample, degrees C
%R = Universal gas constant, 8.314 J/(mol K)

clear

R=8.314;
dt = 5;     %seconds for each interval

RawData = load('FrucData.txt'); %[C,K,T]
Temp = load('FrucTemps.txt');

Index=length(RawData)

options=optimset('MaxIter',10000);

k1=1.5e10;
k2=4e10;
k3=5e10;
k4=8e10;
k5=1e11;
Ea=109000;

params0=[k1,k2,k3,k4,k5,Ea];

params = fminsearch(@FrucFitFunc,params0,options,RawData,Temp,Index,dt,R);

K(1)=params(1);
K(2)=params(2);
K(3)=params(3);
K(4)=params(4);
K(5)=params(5);
Ea=params(6);

for i=1:Index;
   Cprev=1;
   T=RawData(i,3); %Temp Profile to use for sample
   z=RawData(i,2); %kinetic parameter to use for sample
   for j=2:Temp(1,T)-1;
      n1=-K(z)*exp(-Ea/(R*(273.15+Temp(j,T))))*dt*Cprev;
      n2=-K(z)*exp(-Ea/(R*(273.15+(Temp(j,T)+Temp(j+1,T))/2)))*dt*(Cprev+n1/2);
      n3=-K(z)*exp(-Ea/(R*(273.15+(Temp(j,T)+Temp(j+1,T))/2)))*dt*(Cprev+n2/2);
      n4=-K(z)*exp(-Ea/(R*(273.15+Temp(j+1,T))))*dt*(Cprev+n3);

      Cest=Cprev+n1/6+n2/3+n3/3+n4/6;
      Cprev=Cest;
```

```
    end
    CalcFruc(i,2)=Cest;
    CalcFruc(i,1)=RawData(i,1);
end

kinetics(1)=K(1);
kinetics(2)=K(2);
kinetics(3)=K(3);
kinetics(4)=K(4);
kinetics(5)=K(5);
kinetics(6)=Ea;
```

B.10.1 Example temperature profile, *FrucTemps* (data file truncated)

47	72	105	154	49	70	104	164	51	74	112	153
21.1	21	21.8	20.9	18.4	21.4	18.5	18.3	18.6	18.4	18.8	18.2
25	21.1	21.9	29	29.9	42.3	35.3	22.3	27.1	22.1	24.4	23.4
45.8	36.2	40.5	64.3	47.2	59.3	53.6	44.1	44.9	41.7	42.3	56.9
65	55.1	56.9	76.6	65.3	71.8	80	59.8	57.9	55.1	55.2	68.4
76.1	81.3	80.8	85.2	77	82.6	86.8	74.5	68.8	68.4	75.9	79.2
83.9	87.6	87.8	90.2	85.2	92.1	90.6	85.4	76.6	85.7	83.3	85.2
92.4	91.5	91.9	92.4	92.8	115.9	97.3	90.5	88.3	89.9	88.3	89.1
96.4	94.2	97.9	109.3	102.8	127.2	109.7	108	90.8	95.1	91.7	91.4
108.6	102	105.6	120.2	116.6	135.4	123.7	121.4	92.7	105.4	93.1	94.1
119.6	124.6	123.2	128.1	128.1	144.3	143.6	131.9	95.1	115.2	99.6	100.3
126.7	133.8	130.8	133.7	137.7	150.9	151.6	139.6	101.4	125.1	105.9	108.3
133.4	141.4	138.3	140.6	153.4	157.2	158.4	148.9	107.2	140.8	112.6	114.3
143.2	148.2	144.2	142.6	159	168.6	164.5	154.9	112.9	146.6	117.6	120.7
145.2	151.6	151.8	145.3	164.2	171.9	169.3	165.4	123.5	151.2	123.3	130.4
146.7	153.4	155.8	149.3	167.4	173.6	173.9	169.6	128	155.5	128.5	134.2
147.6	155.4	157.8	150.6	170.9	174.5	174.8	173.1	131.5	158.7	132.7	137.6
148.2	155.6	159.2	151.6	171.8	175.1	175.5	174.6	135.8	165.6	139.7	140.5
148.8	156.2	159.2	152.6	173.1	175.7	176	176.1	139.4	168.6	142.6	142.9
148.9	156.3	159.2	153.3	174.6	176.4	176.6	177	146.3	171.6	145.2	145.4
149.1	156.4	159.2	154.8	175.3	176.4	176.6	177.8	149.5	173.6	148.3	150.4
149.2	156.6	158.6	155.5	175.4	176.6	176.7	179.1	152.3	176.2	151	152.8
149.3	156.8	157.9	156.2	176.1	176.7	177.3	179.2	154.6	178.2	156	155.1
149.8	156.9	157.9	156.3	176.2	176.8	177.4	179.8	157.2	179.9	158.2	157.1
149.8	157	157.8	156.9	176.9	177	177.5	179.9	159.7	182.7	160	158.9
149.9	157.1	157.7	157.5	177.4	177.1	178	180.4	161.8	184	161.7	162.5
150	157.1	157.5	157.8	177.4	177.4	178	180.7	165.9	185.2	163.7	164

Full data set continued...

B.10.2 Example fructose data, *FrucData*

0.9647	1	1
0.8699	1	2
0.7768	1	3
0.5301	1	4
0.5331	1	4

```
0.8981  2       1
0.6155  2       2
0.4704  2       3
0.1289  2       4
0.1209  2       4
0.7749  3       1
0.3605  3       2
0.1695  3       3
0.0156  3       4
0.6917  4       1
0.0730  4       3
0.6254  5       1
0.1980  5       2
0.0371  5       3
0.8194  1       5
0.5476  1       6
0.1238  1       8
0.1252  1       8
0.4283  2       5
0.0959  2       6
0.0306  2       7
0.0000  2       8
0.0180  2       8
0.6551  1       9
0.1272  1       10
0.0377  1       11
0.0218  1       12
0.0325  1       12
```

B.11 Fructose ODE function, *FrucFitFunc*

```
function f=FrucFitFunc(params,RawData,Temp,Index,dt,R);

%params is array = [k,Ea]
%Arrhenius only model for constant pH using Runge-Kutta method
%The number of time points for each final concentration is stored as the
%first row of the matrix TempProf (Temperature Profile)
%k is in units of 1/sec

K(1) = params(1);
K(2) = params(2);
K(3) = params(3);
K(4) = params(4);
K(5) = params(5);
Ea = params(6);

for i=1:Index;
   T=RawData(i,3); %Temp Profile to use for sample
   z=RawData(i,2); %kinetic parameter to use for sample
   Cprev=1;
   for j=2:Temp(1,T)-1;
      n1=-K(z)*exp(-Ea/(R*(273.15+Temp(j,T))))*dt*Cprev;
      n2=-K(z)*exp(-Ea/(R*(273.15+(Temp(j,T)+Temp(j+1,T))/2)))*dt*(Cprev+n1/2);
      n3=-K(z)*exp(-Ea/(R*(273.15+(Temp(j,T)+Temp(j+1,T))/2)))*dt*(Cprev+n2/2);
      n4=-K(z)*exp(-Ea/(R*(273.15+Temp(j+1,T))))*dt*(Cprev+n3);
```

```
    Cest=Cprev+n1/6+n2/3+n3/3+n4/6;
    Cprev=Cest;
  end
  DataEst(i)=(Cprev-RawData(i,1))^2;
end

Resid=sum(DataEst);

f = Resid;
```

B.12 Glucose linearization method, *GlucFit*

```
%nonlinear curve fitting for fructose degradation
%Arrhenius model only, pH constant in each group of data
%Data generated from thermal bath experiments
%C = Sugar Concentration, dimensionless
%pH = pH of sample
%T = Temperature of sample, degrees C
%R = Universal gas constant, 8.314 J/(mol K)

clear

R=8.314;
dt = 5;     %seconds for each interval

RawData = load('GlucData.txt'); %[C,K,Tprof,Tref]
Temp = load('FrucTemps.txt');   %Temperature profile is the same for both sugars

Index=length(RawData)

Data01 = load('Gluc01.txt');
Data04 = load('Gluc04.txt');
Data10 = load('Gluc10.txt');
Data15 = load('Gluc15.txt');
Data20 = load('Gluc20.txt');

%Prepare data for regression [calculate ln(G) and 1/T]

%Data(:,1)=log(RawData(:,1));
%Data(:,4)=1./(273.15 + RawData(:,4));
%Data(:,2)=RawData(:,2);
%Data(:,3)=RawData(:,3);


Data01(:,1)=log(Data01(:,1));
Data01(:,4)=1./(273.15 + Data01(:,4));
Data04(:,1)=log(Data04(:,1));
Data04(:,4)=1./(273.15 + Data04(:,4));
Data10(:,1)=log(Data10(:,1));
Data10(:,4)=1./(273.15 + Data10(:,4));
Data15(:,1)=log(Data15(:,1));
Data15(:,4)=1./(273.15 + Data15(:,4));
Data20(:,1)=log(Data20(:,1));
Data20(:,4)=1./(273.15 + Data20(:,4));
```

```
DataPts(1)=length(Data01);
DataPts(2)=length(Data04);
DataPts(3)=length(Data10);
DataPts(4)=length(Data15);
DataPts(5)=length(Data20);

options=optimset('MaxIter',10000);

k1=1.0e10;
k2=1.5e11;
k3=2.0e11;
k4=2.5e11;
k5=3.5e11;
Ea=108100;

params0=[k1,k2,k3,k4,k5,Ea];

params                                                                                                    =
fminsearch(@GlucFitFunc,params0,options,Data01,Data04,Data10,Data15,Data20,Temp,DataPts,dt,R);

K(1)=params(1);
K(2)=params(2);
K(3)=params(3);
K(4)=params(4);
K(5)=params(5);
Ea=params(6);

for i=1:Index;
   Cprev=1;
   T=RawData(i,3); %Temp Profile to use for sample
   z=RawData(i,2); %kinetic parameter to use for sample
   for j=2:Temp(1,T)-1;
      n1=-K(z)*exp(-Ea/(R*(273.15+Temp(j,T))))*dt*Cprev;
      n2=-K(z)*exp(-Ea/(R*(273.15+(Temp(j,T)+Temp(j+1,T))/2)))*dt*(Cprev+n1/2);
      n3=-K(z)*exp(-Ea/(R*(273.15+(Temp(j,T)+Temp(j+1,T))/2)))*dt*(Cprev+n2/2);
      n4=-K(z)*exp(-Ea/(R*(273.15+Temp(j+1,T))))*dt*(Cprev+n3);

      Cest=Cprev+n1/6+n2/3+n3/3+n4/6;
      Cprev=Cest;
   end
   CalcGluc(i,2)=Cest;
   CalcGluc(i,1)=RawData(i,1);
end

%Copied from function to calculate SSE, SST, and R^2

%Calculate the equivalent reaction time (RTeq) for each temperature catagory
%RTeq is a function of both temperature and Activation Energy (Ea)
Tref = [160,160,160,160,180,180,180,180,200,200,200,200];

for r=1:12;
   RTtemp=zeros(Temp(1,r),1);
   for j=2:Temp(1,r);
      RTtemp(j)=dt/exp(Ea/R*(1/(273.15+Temp(j,r))-1/(273.15+Tref(r))));
   end
```

```
   RTeq(r)=sum(RTtemp)./60;
end

%Regress each data set to determine parameters
%Data for 0.4% H2SO4
for i=1:DataPts(1);
   T=Data01(i,3); %Temp Profile to use for sample
   z=Data01(i,2); %kinetic parameter to use for sample

   lnKs(i)=log(-Data01(i,1)/RTeq(T));
   Eval(i)=(-Ea/R)*Data01(i,4)+log(K(z));

   DataEst(i)=(lnKs(i)-Eval(i))^2;
end
SST(1)=sum(lnKs.^2)-(sum(lnKs))^2/DataPts(1)
SSE(1)=sum(DataEst);
R2(1)=1-SSE(1)./SST(1);
clear DataEst Eval lnKs;

%Data for 0.4% H2SO4
for i=1:DataPts(2);
   T=Data04(i,3); %Temp Profile to use for sample
   z=Data04(i,2); %kinetic parameter to use for sample

   lnKs(i)=log(-Data04(i,1)/RTeq(T));
   Eval(i)=(-Ea/R)*Data04(i,4)+log(K(z));

   DataEst(i)=(lnKs(i)-Eval(i))^2;
end

SSE(2)=sum(DataEst);
clear DataEst Eval lnKs;

%Data for 1.0% H2SO4
for i=1:DataPts(3);
   T=Data10(i,3); %Temp Profile to use for sample
   z=Data10(i,2); %kinetic parameter to use for sample

   lnKs(i)=log(-Data10(i,1)/RTeq(T));
   Eval(i)=(-Ea/R)*Data10(i,4)+log(K(z));

   DataEst(i)=(lnKs(i)-Eval(i))^2;
end

SSE(3)=sum(DataEst);
clear DataEst Eval lnKs;

%Data for 1.5% H2SO4
for i=1:DataPts(4);
   T=Data15(i,3); %Temp Profile to use for sample
   z=Data15(i,2); %kinetic parameter to use for sample

   lnKs(i)=log(-Data15(i,1)/RTeq(T));
   Eval(i)=(-Ea/R)*Data15(i,4)+log(K(z));

   DataEst(i)=(lnKs(i)-Eval(i))^2;
```

```
end

SSE(4)=sum(DataEst);
clear DataEst Eval lnKs;

%Data for 2.0% H2SO4
for i=1:DataPts(5);
   T=Data20(i,3); %Temp Profile to use for sample
   z=Data20(i,2); %kinetic parameter to use for sample

   lnKs(i)=log(-Data20(i,1)/RTeq(T));
   Eval(i)=(-Ea/R)*Data20(i,4)+log(K(z));

   DataEst(i)=(lnKs(i)-Eval(i))^2;
end

SSE(5)=sum(DataEst);
clear DataEst Eval lnKs;
```

B.12.1 Example glucose data, *GlucData01*

0.9755	1	2	160
0.9530	1	3	160
0.9151	1	4	160
0.8864	1	4	160
0.9165	1	5	180
0.8593	1	6	180
0.7460	1	8	180
0.7163	1	8	180
0.7964	1	10	200
0.6174	1	11	200
0.5431	1	12	200
0.3099	1	12	200

B.13 Glucose linearization function, *GlucFitFunc*

```
function f=GlucFitFunc(params,Data01,Data04,Data10,Data15,Data20,Temp,DataPts,dt,R);

RTeq=zeros(12,1);

%params is array = [k,Ea]
%Arrhenius only model for constant pH using regression of ln(Ks) vs. 1/T
%First row of Temp is the number of non-zero values in each column

K(1) = params(1);
K(2) = params(2);
K(3) = params(3);
K(4) = params(4);
K(5) = params(5);
Ea = params(6);
```

```
%Calculate the equivalent reaction time (RTeq) for each temperature catagory
%RTeq is a function of both temperature and Activation Energy (Ea)
Tref = [160,160,160,160,180,180,180,180,200,200,200,200];

for r=1:12;
   RTtemp=zeros(Temp(1,r),1);
   for j=2:Temp(1,r);
      RTtemp(j)=dt/exp(Ea/R*(1/(273.15+Temp(j,r))-1/(273.15+Tref(r))));
   end
   RTeq(r)=sum(RTtemp)./60;
end

%Regress each data set to determine parameters
%Data for 0.4% H2SO4
for i=1:DataPts(1);
   T=Data01(i,3); %Temp Profile to use for sample
   z=Data01(i,2); %kinetic parameter to use for sample

   lnKs(i)=log(-Data01(i,1)/RTeq(T));
   Eval(i)=(-Ea/R)*Data01(i,4)+log(K(z));

   DataEst(i)=(lnKs(i)-Eval(i))^2;
end

SSE(1)=sum(DataEst);
clear clear DataEst Eval lnKs;

%Data for 0.4% H2SO4
for i=1:DataPts(2);
   T=Data04(i,3); %Temp Profile to use for sample
   z=Data04(i,2); %kinetic parameter to use for sample

   lnKs(i)=log(-Data04(i,1)/RTeq(T));
   Eval(i)=(-Ea/R)*Data04(i,4)+log(K(z));

   DataEst(i)=(lnKs(i)-Eval(i))^2;
end

SSE(2)=sum(DataEst);
clear clear DataEst Eval lnKs;

%Data for 1.0% H2SO4
for i=1:DataPts(3);
   T=Data10(i,3); %Temp Profile to use for sample
   z=Data10(i,2); %kinetic parameter to use for sample

   lnKs(i)=log(-Data10(i,1)/RTeq(T));
   Eval(i)=(-Ea/R)*Data10(i,4)+log(K(z));

   DataEst(i)=(lnKs(i)-Eval(i))^2;
end

SSE(3)=sum(DataEst);
clear clear DataEst Eval lnKs;

%Data for 1.5% H2SO4
```

```
for i=1:DataPts(4);
   T=Data15(i,3); %Temp Profile to use for sample
   z=Data15(i,2); %kinetic parameter to use for sample

   lnKs(i)=log(-Data15(i,1)/RTeq(T));
   Eval(i)=(-Ea/R)*Data15(i,4)+log(K(z));

   DataEst(i)=(lnKs(i)-Eval(i))^2;
end

SSE(4)=sum(DataEst);
clear clear DataEst Eval lnKs;

%Data for 2.0% H2SO4
for i=1:DataPts(5);
   T=Data20(i,3); %Temp Profile to use for sample
   z=Data20(i,2); %kinetic parameter to use for sample

   lnKs(i)=log(-Data20(i,1)/RTeq(T));
   Eval(i)=(-Ea/R)*Data20(i,4)+log(K(z));

   DataEst(i)=(lnKs(i)-Eval(i))^2;
end

SSE(5)=sum(DataEst);
clear clear DataEst Eval lnKs;

Resid=mean(SSE);

f = Resid;
```

B.14 5-HMF ODE method, *HMFFit*

```
%nonlinear curve fitting for fructose degradation
%Arrhenius model only, pH constant in each group of data
%Data generated from thermal bath experiments
%C = Sugar Concentration, dimensionless
%K = kinetic rate constant in 1/sec
%T = Temperature of sample, degrees C
%R = Universal gas constant, 8.314 J/(mol K)

clear

R=8.314;
dt = 5;     %seconds for each interval

RawData = load('HMFSevData.txt'); %[C,K,T]
Temp = load('FrucTemps.txt');

Index=length(RawData)

FG=[5.61e12, 3.10e11;1.70e13, 5.17e11;3.68e13, 6.38e11;5.00e13, 9.87e11;5.87e13, 1.02e12];
EaFG=[116800, 113000];
```

```
options=optimset('MaxIter',10000);

k1=1.5e11;
k2=4e11;
k3=5e11;
k4=8e11;
k5=1e12;
Ea=110000;

params0=[k1,k2,k3,k4,k5,Ea];

params = fminsearch(@HMFFitFunc,params0,options,RawData,Temp,Index,dt,R,FG,EaFG);

K(1)=params(1);
K(2)=params(2);
K(3)=params(3);
K(4)=params(4);
K(5)=params(5);
Ea=params(6);

for i=1:Index;
   Cprev=0;
   Fprev=1;
   Gprev=1;
   T=RawData(i,3); %Temp Profile to use for sample
   z=RawData(i,2); %kinetic parameter to use for sample
   for j=2:Temp(1,T)-1;
      f1=-FG(z,1)/60*exp(-EaFG(1)/(R*(273.15+Temp(j,T))))*dt*Fprev;
      f2=-FG(z,1)/60*exp(-EaFG(1)/(R*(273.15+(Temp(j,T)+Temp(j+1,T))/2)))*dt*(Fprev+f1/2);
      f3=-FG(z,1)/60*exp(-EaFG(1)/(R*(273.15+(Temp(j,T)+Temp(j+1,T))/2)))*dt*(Fprev+f2/2);
      f4=-FG(z,1)/60*exp(-EaFG(1)/(R*(273.15+Temp(j+1,T))))*dt*(Fprev+f3);

      Fest=Fprev+f1/6+f2/3+f3/3+f4/6;
      delF=Fest-Fprev;
      Fprev=Fest;

      g1=-FG(z,2)/60*exp(-EaFG(2)/(R*(273.15+Temp(j,T))))*dt*Gprev;
      g2=-FG(z,2)/60*exp(-EaFG(2)/(R*(273.15+(Temp(j,T)+Temp(j+1,T))/2)))*dt*(Gprev+g1/2);
      g3=-FG(z,2)/60*exp(-EaFG(2)/(R*(273.15+(Temp(j,T)+Temp(j+1,T))/2)))*dt*(Gprev+g2/2);
      g4=-FG(z,2)/60*exp(-EaFG(2)/(R*(273.15+Temp(j+1,T))))*dt*(Gprev+g3);

      Gest=Gprev+g1/6+g2/3+g3/3+g4/6;
      delG=Gest-Gprev;
      Gprev=Gest;

      Cprev=Cprev-0.25*delF-0.25*delG; %Add the first half of F and G

      n1=-K(z)/60*exp(-Ea/(R*(273.15+Temp(j,T))))*dt*Cprev;
      n2=-K(z)/60*exp(-Ea/(R*(273.15+(Temp(j,T)+Temp(j+1,T))/2)))*dt*(Cprev+n1/2);
      n3=-K(z)/60*exp(-Ea/(R*(273.15+(Temp(j,T)+Temp(j+1,T))/2)))*dt*(Cprev+n2/2);
      n4=-K(z)/60*exp(-Ea/(R*(273.15+Temp(j+1,T))))*dt*(Cprev+n3);

      Cest=Cprev+n1/6+n2/3+n3/3+n4/6-0.25*delF-0.25*delG;
      Cprev=Cest;
   end
   CalcFruc(i,2)=Cest;
```

```
   CalcFruc(i,1)=RawData(i,1);
end

kinetics(1)=K(1);
kinetics(2)=K(2);
kinetics(3)=K(3);
kinetics(4)=K(4);
kinetics(5)=K(5);
kinetics(6)=Ea;
```

B.14.1 Example 5-HMF data, *HMFdata*

0.003876222	1	1
0.024580786	1	2
0.049587688	1	3
0.129905368	1	4
0.025517862	2	1
0.11515921	2	2
0.145884734	2	3
0.236857257	2	4
0.057365199	3	1
0.181736814	3	2
0.219077717	3	3
0.15527421	3	4
0.086727082	4	1
0.202844278	4	3
0.107800274	5	1
0.210606481	5	2
0.167816227	5	3
0.055590797	1	5
0.145497031	1	6
0.26070394	1	8
0.257004675	1	8
0.177955397	2	5
0.253570104	2	6
0.221160804	2	7
0.143008092	2	8
0.146939677	2	8
0.245638461	3	5
0.093129112	3	7
0.046433166	3	8
0.238526924	4	5
0.134231743	4	6
0.05796523	4	7
0.234124011	5	5
0.093968794	5	6
0.03759952	5	7
0.103605218	1	9
0.277518633	1	10
0.261040356	1	11
0.228151891	1	12
0.204816689	1	12
0.253921791	2	9
0.189666231	2	10

```
0.094498689     2       11
0.050750015     2       12
0.054112982     2       12
0.21999032      3       9
0.087862712     3       10
0.02870437      3       11
0.019658414     3       12
0.21175058      4       9
0.071513256     4       10
0.015340315     4       11
0.213305203     5       9
0.058274878     5       10
0.014249415     5       11
```

B.15 5-HMF ODE function, *HMFFitFunc*

```
function f=HMFFitFunc(params,RawData,Temp,Index,dt,R,FG,EaFG);

%params is array = [k,Ea]
%Arrhenius only model for constant pH using Runge-Kutta method
%The number of time points for each final concentration is stored as the
%first row of the matrix TempProf (Temperature Profile)
%k is in units of 1/sec

K(1) = params(1);
K(2) = params(2);
K(3) = params(3);
K(4) = params(4);
K(5) = params(5);
Ea = params(6);

for i=1:Index;
   T=RawData(i,3); %Temp Profile to use for sample
   z=RawData(i,2); %kinetic parameter to use for sample
   Cprev=0;
   Fprev=1;
   Gprev=1;
   for j=2:Temp(1,T)-1;
      f1=-FG(z,1)/60*exp(-EaFG(1)/(R*(273.15+Temp(j,T))))*dt*Fprev;
      f2=-FG(z,1)/60*exp(-EaFG(1)/(R*(273.15+(Temp(j,T)+Temp(j+1,T))/2)))*dt*(Fprev+f1/2);
      f3=-FG(z,1)/60*exp(-EaFG(1)/(R*(273.15+(Temp(j,T)+Temp(j+1,T))/2)))*dt*(Fprev+f2/2);
      f4=-FG(z,1)/60*exp(-EaFG(1)/(R*(273.15+Temp(j+1,T))))*dt*(Fprev+f3);

      Fest=Fprev+f1/6+f2/3+f3/3+f4/6;
      delF=Fest-Fprev;
      Fprev=Fest;

      g1=-FG(z,2)/60*exp(-EaFG(2)/(R*(273.15+Temp(j,T))))*dt*Gprev;
      g2=-FG(z,2)/60*exp(-EaFG(2)/(R*(273.15+(Temp(j,T)+Temp(j+1,T))/2)))*dt*(Gprev+g1/2);
      g3=-FG(z,2)/60*exp(-EaFG(2)/(R*(273.15+(Temp(j,T)+Temp(j+1,T))/2)))*dt*(Gprev+g2/2);
      g4=-FG(z,2)/60*exp(-EaFG(2)/(R*(273.15+Temp(j+1,T))))*dt*(Gprev+g3);

      Gest=Gprev+g1/6+g2/3+g3/3+g4/6;
      delG=Gest-Gprev;
```

```
      Gprev=Gest;

      Cprev=Cprev-0.25*delF-0.25*delG; %Add the first half of F and G

      n1=-K(z)/60*exp(-Ea/(R*(273.15+Temp(j,T))))*dt*Cprev;
      n2=-K(z)/60*exp(-Ea/(R*(273.15+(Temp(j,T)+Temp(j+1,T))/2)))*dt*(Cprev+n1/2);
      n3=-K(z)/60*exp(-Ea/(R*(273.15+(Temp(j,T)+Temp(j+1,T))/2)))*dt*(Cprev+n2/2);
      n4=-K(z)/60*exp(-Ea/(R*(273.15+Temp(j+1,T))))*dt*(Cprev+n3);

      Cest=Cprev+n1/6+n2/3+n3/3+n4/6-0.25*delF-0.25*delG; %Add the second half of F and G
      Cprev=Cest;
   end
   DataEst(i)=(Cprev-RawData(i,1))^2;
end

Resid=sum(DataEst);

f = Resid;
```